Quantitative analyses of structure-function heterogeneity of individual mitochondrial components reveal an early role of small-mitochondrial-networks in priming neoplastic transformation

Mayank Saini[1#], Swati Agarwala[1#], Biratal Wagle[1], Brian Spurlock[2], Bharti Golchha[1], Danitra Parker[2] and Kasturi Mitra[1,2*]

1 Department of Biology, Ashoka University, New Delhi (NCR), India

2 Department of Genetics, University of Alabama at Birmingham, Birmingham, Alabama, USA

* corresponding author: Kasturi Mitra

#Equal Contribution

Email: kasturi.mitra@ashoka.edu.in

Author Contributions: MS performed all mito-SinComp analyses, SA performed all transcriptomics analyses, BW developed mito-SinComp analyses with help from MS, BS and DP collected data, BG performed immunoblot analyses, KM supervised all aspects and wrote the manuscript with help from MS and SA.

Competing Interest Statement: None

Classification: Biological sciences, Cell Biology

Keywords: Small Mitochondrial Networks, Stem cells driven neoplasticity, Microscopy, single cell transcriptomics, TCDD.

This PDF file includes:

Main Text
Figures 1 – 7 and their legends

Abstract

Quantitative understanding of mitochondrial heterogeneity is necessary for elucidating the precise role of these multifaceted organelles. We demonstrate an early mechanistic role of mitochondria in initiating neoplasticity by employing our quantitative analyses of structure-function of individual mitochondria coupled with single cell transcriptomics. We demonstrate that the large 'Hyperfused Mitochondrial Networks' (HMNs) promptly get converted to the heterogenous 'Small Mitochondrial Networks' (SMNs) as the stem cell enriching low dose of the model carcinogen, TCDD, depolarizes mitochondria. This happens by reorganization of the HMN nodes and edges, which enriches redox tuned SMNs with distinct network complexity. This leads to establishment of transcriptomic interaction between the upregulated redox relevant mtDNA genes and the lineage specific stemness gene, KRT15, prior to cell cycle exit, and is detected only in the late-S phase of the neoplastic cell population. Consistently, high carcinogenic dose incapable of causing pronounced neoplastic stem cell enrichment fails to specifically enrich SMNs and establish the mtDNA-KRT15 transcriptomic interaction prior to cell cycle exit. The mtDNA-KRT15 modulation is confirmed in relevant tumors, while highlighting patient heterogeneity. Therefore, we propose that early enrichment of redox tuned SMNs primes neoplastic transformation by establishing interaction between mtDNA and stemness genes prior to cell cycle exit towards generating quiescent neoplastic stem cells. Our data implies that redox tuned SMNs, created by mitochondrial fission, would be sustained by tuning the balance of mitochondrial fission-fusion during neoplastic transformation. The proposed early role of mitochondria in cancer etiology is potentially relevant in designing precision strategies for cancer prevention and therapy.

Significance Statement

Using our novel quantitative combinatorial approach of quantitative microscopy and single cell transcriptomics, we elucidate a biological mechanism of cancer initiation involving stem cells. Based on data from experimentation with a model carcinogen, we propose that conversion of large 'Hyperfused Mitochondrial Networks' (HMNs) to heterogenous 'Small Mitochondrial Networks' (SMNs), by modulating the nodes and edges of mitochondrial networks, primes non-transformed cells towards stem cell driven neoplasticity. Mechanistically, the enriched SMNs would tune the mitochondrial redox balance to establish critical transcriptomic interactions required to maintain a stem cell state to support neoplastic transformation. Further testing of our fundamental findings in the light of cancer heterogeneity holds the promise of refinement of various proposed mitochondria based targeted cancer therapies.

Main Text

Introduction

Regulation of cellular homeostatic processes requires nuanced spatiotemporal control, which when disturbed may lead to pathological conditions. The mitochondria, as dynamic organelles, act as gatekeepers of multiple cellular homeostatic processes and, also form signalling hubs (1, 2). Mitochondria are heterogeneous between tissues, cell types and even within cells, while their dysfunctionality has been causatively linked to various disease pathology (3–5). The involvement of mitochondria in cancer pathology has been studied at various functional levels, including regulation of energy metabolism, signalling and gene expression (6, 7). Initiation of tumor formation can happen when the lineage specific adult stem cells undergo neoplastic transformation into tumor initiating cells (8, 9). Importantly, certain tumor initiating cells are particularly vulnerable to mitochondrial inhibition (10, 11). However, mitochondrial heterogeneity, at the level of tumors as well as patients, poses challenges in developing a generalized understanding of the exact role of mitochondria in cancer initiation or progression., thus making translation of findings difficult.

Mitochondria are heterogenous in their shapes and structures, including their elaborate physical networks, modulation of which affects cell proliferation and various other cellular processes critically (12–16). Mitochondrial structure-function is primarily modulated by the counteracting processes of mitochondrial fission and fusion. The core molecular machinery for mitochondrial fission involves Drp1 and its mitochondrial recruiters MFF or FIS1, while that of mitochondrial fusion are the Mitofusins and OPA1 (15, 17). Fission and fusion of mitochondria can act in concert in regulating the same or different aspect of a given cellular process (18–22). However, how mitochondrial fission and fusion processes coordinate to maintain the physical mitochondrial networks remains an open question, largely due to lack of quantitative understanding of the mitochondrial networks per se. Additionally, mitochondria can exist anywhere in the shape spectrum in normal or pathophysiological states, which is not reflected accurately by genetic alteration of the molecular players. Therefore, straightforward genetic approaches have led to confusing findings preventing building a consensus of the exact role of mitochondrial fission and fusion in cancer development. This highlights the necessity of developing quantitative understanding of the structure-function of mitochondria across their shape spectrum to elucidate the intricate interplay of mitochondria with other cellular process.

Various laboratories, including our own, have attempted to define and quantitate mitochondrial shape (23–30). Using quantitative approach of mitochondrial structure and function analyses, we have previously reported that a distinct structure and function state of mitochondria prime neoplastic stemness in ovarian and keratinocyte lineages (20, 30). In this priming process, low mitochondrial fission and high mitochondrial membrane potential are achieved to poise the cells for self-renewal and proliferation. Similar mitochondria-driven priming of stem cells has also been reported in neural, hematopoietic and mammary lineages (31–33). TCDD is a model oxidative carcinogen that influences stemness properties in multiple cell lineages (34–39). Using single cell approaches (microscopy and transcriptomics) we reported that repression of mitochondrial fission as well as its regulated activation are required to prime a stem cell state to initiate as well as sustain TCDD induced neoplasticity in keratinocytes (20). Activation of

mitochondrial fission is also essential for oncogene induced neoplastic transformation in other lineages (40, 41).

Here, we investigate the mechanism of mitochondrial priming of stemness towards initiating neoplastic transformation. Towards that, we developed quantitative analysis of single mitochondrial structure-function, mito-SinComp, to tease out mitochondrial heterogeneity, and employed it along with quantitative single cell RNA Seq (scRNA-seq). We find that particularly low dose carcinogen can itself induce mitochondria-based priming of stemness in non-transformed cells within one hour of exposure. We and others have previously described the role of hyperfusion of mitochondria during cell cycle transition, stress and starvation induced situations (22, 42, 43). Here we demonstrate that TCDD driven priming of neoplasticity involves precise conversion of the '**H**yperfused-**M**itochondrial-**N**etworks **(HMNs)'** to '**S**mall-**M**itochondrial-**N**etworks **(SMNs)'**. Based our data from mito-SinComp analyses and hdWGCNA, we propose that early enrichment of redox tuned SMNs primes neoplastic transformation by establishing interaction between mtDNA and stemness genes prior to cell cycle exit towards generating quiescent neoplastic stem cells. Data obtained with our novel and combinatorial approaches reveal a mechanistic underpinning of cancer initiation involving mitochondrial priming of stemness, while highlighting heterogeneity of such a process in patient tumors. Further testing our fundamental findings in patient tumors holds the promise of facilitating informed design of personalized strategies for cancer prevention and therapy.

Results

Single mitochondrial analyses identify and characterize the physical Small- Mitochondrial-Networks that are linked to stemness transcriptomic network

We previously employed single cell modalities of mito-SinCe (for mitochondrial shape analyses) and scRNA-seq (for transcriptomics analyses) to elucidate mitochondrial priming of stem cell driven neoplasticity in HaCaT keratinocytes (20, 44). Such mitochondrial priming of self-renewal and proliferation is characterized by enrichment of cells with intermediately-fused mitochondria, while hyperfusion of mitochondria prevents such stem cell priming. Here we designed analyses of single mitochondrial components, 'mito-SinComp', to quantitively define, identify and characterize the physical mitochondrial networks, and identify any linked stemness transcriptomic network by employing scRNA-seq analyses. We took advantage of our previously published mito-SinCe data set where 'intermediately-fused' (**INT**) or 'hyperfused' (**HF**) mitochondria are enriched, respectively, in cells with weak or strong knockdown of the mitochondrial fission protein Drp1 (20). Here, we combined this data set and studied individual mitochondrial networks and non-networks from the INT and HF cell groups as defined by the [Fission] vs [Fusion5] bivariate plots (**Fig. 1A**); these mito-SinCe metrics were designed from MitoGraph output (30, 45). The total mitochondrial length per cell in the INT group is lower than that of the HF group where, by definition, cells tend to have fewer mitochondrial components due to fusion of majority of components (**Fig. S1A-B**).

Using the newly developed mito-SinComp pipeline on the MitoGraph output we identified individual networks and non-networks of mitochondria (see Main and Supplementary Methods for details), as represented by Cell1-INT and Cell2-HF having comparable total mitochondrial length

146 **(Fig. 1B, Fig. S1C, Suppl. Data 1** showing comparison of the metrics for each cell**)**. The mito-
147 SinComp pipeline revealed various structural properties of mitochondrial components in the INT-
148 Cells and HF-Cells groups: **a)** comparable abundance of networked and non-networked
149 mitochondria per cell (**Fig. S1D-E**) and length of non-networked mitochondria between the groups
150 (**Fig. S1F,** right); **b)** higher abundance of longer networked mitochondria (i.e. hyperfused) in the
151 HF-Cells group (**Fig. S1F,** left); **c)** the average length of the networked mitochondria per cell is
152 substantially shorter in the INT-Cells group in comparison to the HF-Cells group, while the
153 networked mitochondria are ~10-100 times longer than the non-networked mitochondria (**Fig. 1C,**
154 **Fig. S1G**). These data raised the possibility that the INT-cells may be enriched with Small
155 Mitochondrial Networks (**SMNs**) in contrast to the longer Hyperfused Mitochondrial Networks
156 (**HMNs**) of the HF-cells. To confirm this, we computed the 'Cell-Relative Length of mitochondrial
157 network or non-network', [CRL mito-Net] or [CRL mito-nonNet]. This metric for a networked or
158 non-worked mitochondria is the natural log transformed value of its length normalized by the total
159 length of network or non-network of the cell it belongs to (**Suppl. Methods**). The networks with
160 maximum [CRL mito-Net] for the mitochondrial populations of Cell 1- INT and Cell 2-HF are
161 boxed and extracted in **Fig. 1B** and their network metrics are listed in **Suppl. Data 1**.
162 Interestingly, frequency distribution of [CRL mito-Net] indicates more networks with higher value
163 of this metric are found in the INT-cells than the HF-cells, while it is reverse for the [CRL mito-
164 nonNet] (**Fig. 1D**). This data signifies that SMN enriched cells harbor multiple networks of
165 comparable length as opposed to fewer HMNs in any cell. Therefore, we aimed to distinctly
166 classify the SMNs and the HMNs using a threshold range of [CRL mito-Net] (**Fig. 1D**) (see
167 appropriate Methods section for more details of the threshold). Classification using [CRL mito-
168 Net] confirmed that the number of SMNs is ~5 fold higher than the HMNs in the total population of
169 INT-cells and HF-cells **(Fig. S1H)**, as exemplified by Cell 1-INT and Cell 2-HF in **Fig. 1B**. Most
170 importantly, [CRL mito-Net] based classification demonstrated marked enrichment of the
171 identified SMNs in the INT-cells while confirming the expected enrichment of the identified HMNs
172 in the HF-cells (**Fig. 1E**).

173 Thereafter, we quantified the network properties between the SMN and the HMNs using
174 various metrics (see **Suppl. Methods** for definition and formulae) and compared the median and
175 the coefficient of variation (indicating heterogeneity) (**Fig. 1F, Fig. S1I**). In comparison to the
176 HMNs, the SMNs exhibit the following properties: **a)** ~2 fold smaller in size (assessed by length)
177 and are remarkably heterogenous in thickness (assessed by diameter); **b)** ~10 fold fewer
178 mitochondrial nodes and edges (edges represent individual mitochondrial elements within a
179 network and the terminal free nodes are not counted). **c)** by and large comparable element size
180 (assessed by element length) within a network; **d)** comparable network complexity (assessed by
181 nodes or edge density), with remarkable heterogeneity; **e)** comparable overall and maximum
182 connectivity. These metrics demonstrate that as compared to the HMNs, the SMNs are
183 remarkably heterogenous in their thickness and network complexity, while their organization of
184 the nodes and edges are distinct with comparable length of individual mitochondrial element
185 within the networks.

186 Next, we asked if SMN enrichment can be linked to the transcriptomic network of the
187 functional stem cell gene, KRT15, of the keratinocyte lineage (46). Therefore, we employed the
188 recently reported hdWGCNA pipeline (see Methods) on our published scRNA-seq data. There,
189 the KRT15^{hi} stem cells are enriched by the weak (W) Drp1 knockdown and depleted by the strong
190 (S) Drp1 knockdown (kd) (20). First, we performed pairwise pseudo-bulk RNA-seq analyses to
191 identify the genes that are differentially expressed in the Drp1-kd (W) and Drp1-kd (S)

192 populations with respect to the NT control populations. hdWGCNA of the combined gene sets of
193 the above pairwise analyses identified the KRT15 transcriptomic interaction module with 10
194 genes directly interacting with KRT15 **(Fig. 1G, left, Fig. S2A).** Next, we performed cell cluster
195 analyses of the pooled data sets of the NT, Drp1-kd (W) data and Drp1-kd (S) populations.
196 Notably, 4 out of the above 10 directly interacting partners of KRT15 were confirmed in one of the
197 modules identified by hdWGCNA performed with the marker genes of the quiescent / slow-cycling
198 KRT15^{hi} stem cell cluster (SloCycl-K15^{hi} as in ref. (20)) **(Fig. 1G, right, Fig. 1H, Fig. S2B-C,**
199 **boxed)**. Most importantly, the KRT15 interacting genes undergo marked upregulation across all
200 cell clusters in the Drp1-kd (W) population that sustains enrichment of the stem cell linked INT
201 subpopulation harboring abundant SMNs **(Fig. 1I, Fig. S2D)**. On the other hand, two of those
202 genes (CRABP2, KRT4) undergo marked downregulation only in the SloCycl-K15^{hi} cells Drp1-kd
203 (S) population with abundant HF-cells with depleted SMNs.

204 In summary, by employing mito-SinComp structural analyses on the combined population
205 of Drp1 knockdown and control we designed the metric for the physical mitochondrial network,
206 [CRL mito-Net] to distinguish the SMNs from the HMNs within individual cells (**Fig. 1J**). The
207 SMNs are abundant in the INT-cells that are prevalent in the stem cell enriched Drp1-kd (W)
208 population (20). Whereas the SMNs are fewer in the HF-cells that are prevalent in the stem cell
209 depleted Drp1-kd (S) population (20). In comparison to the HMNs, the SMNs are remarkably
210 heterogenous, have distinct network organization, and are linked to stemness transcriptomic
211 network characterized by KRT15-interacting genes identified by hdWGCNA analyses. Application
212 of the same [CRL mito-Net] threshold successfully detected enrichment of SMNs in sorted
213 neoplastic stem cells in yet another lineage (not shown).

214

215 **Acute-1h exposure to stem cell enriching carcinogen depolarizes mitochondria and**
216 **converts HMNs to complex and heterogenous SMNs, by modulating their nodes and edges**

217 HaCaT keratinocytes that maintain 'intermediately-fused' or 'hyperfused' mitochondria
218 **(**similar to **Fig.1A)** are primed or blocked, respectively, for stem cell driven neoplastic
219 transformation driven by the model carcinogen TCDD (20). Here we find, acute 1 hour exposure
220 of HaCaTs to TCDD-1nM (T1) promptly depolarizes mitochondria with respect to Toluene (Tol)
221 vehicle control **(Fig. 2A** top**, Fig. S3A, Fig. S3B** top**)**. However, the higher dose, TCDD-10nM
222 (T10), needs 4 hours to cause the marked mitochondrial depolarization **(Fig. 2A, Fig. S3B**
223 bottom**)**. We hypothesized that the dose independent early mitochondrial depolarization by T1-1h
224 exposure causes mitochondrial priming for stemness to promote stem cell driven neoplasticity
225 observed with prolonged T1 exposure (20). Given mitochondrial depolarization causes alteration
226 of mitochondrial shape in various systems tested (15, 47), we studied the quantitative properties
227 of mitochondrial structure after exposure to Tol-1h (vehicle control), T1-1h (stem cell enriching
228 dose) and T10-1h (control dose) **(Fig. 2B)**. We used live cells stably expressing the
229 mitochondrial structural probe mito-PSmO2 for determining structural features of single
230 mitochondrial components within single cells **(Fig. S3C)**. The 3D maps of networked and non-
231 networked mitochondria in the representative cells from experimental groups indicate lack of
232 large mitochondrial networks after T1-1h exposure, whereas the T10-1h exposed mitochondrial
233 networks appear to be similar to that of Tol-1h (**Fig. 2C)**. Consistently, the mito-SinCe metric
234 [Fission] suggests that T1-1h exposure elevates the contribution of mitochondrial fission in
235 maintaining mitochondrial shape, which is modest with T10-1h exposure **(Fig. 2D)**. However, the

236 mito-SinCe metric [Fusion5] reveals that the reduced contribution of mitochondrial fusion is
237 comparable between the T1-1h and T10-1h exposure.

238 To probe further, we performed mito-SinComp structural analyses, as described in **Fig. 1**,
239 towards quantitative elucidation of the features of the mitochondrial networks and non-networks
240 after TCDD exposure**.** Consistent with **Fig. 2D**, particularly T1-1h exposure reduces the average
241 length of both networked and non-networked mitochondria within individual cells, while T10-1h
242 exposure modestly reduces the network length only **(Fig. 2E, Fig. S3D-G)**. Thus, the data clearly
243 demonstrates that T1-1h dose reduces the length of the overall mitochondrial population likely
244 through modulation of fission, unlike T10-1h. Furthermore, the distribution of the [CRL mito-Net]
245 metric demonstrates that in comparison to Tol-1h exposure, T1-1h exposure increases the cell-
246 relative length of the mitochondrial networks, which happens to a lesser degree with T10-1h
247 exposure **(Fig. 2F, left)**. The distribution of [CRL mito-nonNet] and individual mitochondrial length
248 (networked and non-networked) remain largely comparable between the groups **(Fig. 2F, right,**
249 **Fig. S3H)**. Importantly, [CRL mito-Net] based classification **(**as in **Fig. 1D)** reveals remarkable
250 enrichment of SMNs and concomitant depletion of the HMNs specifically with T1-1h exposure, in
251 comparison to the Tol-1hr exposure **(Fig. 2G).** T10-1h exposure exhibits lesser specificity of
252 enrichment and depletion of SMNs and HMNs, respectively. This data strongly suggests that the
253 HMNs are promptly converted to SMNs particularly with T1-1h exposure.

254 Analyses of various structural metrics reveal that the overall SMNs remain heterogenous
255 in their thickness and their network complexity (nodes or edge density) even after T1-1h or T10-
256 1h exposure **(Fig. 2H, Fig. S3I-J).** Whereas, T1-1h exposure dramatically reduces the network
257 size and the number of nodes and edges of the HMNs, almost to the level of the SMNs (lower
258 abundance of HMNs compromises the statistical significance assessment through multiple
259 hypothesis testing). Notably, T1-1h exposure does not impact the size of the individual
260 mitochondrial elements within the networks **(Fig. 2H).** These observations corroborate the T1-1h
261 induced conversion of HMNs to SMNs (**Fig. 2G**), and further demonstrate that the conversion
262 happens particularly by modulating the organization of the nodes and edges of the HMNs.
263 Moreover, T1-1h exposure also reduces the network size of the SMNs and substantially elevates
264 their level and heterogeneity of the network complexity, while T10-1h has modest or no impact
265 **(Fig. 2H)**. In contrast, the dose dependent effect of T1-1h and T10-1h exposure is seen in their
266 modest reduction of SMN thickness **(Fig. 2H)**.

267 Taken together, our mito-SinComp structural analyses demonstrate that the stem cell
268 enriching TCDD dose (T1-1h) promptly converts the HMNs to SMNs of greater network
269 complexity and heterogeneity, thus enriching these SMNs. Our data suggest that T1-1h, which
270 elevates the [Fission] metric, alters network organization of the HMNs by modulating their nodes
271 and edges to convert them to more complex SMNs. This could be brought about by regulated
272 fission events at the mitochondrial nodes. Noteworthily, the SMNs do not further disassemble into
273 smaller elements suggesting a possible role of counteracting mitochondrial fusion events in
274 maintaining the SMNs. Our data also highlights involvement of robust mitochondrial
275 depolarization in the SMN enrichment process, although the cause-and-effect relationship
276 remains to be elucidated.

277

278 **Acute-1h exposure to stem cell enriching carcinogen sustains an intermediate level of**
279 **oxidative status in the SMNs of restricted network complexity**

280 Precise redox regulation is crucial for stem cell maintenance as well as for neoplastic
281 transformation (48, 49). Long term TCDD exposure causes oxidative stress which has been
282 linked to its carcinogenicity (50–52). Here, we probed into the involvement of TCDD induced
283 mitochondrial redox changes that could arise due to mitochondrial depolarization **(Fig. 2A)**.
284 Therefore, we studied the impact of Tol-1h (vehicle control), T1-1h (stem cell enriching dose), and
285 T10-1h (control dose) on the relationship between mitochondrial redox status and their network
286 properties using mito-SinComp structure-function analyses **(Fig. 2B).** Here, the redox function is
287 measured in the mitochondrial networks and non-networks identified in **Fig. 2**. We used our
288 previously validated combination of genetically encoded general redox probe for mitochondrial
289 matrix, mito-roGFP, and mitochondrial structural probe mito-PSmO2 (30) **(Fig. 3A)**. Mito-
290 SinComp redox analyses generates [Oxidation] values for individual mitochondrial network and
291 non-network, which can be averaged to obtain the $[\text{Oxidation}]_{Av}$ values of an individual cell (see
292 Main and Supplementary Methods for details). We validated the automated mito-SinComp
293 intensity measurements by their strong linear correlation with those obtained manually using
294 standard image analyses software of select single mitochondrial components **(Fig. S4A-B)**;
295 weaker linear correlation of averaged values of all single mitochondria within single cells indicates
296 heterogeneity of intracellular mitochondrial signal. Nonetheless, the $[\text{Oxidation}]_{Av}$ values per cell
297 for populations exposed to Tol, T1 and T10 for 1 and 4 hours obtained by automated mito-
298 SinComp overall match with that obtained manually from standard image analyses software **(Fig.**
299 **S4C)**.

300 Consistent with dramatic mitochondrial depolarization with 4 hours exposure to TCDD
301 **(Fig. 2A)**, we noted an overall decrease in mitochondrial $[\text{Oxidation}]_{Av}$ per cell with such exposure
302 **(Fig. S4C)**. However, the unique T1-1h induced depolarization **(Fig. 2A)** associates with a trend
303 in increase in the median [Oxidation] within individual cells **(Fig. S4C)**, networks and non-
304 networks **(Fig. 3B-C)**. HMNs exhibit a striking increase in [Oxidation] with T1-1h exposure (**Fig.**
305 **3C**), which is consistent with the pronounced impact of T1-1h on the structural features of the
306 HMNs towards converting them to SMNs (**Fig. 2**) (the data remains compromised in statistical
307 significance assessment due to lower number of HMNs). Furthermore, the apparent bimodal
308 distribution of [Oxidation] in the SMNs of the Tol-1h and the T1-1h groups reduces to a unimodal
309 distribution in the T10-1h group (**Fig. 3C**). To tease out the heterogeneity associated with the
310 bimodal distribution of oxidative status within the SMN population, we divided the distribution into
311 [Oxidation]-Hi / Int / Lo zones; zone demarcations were defined using the level of minimum
312 abundance between the two peaks of Tol-1h control **(Fig. 3C,** dashed orange line**)** and its
313 distance to the upper quartile level of the T10-1h control **(Fig. 3C,** solid orange lines**)**. The impact
314 of the T1-1h on reduction of SMN size and elevation of their network complexity ([Nodes or Edge
315 density]) (**Fig. 2**) is observed in all the 3 zones (**Fig. 3D**). However, the trend in pronounced
316 reduction of number of elements within individual networks is limited to the [Oxidation]-Int zone
317 (**Fig. S4D**). To probe further, we performed bivariate structure-function analyses between
318 [Oxidation] and individual structural parameters of the SMNs and quantified their abundance in
319 the defined [Oxidation] zones. We noted that the [Oxidation]-Int zone is overall enriched (~1.7 X)
320 with T1-1h induced SMNs and [Oxidation]-Lo zone is enriched (~2X) with T10-1h induced SMNs,
321 with respect to the Tol-1h group **(Fig. 3E,** % distribution on the right**)**. Interestingly, the bivariate
322 plot between [Node or Edge density] and [Oxidation] appears to be unique from other structural
323 parameters **(Fig. 3E, S4E)**. Particularly, the SMNs are primarily restricted within a lower level of

[Node or Edge density] only in the [Oxidation]-Int zone (**Fig. 3E**, vertical dashed line), with maximal nodal connectivity also restricted in this redox zone **(Fig. S4D-E)**. In contrast, the other structural parameters do not exhibit restricted distribution in the [Oxidation]-Int zone **(Fig. S4E)**.

Therefore, our mito-SinComp structure-function analyses is able to quantitively tease out mitochondrial heterogeneity, while strongly demonstrating an association of mitochondrial redox levels particularly with mitochondrial network complexity ([Nodes or Edge density]). Moreover, our data demonstrates that acute exposure to particularly the stem cell enriching dose of TCDD (T1-1h) increases the abundance of SMNs at an intermediate level of oxidative status. Although such exposure increases the overall SMN network complexity, the redox tuned SMNs in the intermediate redox level have restricted network complexity. In the subsequent sections, we test if the early enrichment of the complex and redox tuned SMNs underlie the mitochondrial priming of stemness driven neoplastic transformation.

Acute-2.5h exposure to stem cell enriching carcinogen upregulates mtDNA genes while connecting transcriptomes for mitochondrial energetics and cell cycle exit

Maintenance of mitochondrial fission at a goldilocks level maintains stemness gene expression profile established by TCDD-1nM driven transformation in the HaCaT keratinocyte cell model (20). Here, we asked if the HMN to SMN conversion by T1-1h exposure, achieved with mitochondrial depolarization and increase in mitochondrial fission **(Figs. 2-3),** can lead to altered gene expression towards priming of neoplasticity. Therefore, we performed scRNA-seq of HaCaT cells promptly following SMN enrichment i.e. after 2.5 hrs exposure to Tol (vehicle control), T1 (stem cell enriching dose) and T10 (control dose).

First, we performed pairwise pseudo-bulk analyses of the scRNA-seq data to study the impact of TCDD on overall gene expression **(Fig. S5A)**. Interestingly, the TCDD induced functional stemness gene, Aldh1A3 (38, 53) is comparably upregulated with T1-2.5h or T10-2.5h exposure, while upregulation of canonical TCDD target gene, *CYP1B1* (54), is detected only with T10-2.5h **(Fig. S5B)**. Furthermore, the nuclear genes encoding mitochondrial proteins from MitoCarta database (55) were overall downregulated by both T1-2.5h and T10-2.5h with respect to Tol-2.5h **(Fig. 4A)**. Although T10-2.5h downregulates a substantially greater number of genes for mitochondrial proteins, T1-2.5h specifically downregulates PHB (maintains mitochondrial shape and mtDNA, (56–58), ATP5F1E (regulates energetics, (59) and C1QBP (regulates mitochondrial protein synthesis (60, 61) (**Fig. 4A**, empty triangles). On the contrary, genes encoded by the mitochondrial DNA (mtDNA) heavy strand were upregulated particularly by T1-2.5h exposure (represented by 5 mtDNA genes detected in the data set, **Fig. 4A**); the singular gene encoded by the mtDNA light strand (*MT-ND6)* was downregulated by T10-2.5h. Estimation of protein levels confirmed that TCDD impacts the mtDNA encoded proteins differently than the nuclear DNA encoded mitochondrial proteins (exemplified by MT-CYB and NDUFB3, filled triangles in **Fig. 4A**). Similar to the scRNA-seq findings, T1-2.5h or T10-2.5h exposure caused a modest increase or a dramatic reduction in MT-CYB levels, respectively, with no impact of TCDD on NDUFB3 **(Fig. 4B-C)**; the difference between the protein and mRNA levels could be due to little turnover of NDUFB3 protein within 2.5 hours of exposure. Next, we performed GSEA based functional annotation of all differentially expressed genes from the pairwise pseudo-bulk analyses of the scRNA-seq data **(Fig.S5A, Suppl Data. 2).** We found that both T1-2.5h or T10-2.5h

exposure downregulate genes involved in mitochondrial energetics and cell cycle, confirming TCDD driven cell cycle exit (34–39); the fewer upregulated mtDNA genes were not detected in any functional category **(Fig. 4D, Suppl. Data 2)**. On the other hand, the T10-2.5h driven upregulation cell signaling genes are not observed with T1-2.5h.

Next, to study the cell cycle exit related transcriptomic interaction of the mitochondrial energetics genes and cell cycle genes we performed hdWGCNA with the gene set of pairwise T1 / T10 vs Tol analyses described above. Relevantly, we probed into the presence mitochondrial energetics genes (MitoCarta) and cell cycle genes (REACTOME) among the top 20 hub genes of the identified transcriptomic interaction modules identified by hdWGCNA. Among the modules obtained with gene set from the (T1 vs Tol)-2.5h analysis, maximum number of MitoEnergetics (10) genes exhibit transcriptomic interaction with CellCycle (10) genes during cell cycle exit **(Fig. 4E,** boxed**)**. On the other hand, with the gene set from the (T10 vs Tol)-2.5h analysis, the T1-2.5h and T10-2.5h groups were comparable for the mitoEnergetics-CellCycle transcriptomic interaction modules **(Fig.S5C)**. Moreover, the gene connectivity within the cell cycle exit related [mitoEnergetics-CellCycle] modules are strikingly complex in the above two T1-2.5h groups in comparison to that of the T10-2.5h group, as reflected by the markedly higher number of edges in their hub-gene network plots **(Fig. 4F)**. Interestingly, within the T1-2.5h-mitoEneregetics-CellCycle-A module, the glycolytic enzyme GAPDH, with maximum degree connectivity **(Fig. S5D)**, connects the mitoEnergetics and CellCycle genes. Notably, we did not detect any of the mtDNA genes in any mitoEnergetics-CellCycle modules although mtDNA genes are integral part of mitochondrial energetics circuitry.

Taken together our data demonstrates that acute exposure to particularly the stem cell enriching TCDD dose (T1-2.5h) upregulates mtDNA heavy strand genes while causing cell cycle exit (reflected by downregulation of cell cycle genes). Our data indicates that mtDNA genes and mitoEnergetics-CellCycle transcriptomic network, induced promptly with the establishment of the redox tuned SMNs (**Fig. 2-3**), prime the initiation of neoplastic transformation driven by stem cell enriching carcinogen dose (20).

Acute-2.5h exposure to stem cell enriching carcinogen establishes mtDNA-KRT15(stemness) transcriptomic interaction in non-transformed proliferating cells prior to their cell cycle exit

Keratin-15 (KRT15) is a well-known functional marker for epidermal stem cells, particularly in the keratinocyte lineage (46). We previously reported that TCDD-1nM induced enrichment of quiescent-neoplastic-KRT15^{hi}-stem-cells happens with concomitant decrease in cells with lower expression of mt-DNA genes in keratinocytes (20). Here we investigated if the acute upregulation of mtDNA genes particularly by T1-2.5h exposure **(Fig. 4A)** is linked to KRT15 expression.

First, we performed scRNA-seq analyses to detect any emergence of the KRT15^{hi} stem cell cluster with exposure to Tol-2.5h (vehicle control), T1-2.5h (stem cell enriching dose) and T10-2.5h (control dose). We identified the cell clusters on a UMAP plot, quantified their abundance **(Fig.5A, Fig.S6A)**, and assigned cluster functionality by GSEA on their respective gene markers **(Fig.S6B, Suppl. Data 3)**. Consistent with TCDD induced overall cell cycle exit **(Fig. 4D),** we found reduced abundance of the CellCycle^{hi} i.e. 'Proliferating' cells and increase in

410 that of the CellCycle^{lo} i.e. 'CC-Exiting' cells with both T1-2.5h or T10-2.5h exposure (**Fig.5A,**
411 **Fig.S6A)**. Noteworthily, of all 18 members of KRT family genes, the contribution of the stem cell
412 gene KRT15 is prominently highest in defining the CC-Exiting cluster due to its upregulation in the
413 cells of this cluster **(Fig. 5B**, **Fig. S6C)**. This data suggests that the commencement of stemness
414 (defined by KRT15 expression) is linked to cell cycle exit happening within 2.5 hours of TCDD
415 exposure. Therefore, we re-designated the CC-Exiting cluster as CC-Exiting-K15^{hi} **(Fig. 5A)**.
416 Additionally, T1-2.5h and T10-2.5h exposure reduce the abundance of 'Cytokine' producing cells,
417 and modestly increase the number of 'Differentiated(KRTs)' cells (designated based on
418 downregulation of cell cycle genes along upregulation of multiple keratin family genes).
419 Noteworthily, the T1-2.5h driven upregulation of mtDNA heavy strand genes (**Fig. 4A**) happens
420 across all cell clusters with maximum in Proliferating cells and minimum in CC-Exiting-K15^{hi} cells
421 **(Fig. 5C, Fig.S6D).** This data suggests a direct impact of T1-2.5h on mtDNA gene expression
422 that is likely mediated through the mitochondrial structure-function alterations **(Fig. 2-3).** Notably,
423 MT-ND1, MT-ND4 and MT-ND5, crucial components of the major site of mitochondrial ROS
424 production namely Complex I (62), underwent the most prominent increase with T1-2.5h
425 exposure that was not detected in T10-2.5h exposure (**Fig. 5C,** boxed). The components of
426 Complex III and IV are upregulated with both T1-2.5h and T10-2.5h exposure, although more with
427 the former.

428 Next, we aimed at identifying any mtDNA gene co-expression modules with KRT15
429 and/or other relevant genes within each cell cluster using hdWGCNA and further assigned
430 functionality to the listed modules using GSEA **(Fig. S7A, Suppl Data 3).** Expectedly, the distinct
431 mtDNA (see Methods for reassignment) and the CellCycle modules are identified in almost all cell
432 clusters across the Tol-2.5h, T1-2.5h and T10-2.5h groups **(Fig. 5D, S7B-D)**. Importantly, the
433 mtDNA genes are found to interact with the stem-cell gene KRT15 only in the Proliferating cells of
434 the T1-2.5h group **(Fig. 5C,** boxed**)**. Notably, KRT15 is downregulated in the Proliferating cells
435 that exhibits maximum upregulation of mtDNA genes (**Fig. 5B-C**). Furthermore, the mtDNA-
436 KRT15 interaction module includes the gene HES1 **(Fig. 5C)**, which is regulated to maintain
437 quiescence (20, 63, 64) and was dramatically upregulated in T1 induced quiescent-KRT15^{hi}-
438 stem-cell enriched transformed population (20). Hub-gene network analyses of the mtDNA-
439 KRT15 module reveals a distinct network of interacting mtDNA genes, out of which only redox
440 related MT-ND1 is directly connected to KRT15 **(Fig. 5E-F)**. In turn, within the T1-2.5h-
441 Proliferating-mtDNA-KRT15 module, KRT15 is directly connected to meaningful partners namely
442 its paralog KRT19, SERPINB13 of keratinocyte lineage (65), quiescence regulator HES1 (20, 63,
443 64) and redox scavenger GPX2 (66) **(Fig. 5E-F)**.

444 Taken together, these data demonstrate that following enrichment of the redox tuned
445 SMNs by the stem cell enriching TCDD exposure, the redox relevant mt-ND1(Complex I)-
446 KRT15(stemness) transcriptomic interaction is established in the proliferating cells before they
447 exit cell cycle. Our findings also indicate that cell cycle exit related upregulation in KRT15 is
448 linked to downregulation of mtDNA genes, which commences establishment of the reciprocal
449 relationship of the KRT15^{hi} and the mtDNA^{lo} clusters observed in the stem cell enriched T1
450 transformed population (20). These results suggest that such mtDNA-KRT15 transcriptomic
451 interactions established after SMN enrichment and prior to TCCD induced cell cycle exit underlie
452 the priming of stemness within the first 3 hours of exposure only to the low carcinogen dose.

453

454 T**ransformation with stem cell enriching carcinogen sustains SMN enrichment and**
455 **maintains the mtDNA-KRT15 transcriptomic interaction particularly in late S phase.**

456 Carcinogens, including TCDD, lead to neoplastic transformation after prolonged exposure
457 (50–52). We investigated if the priming related SMN enrichment **(Fig. 2)** and the mtDNA-KRT15
458 transcriptomic interaction established by the stem cell enriching TCDD dose **(Fig. 5)** is sustained
459 even after neoplastic transformation. Here, we performed mito-SinComp and hdWGCNA
460 analyses of our published mito-SinCe and scRNA-seq datasets, respectively, of HaCaT cells
461 transformed by 1nM or 10nM TCDD (TF1**,** stem cell enriched or TF10, control dose) using the
462 non-transformed Parental (P) controls as necessary (20).

463 Similar to the cells with T1-1h or T10-1h acute exposure **(Fig. 2F)**, SMN and HMN
464 abundance is distinctly different between the TF1 and TF10 cell populations, as demonstrated by
465 mito-SinComp structural analyses **(Fig. 6A, Fig. S8A)**. However, TF1 cell population exhibits
466 enrichment of both SMNs and HMNs in individual transformed cells **(Fig. 6A)**, in contrast to the
467 marked conversion of HMN to SMNs by acute T1-1h exposure **(Fig. 2F)**. This suggests that
468 HMNs re-occurred in the TF1 cells after the priming event during the transformation process.
469 Nonetheless, the SMNs maintain higher heterogeneity than the HMNs, most prominently in their
470 network complexity (Edge/Node Density) **(Fig. 6B)**. Also, TF1 SMNs maintain higher
471 heterogeneity and are modestly thinner in comparison to those of the TF10 SMNs **(Fig. 6B, S8B)**.
472 However, in contrast to the cells undergoing priming by T1-1h dose, the properties of HMNs in
473 TF1 group are distinct from the SMNs in that group and remain more comparable to those of
474 TF10 group **(Fig. 6B, S8B)**. Next, we quantified the relative abundance of SMNs over HMNs in
475 each cell **(Fig. 6C, Fig. S8C).** We found that 29% of TF1 and 15% of TF10 cells harbor greater
476 number of SMNs than HMNs (" %SMN / %HMN " >1.1) whereas 64% TF1 and 80% of TF10 cells
477 harbor greater number of HMNs than SMNs (" %SMN / %HMN " <0.9) **(Fig. 6D)**. These data
478 together suggest that neoplastic transformation with long term exposure to the stem cell enriching
479 T1 dose allows one third of the transformed cells (TF1) to maintain abundance of SMNs that
480 retain heterogeneity in their network properties. In contrast, such a phenotype is substantially
481 weaker in cells transformed with long term T10 exposure (TF10).

482 Next, we addressed if the SMN enrichment in the TF1 cells are linked to any mtDNA-
483 KRT15 transcriptomic interaction module. Pairwise pseudobulk-RNAseq analyses of the TF1 and
484 TF10 cells in comparison to the parental cells confirmed the key observation of the T1-1h or T10-
485 1h exposure (**Fig. 4A**). Particularly, the SMN enriched TF1 population exhibits specific
486 upregulation of mtDNA heavy strand genes encoding components of Complex I and
487 downregulation of the mtDNA regulator PHB, which is not observed in the TF10 population **(Fig.**
488 **6E)**. Notably, the MT-ND1 gene with direct transcriptomic connection to KRT15 gene **(Fig. 5E, F)**
489 is downregulated in TF10 along with other mtDNA genes **(Fig. 6E).** On the other hand, the
490 nuclear genes encoding mitochondrial proteins showed a similar trend between the TF1 vs P and
491 TF10 vs P comparative groups **(Fig. S8D).** Importantly, hdWGCNA performed with the gene sets
492 obtained from the TF1 vs P analyses identified the lineage specific stem cell genes KRT15 and
493 SOX4 exclusively in one of the modules of the SMN and stem cell enriched TF1 population **(Fig.**
494 **S8E, boxed)**; only two mitochondrial energetics genes, other than the mtDNA genes, were
495 detected in the identified modules**.** In contrast, corresponding hdWGCNA performed for the gene
496 set obtained from the TF10 vs P analyses did not show any such interactions although one
497 module with mtDNA genes was identified **(Fig. S8E, bottom).**

498 TCDD driven carcinogenesis of keratinocytes models cutaneous squamous cell
499 carcinoma (cSCC) (50–52). Therefore, we aimed at confirming the distinction of mtDNA genes
500 observed between TF1 and TF10 population in the available scRNA-seq data from SCC patient
501 samples (67). We performed pairwise pseudo-bulk RNA-seq analyses of average expression of
502 mtDNA and other relevant genes between cutaneous SCC tumor and adjacent tissue available
503 from patients. A total of 9 out of 10 patients exhibit decrease in mtDNA in the tumors in
504 comparison to the adjacent normal tissue **(Fig. 6F, top panel).** This confirms our observation with
505 TF10 cells that form xenografts with SCC features (20). These patients also showed a decrease
506 in keratin genes in the tumor suggesting reversal of differentiation in the tumor cells **(Fig. 6F,**
507 middle panel, boxed**).** In contrast, one patient exhibits already low levels of keratin genes in the
508 adjacent normal tissue that does not further change in the tumor, suggesting a different state of
509 the normal cells **(Fig. 6F,** boxed**)**. Interestingly, this singular patient also exhibits prominent
510 increase in mtDNA genes in the tumor **(Fig. 6F,** boxed**),** similar to the SMN and stem cell
511 enriched TF1 cells that forms xenografts of primitive nature with lower tumor incidence (20).
512 Notably, the behavior of the nuclear encoded gene for the mitochondrial protein NDUFB3 (used
513 as control in **Fig. 4B-C)** is similar across all the 10 patients (**Fig. 6F**).

514 Next, we aimed at identifying the transcriptomic interaction modules in individual cell
515 clusters identified by scRNA-seq analyses of our published Parental (P), SMN and stem cell
516 enriched TF1 and TF10 cell populations, where the S-Late cells transition to the quiescent-
517 neoplastic-KRT15^{hi}-stem-cells (20). Therefore, we performed hdWGCNA on each cell cluster of
518 the TF1 and TF10 transformed populations to conclude about transcriptomic interaction in
519 transformed cells. Interestingly, among all the cell cycle stages detected (**Fig. S8F**), only the S-
520 Late cells of the TF1 population exhibit the relevant mtDNA-KRT15 direct transcriptomic
521 interaction in one module **(Fig. 6G-I).** In the TF1 population, KRT15 directly interacts with both
522 Complex I and Complex III components, namely MT-ND1 and MT-CYB, respectively. In contrast,
523 no direct mtDNA-KRT15 connections are detected in the identified less complex mtDNA-KRT15
524 transcriptomic modules of the Cytokine expressing cells of the TF1 and TF10 populations **(Fig.**
525 **6H-I).** Importantly, only the late S phase cells of the TF1 population harbour an mtDNA-KRT15-
526 HES1 transcriptomic interaction **(Fig. 6I),** which was detected with T1 exposure **(Fig. 5E).** Taken
527 together, our data demonstrates that the MT-{ND1 / CYB} -KRT15 transcriptomic interactions
528 established in the late S phase are linked to the cell cycle exit to maintain the quiescent-
529 neoplastic-KRT15^{hi}-stem-cells in the TF1 population.

530 In summary, our results demonstrate that the early SMN enrichment, the associated
531 upregulation of mtDNA genes and the mtDNA-stemness transcriptomic interaction of the non-
532 transformed proliferating cells continue to sustain even after neoplastic transformation. The
533 mtDNA-stemness transcriptomic interaction is particularly detected in the late S phase cells and
534 is potentially linked to cell cycle exit to maintain the quiescent neoplastic stem cells (20). In the
535 transformed population, MT-ND1(Complex-I)- KRT15(stemness) and MT-CB5(Complex-III)-
536 KRT15(stemness) transcriptomic interactions are detected, implicating both the complexes for
537 mitochondrial ROS production (62). Our patient sample analyses also provide key validation of
538 the data from our cell line model, while also highlighting patient heterogeneity in the potential
539 mitochondria driven priming status of individuals.

540

541

Discussion

Studies on mitochondrial heterogeneity have revealed a more complex role of mitochondria in cancer and other pathophysiological conditions (1, 5, 14, 68, 69). Quantitative understanding of mitochondrial heterogeneity is required to elucidate the precise involvement of mitochondria on cellular pathophysiology. Here we tease out the significance of the intracellular mitochondrial heterogeneity in cancer initiation by developing and employing a quantitative analytical method for studying structure-function of single mitochondrial components. This mito-SinComp analysis distinguishes the physical mitochondrial networks from non-networks, identifies the "Small Mitochondrial Networks (SMNs)' and the Hyperfused Mitochondrial Networks (HMNs), and characterizes their structure-function properties**.** We further link findings from mito-SinComp analyses to stemness transcriptomic network involving mtDNA, by employing hdWGCNA on scRNA-seq data. Based on our findings from cell populations with early exposure to the model carcinogen TCDD and their neoplastic counterparts, we propose that early enrichment of redox-tuned small networks of mitochondria primes neoplasticity by establishing mtDNA-stemness transcriptomic network even prior to cell cycle exit towards generating quiescent neoplastic stem cells **(Fig. 7).**

First, we detect enrichment of characteristically heterogenous SMNs linked to the transcriptomic network of the functional stem cell gene KRT15 in a non-transformed keratinocyte population **(Fig. 1)** where stemness was modulated by genetic manipulation of mitochondrial fission (20). Next, we demonstrate that the HMNs of the non-transformed keratinocytes are promptly converted to heterogenous and complex SMNs when the cells are exposed to low dose of the model carcinogen TCDD (**Fig. 2**) that enriches KRT15^{hi} neoplastic stem cells during transformation (20). HMN to SMN conversion is associated with dramatic mitochondrial depolarization and is brought about by modulation of the nodes and edges of the HMNs. The resulting heterogenous SMNs have their redox levels particularly linked to their network complexity (i.e. density of nodes and edges) (**Fig. 2,3**). Such early SMN enrichment is promptly followed by upregulation of mtDNA genes and establishment of a mtDNA-KRT15 transcriptomic interaction in the proliferating non-transformed cells prior to their cell cycle exit **(Fig. 4, 5).** The neoplastic stem cell enriched transformed population indeed sustains the SMN enrichment while the mtDNA-KRT15 transcriptomic interaction is detected particularly in the Late-S phase before cell cycle exit **(Fig. 6).** Importantly, the control TCDD dose that does not cause pronounced enrichment of KRT15^{hi} stem cells (20) is not able to cause the pronounced early enrichment of SMNs and fails to establish the mtDNA-KRT15 transcriptomic interaction **(Figs 2-6).** The key data of the model carcinogen induced modulation of mtDNA-KRT15 gene expression from the model keratinocyte lineage is recapitulated in cSCC patient tumors, with notable patient heterogeneity. **(Fig. 6F).** This data implies that modulation of mt-DNA gene expression in cSCC patients could be an early event of mitochondria driven priming of their tumor development.

Network forming ability of mitochondria may help in precise mitochondrial quality control, equilibration or maintenance of mtDNA and other mitochondrial contents, in transmitting signal or analytes efficiently through various parts of the cell and may also have provided evolutionary advantage (70–73). However, the precise mechanism of formation of mitochondrial networks and their control by mitochondrial fission and fusion events remain largely unknown. The mito-SinComp analyses of single mitochondrial networks and non-networks suggested a mechanism of conversion of HMNs to SMNs. To form the SMNs, the stem cell enriching carcinogen primarily

587 reorganizes the HMNs at the level of nodes and their connected edges, while largely retaining the
588 length of the mitochondrial elements **(Fig. 1F, 2H).** Such a mechanism would involve induction of
589 mitochondrial fission particularly at the nodes of the HMNs. Consistently, stem cell enriching
590 carcinogen elevates the [Fission] metric **(Fig.2D),** which can be potentially triggered by activation
591 of Drp1 driven mitochondrial fission (not shown). Thus, active levels of mitochondrial fission in the
592 cells with weaker Drp1 knockdown are able to enrich the SMNs **(Fig 1J).** Therefore, our data
593 indicates that marked inhibition of neoplastic transformation by obliteration of Drp1 activity (20,
594 40, 41) may be due to inhibition Drp1 driven fission at nodes of the HMNs, thus preventing their
595 conversion to the SMNs.

596 Enrichment of SMNs implies that their breaking down into individual mitochondrial
597 elements is prevented, which can be brought about by repressed Drp1 activity in concert with
598 counteracting fusion proteins. This conception of mitochondrial fission and fusion cycles
599 reconciles various apparently contradictory findings where fission or fusion regulators have been
600 causatively linked to stem cell regulation (19–21, 32, 33, 74–76). We speculate that the
601 mitochondrial fission and fusion cycles involved in SMN generation and maintenance could
602 modulate the reductive metabolism sustained by the P5CS enzyme in the regions of reduced
603 ATP synthase activity (14), which could be in the mitochondrial zones of reduced ATP synthesis
604 we found in ~10% of some cancer cells (30). Indeed, we found reduction of ATP5F1E gene
605 expression in association with SMN enrichment and mtDNA-KRT15 interaction **(Fig. 4A)**.
606 Moreover, fine-tuned repression of Drp1 that primes stemness (20) also elevates expression of
607 P5CS in the mtDNA^{lo} cell cluster (not shown).

608 It is reasonable to speculate that reduction in ATP synthesis is induced by mitochondrial
609 priming related mitochondrial depolarization that is linked to the prompt conversion of HMNs to
610 SMNs within one hour of carcinogen exposure. Studies with higher temporal resolution would
611 reveal if mitochondrial depolarization precisely controls assembly of fission sites at the HMNs
612 nodes (possibility A in **Fig. 7**), or mitochondrial fission driven removal of network elements
613 depolarizes the SMNs (possibility B in **Fig. 7**). Nonetheless, such precise regulation of the
614 mitochondrial fission and/or fusion events may the involve PHB that regulates mitochondrial
615 shape and mtDNA (77, 78), that is altered particularly during mitochondrial priming **(Fig. 4A)** and
616 after neoplastic stem cell enrichment **(Fig.6E).** It is clear that mtDNA aberrations impact
617 stemness (79, 80), while greater than two-fold elevation of mtDNA copy number occurs during the
618 differentiation of stem cells of various lineages (3 and references therein). Our study raises the
619 possibility of a specific mtDNA regulation during cell cycle exit towards maintenance of quiescent
620 stem cells, which could be brought about by Prohibitin or similar molecules.

621 Redox regulation is critical to the development of cancer (48), and mitochondria act as a
622 crucial hub of redox signaling that is controlled by precise regulation of mitochondrial energetics
623 circuitry (2, 81). Although spatiotemporal heterogeneity in mitochondrial redox regulation and its
624 crosstalk with mitochondrial structural properties are well documented (82–84), the quantitative
625 understanding of such redox regulation is missing. The mito-SinComp quantitative approach
626 identified the property of 'network complexity' of the SMNs to be linked to their redox levels
627 **(Fig.2G-H, 3D-E)**, thus revealing formation of SMNs as potential spatio-temporally controlled
628 mechanism related to fine-tuning of redox signaling. In the context of mitochondrial priming of
629 stem cells, our study demonstrates the following 3 aspects of redox regulation. First, the impact of
630 the reportedly oxidative carcinogen TCDD on mitochondrial redox levels varies based on the
631 mitochondrial network status (**Fig. 3B-C**). Second, importance of an intermediate zone of

632 [Oxidation] with restricted network complexity emerges in the concept of priming for stemness
633 **(Figs. 3D,E).** Third, TCDD driven mitochondrial priming involves interaction of the stemness gene
634 KRT15 and mitochondrial Complex I (**Fig. 5E**, **Fig. 6I**) or Complex III (**Fig. 6I**) that are the main
635 sites of mitochondrial ROS production (62). These observations raise the possibility that SMN
636 driven tuning of redox signalling may be important towards maintaining stemness gene
637 expression profile, given either elevating or reducing the tuned redox levels of stem cells disrupts
638 their self-renewal, proliferation or differentiation properties (85–87).

639 Redox regulation of S phase of cell proliferation cycle has been documented (88–92).
640 Cell cycle exit and acquisition of quiescence is critical to maintaining stem cell pool and
641 functionality (93). Here, we note that upregulation of mtDNA genes during TCDD driven priming
642 happens as transcriptomic interactions are established between cell cycle and mitochondrial
643 energetics genes (**Fig. 4 D-F**). Moreover, the MT-ND1-KRT15 transcriptomic interaction
644 established before non-transformed cells exit cell cycle during TCDD driven priming, is
645 particularly detected in Late-S phase in the transformed population (**Fig. 5D-F, 6G-I**). Our
646 previous analyses shows that enrichment of KRT15^{hi} population happens with decrease of its
647 reciprocal mtDNA^{lo} cell population, and the cellular decision of this bifurcation is likely made in the
648 Late-S phase cells (20). Therefore, it can be speculated that the MT-ND1-KRT15 transcriptomic
649 interaction is involved in redox regulated cell cycle exit for enrichment of the quiescent-neoplastic-
650 KRT15^{hi}-stem-cells. The mechanism of such transcriptomic interactions in cell cycle exit may
651 include HES1, as indicated by our finding (**Fig. 5D, Fig. 6I**).

652 In conclusion, based on data obtained with our quantitative combinatorial approach of
653 quantitative microscopy and single cell transcriptomics, we elucidate a biological mechanism of
654 cancer initiation involving stem cells. We propose that conversion of HMNs to SMNs by
655 modulating the complexity of mitochondrial networks is a mechanism of priming non-transformed
656 cells for stem cell driven neoplasticity, as revealed by experimentation with a model carcinogen.
657 Mechanistically, the enriched SMNs would tune the mitochondrial redox balance to support
658 critical transcriptomic interactions required to maintain a stem cell state to support neoplastic
659 transformation. Further testing our fundamental findings in the light of cancer heterogeneity may
660 allow refinement of various proposed mitochondria based targeted cancer therapies (11).
661
662

663 Materials and Methods

664

665 **Cell culture, mitochondrial staining, confocal microscopy, immunoblotting** : Immortalized
666 skin keratinocyte cell line HaCaT cells, the previously derived TCDD transformed lines and the
667 stable lines expressing mito-PSmO2 and mito-roGFP were cultured following standard protocols
668 (20, 44). Appropriate cells were used for individual experiments. Staining of TCDD exposed cells
669 with TMRE or mitotracker green was performed while maintaining TCDD in the staining solution,
670 as described (20). Confocal microscopy for mito-SinCe analyses was performed as described
671 (30). The resulting confocal micrographs were utilized for Mito-SinComp analysis following
672 appropriate quality control steps (30). Immunoblotting was performed with TCDD exposed cells
673 using standard methods using commercial antibodies to NDUFB3, Beta actin (Santa Cruz
674 Biotechnology), MT-CYB (Invitrogen), Tom20 (Cell Signaling Technology), and appropriate
675 secondary antibodies.

676

677 **Development of Mito-SinComp analysis for studying structure-function relationship of**
678 **single mitochondria :** Mito-SinComp analysis for single mitochondrial components is an
679 extension of our previously established single cell analytical approach Mito-SinCe where
680 mitochondrial structural analyses is primarily performed by the open source MitoGraph algorithm
681 (30). To perform Mito-SinComp analyses, we included function analyses for single mitochondrial
682 component identified by MitoGraph within single cells. In brief, the mito-SinComp analysis uses
683 3D confocal micrographs with appropriate combinations of compatible probes reporting
684 mitochondrial structure and function separately. Our customized, modular script for mito-SinComp
685 structure-function analysis comprises several steps (detailed in Supplementary Methods, **Fig.S9**).
686 First, the 'structure' and 'function' channels are identified, followed by the application of
687 MitoGraph for mitochondrial segmentation and structural analysis. Individual mitochondrial
688 components are then delineated to calculate structural properties for both networks and non-
689 networks.

690 The functional analysis for individual networks and non-networks involves converting the
691 MitoGraph output into pixel coordinates and extracting intensity values from the corresponding
692 'function' channels. For validation of the intensity values calculated from MitoSincomp, we used
693 appropriate ImageJ plugin or Zen Blue proprietary software (**Fig.S4B**). These intensity values are
694 further used to calculate average pixel intensity ratios reflecting the redox function in this case.
695 The output of mitoSinComp analyses is a comprehensive data file (*.csv) holding the relevant
696 details for individual mitochondria in individual cells; rows with point_ids under line_ids under
697 cc_ids while columns with relevant values for each id. This file is used to obtain the structural and
698 the functional parameters as well as for creating 3D graphs for visualization. For intra-cellular
699 comparisons of SMNs and HMNs, the *.vtk files generated by MitoGraph for individual cells were
700 analyzed and visualized using the open-source software ParaView-v5.13.0
701 (https://www.paraview.org/).

702 To distinguish between SMNs and HMNs from the mitochondrial population we employed
703 the thresholding approach using the CRL mito-Net metric, in conjunction with the previously
704 defined Cellular Fusion1 metric, a measure of mitochondrial fusion within a cell (calculated as the
705 ratio of the longest component's length to the total length of all components in the cell (30). For
706 the HF-cells group, the Fusion1 metric was calculated for all cells. The cell with the minimum
707 Fusion1 value was identified, and within it, the network with the maximum CRL mito-Net value
708 was used as a threshold to demarcate the boundary between the SMN and HMN zones. The
709 starting point of the SMN zone was defined by the peak of the INT-cells group, reflecting the
710 enrichment of SMNs within this group. (**Fig-1D**). The same threshold was used for all analyses
711 after confirming the distribution of the length parameters for networks and non-networks.

712 All plots were generated in Python using appropriate modules. Quantification of mean
713 fluorescent intensity was performed either automatically using the Mito-SinComp script or
714 manually for each cell using FIJI or proprietary software such as Zen Black and Zen Blue.

715

716 **Single-Cell RNA Seq Analyses and hdWGCNA :** TCDD exposed cells were processed for
717 scRNA-seq using the 10X Genomics platform and analyses was performed using Seurat (v4.3.3),
718 as described before (20). Notably, the cells were tested for > 90% viability before scRNA-seq,
719 and only cells expressing a minimum of 2000 detectable genes were included using

720 ‘nFeature_RNA’ filter. This filtering also excluded dead cells with >10% mtDNA gene expression
721 in all our data sets analyzed. This allowed us to exclude the **percent.mt** filter that uses mtDNA
722 based exclusion of dead cells. Same filters were used for processing publicly available raw data
723 from cSCC patients (67). Seurat objects were processed, integrated, visualized and analysed for
724 relevant downstream analyses including pairwise differential gene expression analyses (using
725 FindMarkers function), cell cluster analyses (using FindAllMarkers function) and Gene Set
726 Enrichment Analysis (GSEA) for cell cluster annotation, using workflow described before (20, 44)
727 **(Suppl Data 2-3).**

728 The WGCNA method identifies transcriptomic networks consisting of multiples modules,
729 with each module having several hub genes (94). We applied this same method for scRNA-seq
730 data using the recently published hdWGCNA method (95). To identify gene co-expression
731 networks hdWGCNA analysis uses integrated Seurat objects for both pseudobulk and cell cluster
732 based analyses. The detailed schematic flowchart of major steps is outlined in **Fig. S10** and
733 details are described in Suppl Methods. In our analyses, we have considered the top 20 / 25
734 genes (ranked by kME) to visualize transcriptomic interactions through hub-gene network plots.
735 Functional annotation of the hdWGCNA modules was performed using GSEA where the modules
736 with ≥ 5 mtDNA genes as the leading-edge genes were reassigned as ‘mtDNA’ in our analyses.
737 Edge distance and the number of edges were quantified using TOM, providing insights into gene
738 connectivity and interaction strength within the network.

739

740 **Statistical Analyses:** Individual experiments were performed at least 3 times, and appropriate
741 statistics were applied. Appropriate statistical analyses for single cell microscopy were conducted
742 using either Excel or Python (SciPy); The Kolmogorov-Smirnov test was applied to histogram and
743 ridge plots; the Mann-Whitney U test to violin and box plots; and the Chi-square test to bivariate
744 scatter plots. Corresponding p-values were calculated and adjusted for multiple hypotheses
745 testing using the Holm-Bonferroni correction method. The hdWGCNA used inbuilt statistical
746 analyses as required.

747

748 **Data Availability:** Data matrices, scripts, and hdWGCNA results will be deposited in public
749 repositories upon publication, to ensure transparency and reproducibility for future research.

750

751 **Acknowledgments**: The research was supported by NIH (R33 ES025662/ES/NIEHS) and DBT-
752 Wellcome Trust India Alliance (IA/S/20/2/505198/WTDBT), DP and BS were supported by NIH
753 (R33 ES025662/ES/NIEHS), SA was supported by DBTRA/2023-24/NE/Ashoka/19, MS was
754 supported by DBT-JRF- DBT/2023-24/Ashoka Uni/2196, BW was supported by DBT-Wellcome
755 Trust India Alliance (IA/S/20/2/505198/WTDBT), BG was supported by DBT/2022-
756 23/ASHOKA/2156. We sincerely thank Akshara Kulkarni, Diya Prasad for their assistance in the
757 execution of the project, and Dr. LS Shashidhara, Dr. Alok Bhattacharya and Dr. Gautam Menon
758 for critically reading the manuscript.

759 ## References
760

761 1. A. Suomalainen, J. Nunnari, Mitochondria at the crossroads of health and disease. *Cell* **187**,
762 2601–2627 (2024).

763 2. C. R. Reczek, N. S. Chandel, ROS-dependent signal transduction. *Curr Opin Cell Biol* **33**, 8
764 (2015).

765 3. S. Agarwala, S. Dhabal, K. Mitra, Significance of quantitative analyses of the impact of
766 heterogeneity in mitochondrial content and shape on cell differentiation. *Open Biol* **14** (2024).

767 4. M. Granath-Panelo, S. Kajimura, Mitochondrial heterogeneity and adaptations to cellular
768 needs. *Nat Cell Biol* **26**, 674–686 (2024).

769 5. S. B. Vafai, V. K. Mootha, Mitochondrial disorders as windows into an ancient organelle.
770 *Nature* **491**, 374–383 (2012).

771 6. I. Martínez-Reyes, N. S. Chandel, Cancer metabolism: looking forward. *Nat Rev Cancer* **21**,
772 669–680 (2021).

773 7. S. Vyas, E. Zaganjor, M. C. Haigis, Mitochondria and Cancer. *Cell* **166**, 555–566 (2016).

774 8. J. J. Loh, S. Ma, Hallmarks of cancer stemness. *Cell Stem Cell* **31**, 617–639 (2024).

775 9. B. C. Prager, Q. Xie, S. Bao, J. N. Rich, Cancer Stem Cells: The Architects of the Tumor
776 Ecosystem. *Cell Stem Cell* **24**, 41–53 (2019).

777 10. C. L. Jones, A. Inguva, C. T. Jordan, Targeting Energy Metabolism in Cancer Stem Cells:
778 Progress and Challenges in Leukemia and Solid Tumors. *Cell Stem Cell* **28**, 378–393 (2021).

779 11. K. Vasan, M. Werner, N. S. Chandel, Mitochondrial Metabolism as a Target for Cancer
780 Therapy. *Cell Metab* **32**, 341–352 (2020).

781 12. B. Spurlock, J. M. A. Tullet, J. L. Hartman, K. Mitra, Interplay of mitochondrial fission-fusion
782 with cell cycle regulation: Possible impacts on stem cell and organismal aging. *Exp Gerontol*
783 **135**, 110919 (2020).

784 13. B. Glancy, Y. Kim, P. Katti, T. B. Willingham, The Functional Impact of Mitochondrial
785 Structure Across Subcellular Scales. *Front Physiol* [Preprint] (2020).

786 14. K. W. Ryu, *et al.*, Cellular ATP demand creates metabolically distinct subpopulations of
787 mitochondria. *Nature 2024* 1–9 (2024). https://doi.org/10.1038/s41586-024-08146-w.

788 15. R. Quintana-Cabrera, L. Scorrano, Determinants and outcomes of mitochondrial dynamics.
789 *Mol Cell* [Preprint] (2023).

790 16. D. C. Chan, Mitochondrial Dynamics and Its Involvement in Disease. *Annual Review of*
791 *Pathology: Mechanisms of Disease* **15**, 235–259 (2020).

17. L. C. Tábara, M. Segawa, J. Prudent, Molecular mechanisms of mitochondrial dynamics. *Nature Reviews Molecular Cell Biology 2024* 1–24 (2024). https://doi.org/10.1038/s41580-024-00785-1.

18. M. Song, K. Mihara, Y. Chen, L. Scorrano, G. W. Dorn, Mitochondrial fission and fusion factors reciprocally orchestrate mitophagic culling in mouse hearts and cultured fibroblasts. *Cell Metab* **21**, 273–286 (2015).

19. J. Prieto, *et al.*, Early ERK1/2 activation promotes DRP1-dependent mitochondrial fission necessary for cell reprogramming. *Nat Commun* **7** (2016).

20. B. Spurlock, *et al.*, Fine-tuned repression of Drp1-driven mitochondrial fission primes a "stem/progenitor-like state" to support neoplastic transformation. *Elife* **10** (2021).

21. X. Zhong, *et al.*, Mitochondrial Dynamics Is Critical for the Full Pluripotency and Embryonic Developmental Potential of Pluripotent Stem Cells. *Cell Metab* **29**, 979-992.e4 (2019).

22. K. Mitra, C. Wunder, B. Roysam, G. Lin, J. Lippincott-Schwartz, A hyperfused mitochondrial state achieved at G1-S regulates cyclin E buildup and entry into S phase. *Proc Natl Acad Sci U S A* **106**, 11960–11965 (2009).

23. S. M. Rafelski, *et al.*, Mitochondrial Network Size Scaling in Budding Yeast. *Science* **338**, 822 (2012).

24. M. Ouellet, G. Guillebaud, V. Gervais, D. Lupien St-Pierre, M. Germain, A novel algorithm identifies stress-induced alterations in mitochondrial connectivity and inner membrane structure from confocal images. *PLoS Comput Biol* **13**, 1–23 (2017).

25. H. S. Ilamathi, *et al.*, A new automated tool to quantify nucleoid distribution within mitochondrial networks. *Scientific Reports 2021 11:1* **11**, 1–14 (2021).

26. A. Rohani, J. A. Kashatus, D. T. Sessions, S. Sharmin, D. F. Kashatus, Mito Hacker: a set of tools to enable high-throughput analysis of mitochondrial network morphology. *Sci Rep* **10** (2020).

27. M. Karbowski, *et al.*, Quantitation of mitochondrial dynamics by photolabeling of individual organelles shows that mitochondrial fusion is blocked during the Bax activation phase of apoptosis. *J Cell Biol* **164**, 493–499 (2004).

28. E. F. Iannetti, J. A. M. Smeitink, J. Beyrath, P. H. G. M. Willems, W. J. H. Koopman, Multiplexed high-content analysis of mitochondrial morphofunction using live-cell microscopy. *Nature Protocols 2016 11:9* **11**, 1693–1710 (2016).

29. A. E. Y. T. Lefebvre, D. Ma, K. Kessenbrock, D. A. Lawson, M. A. Digman, Automated segmentation and tracking of mitochondria in live-cell time-lapse images. *Nat Methods* **18**, 1091–1102 (2021).

30. B. Spurlock, *et al.*, New quantitative approach reveals heterogeneity in mitochondrial structure–function relations in tumor-initiating cells. *J Cell Sci* **132** (2019).

828 31. R. Liang, *et al.*, Restraining Lysosomal Activity Preserves Hematopoietic Stem Cell
829 Quiescence and Potency. *Cell Stem Cell* **26**, 359-376.e7 (2020).

830 32. F. Bonnay, *et al.*, Oxidative Metabolism Drives Immortalization of Neural Stem Cells during
831 Tumorigenesis. *Cell* **182**, 1490-1507.e19 (2020).

832 33. M. J. Wu, *et al.*, Epithelial-Mesenchymal Transition Directs Stem Cell Polarity via Regulation
833 of Mitofusin. *Cell Metab* **29**, 993-1002.e6 (2019).

834 34. L. Perez-Castro, *et al.*, The AHR target gene scinderin activates the WNT pathway by
835 facilitating the nuclear translocation of β-catenin. *J Cell Sci* **135** (2022).

836 35. I. Teino, *et al.*, Impact of AHR Ligand TCDD on Human Embryonic Stem Cells and Early
837 Differentiation. *Int J Mol Sci* **21**, 1–24 (2020).

838 36. A. Der Vartanian, *et al.*, PAX3 Confers Functional Heterogeneity in Skeletal Muscle Stem Cell
839 Responses to Environmental Stress. *Cell Stem Cell* **24**, 958-973.e9 (2019).

840 37. K. P. Singh, F. L. Casado, L. A. Opanashuk, T. A. Gasiewicz, The aryl hydrocarbon receptor
841 has a normal function in the regulation of hematopoietic and other stem/progenitor cell
842 populations. *Biochem Pharmacol* [Preprint] (2009).

843 38. S. Kim, E. Dere, L. D. Burgoon, C. C. Chang, T. R. Zacharewski, Comparative analysis of
844 AhR-mediated TCDD-elicited gene expression in human liver adult stem cells. *Toxicological*
845 *Sciences* **112**, 229–244 (2009).

846 39. V. Shukla, K. Iqbal, H. Okae, T. Arima, M. J. Soares, EFFECTS OF ARYL HYDROCARBON
847 RECEPTOR LIGAND TCDD ON HUMAN TROPHOBLAST CELL DEVELOPMENT. *bioRxiv*
848 (2024). https://doi.org/10.1101/2024.08.27.609205.

849 40. J. A. Kashatus, *et al.*, Erk2 phosphorylation of Drp1 promotes mitochondrial fission and
850 MAPK-driven tumor growth. *Mol Cell* **57**, 537–551 (2015).

851 41. M. N. Serasinghe, *et al.*, Mitochondrial division is requisite to RAS-induced transformation and
852 targeted by oncogenic MAPK pathway inhibitors. *Mol Cell* **57**, 521 (2015).

853 42. D. Tondera, *et al.*, SLP-2 is required for stress-induced mitochondrial hyperfusion. *EMBO J*
854 **28**, 1589–1600 (2009).

855 43. L. C. Gomes, G. Di Benedetto, L. Scorrano, During autophagy mitochondria elongate, are
856 spared from degradation and sustain cell viability. *Nat Cell Biol* **13**, 589–598 (2011).

857 44. S. Agarwala, M. Saini, D. Parker, K. Mitra, Enrichment of carcinogen-driven “mitochondria-
858 primed” human skin stem cells and their identification using single-cell analyses. *STAR Protoc*
859 **4** (2023).

860 45. B. Spurlock, V. S. Hanumanthu, K. Mitra, Strategy of isolating “primed” tumor initiating cells
861 based on mitochondrial transmembrane potential. *Bio Protoc* **11** (2021).

862 46. T. S. Purba, *et al.*, Human epithelial hair follicle stem cells and their progeny: Current state of
863 knowledge, the widening gap in translational research and future challenges. *BioEssays* **36**,
864 513–525 (2014).

865 47. A. R. Fenton, T. A. Jongens, E. L. F. Holzbaur, Mitochondrial dynamics: Shaping and
866 remodeling an organelle network. *Curr Opin Cell Biol* **68**, 28–36 (2021).

867 48. L. B. Sullivan, N. S. Chandel, Mitochondrial reactive oxygen species and cancer. *Cancer*
868 *Metab* **2**, 17 (2014).

869 49. C. L. Bigarella, R. Liang, S. Ghaffari, Stem cells and the impact of ROS signaling.
870 *Development (Cambridge)* **141**, 4206–4218 (2014).

871 50. A. Poland, D. Palen, E. Glover, Tumour promotion by TCDD in skin of HRS/J hairless mice.
872 *Nature* **300**, 271–273 (1982).

873 51. J. Huff, G. Lucier, A. Tritscher, Carcinogenicity of TCDD: experimental, mechanistic, and
874 epidemiologic evidence. *Annu Rev Pharmacol Toxicol* **34**, 343–372 (1994).

875 52. R. Baan, *et al.*, A review of human carcinogens--Part F: chemical agents and related
876 occupations. *Lancet Oncol* **10**, 1143–1144 (2009).

877 53. T. J. Dunn, R. Lindahl, H. C. Pitot, Differential gene expression in response to 2,3,7,8-
878 tetrachlorodibenzo-p-dioxin (TCDD). Noncoordinate regulation of a TCDD-induced aldehyde
879 dehydrogenase and cytochrome P-450c in the rat. *Journal of Biological Chemistry* **263**,
880 10878–10886 (1988).

881 54. P. DiMeglio, *et al.*, Activation of the Aryl Hydrocarbon Receptor Dampens the Severity of
882 Inflammatory Skin Conditions. *Immunity* **40**, 989 (2014).

883 55. S. Rath, *et al.*, MitoCarta3.0: an updated mitochondrial proteome now with sub-organelle
884 localization and pathway annotations. *Nucleic Acids Res* **49**, D1541–D1547 (2021).

885 56. H. Liu, *et al.*, Prohibitin 1 regulates mtDNA release and downstream inflammatory responses .
886 *EMBO J* **41** (2022).

887 57. K. Kasashima, M. Sumitani, M. Satoh, H. Endo, Human prohibitin 1 maintains the
888 organization and stability of the mitochondrial nucleoids. *Exp Cell Res* **314**, 988–996 (2008).

889 58. T. Tatsuta, T. Langer, Prohibitins. *Current Biology* **27**, R629–R631 (2017).

890 59. C. Von Ballmoos, A. Wiedenmann, P. Dimroth, Essentials for ATP synthesis by F1F0 ATP
891 synthases. *Annu Rev Biochem* **78**, 649–672 (2009).

892 60. V. Fogal, *et al.*, Mitochondrial p32 Protein Is a Critical Regulator of Tumor Metabolism via
893 Maintenance of Oxidative Phosphorylation. *Mol Cell Biol* **30**, 1303 (2010).

894 61. M. Yagi, *et al.*, p32/gC1qR is indispensable for fetal development and mitochondrial
895 translation: importance of its RNA-binding ability. *Nucleic Acids Res* **40**, 9717 (2012).

896 62. M. P. Murphy, How mitochondria produce reactive oxygen species. *Biochem J* **417**, 1–13
897 (2009).

898 63. M. Moriyama, *et al.*, Multiple roles of Notch signaling in the regulation of epidermal
899 development. *Dev Cell* **14**, 594–604 (2008).

900 64. L. Sang, H. A. Coller, J. M. Roberts, Control of the reversibility of cellular quiescence by the
901 transcriptional repressor HES1. *Science* **321**, 1095–1100 (2008).

902 65. J. A. Irving, R. N. Pike, A. M. Lesk, J. C. Whisstock, Phylogeny of the serpin superfamily:
903 implications of patterns of amino acid conservation for structure and function. *Genome Res*
904 **10**, 1845–1864 (2000).

905 66. R. S. Esworthy, J. H. Doroshow, F. F. Chu, The beginning of GPX2 and 30 years later. *Free*
906 *Radic Biol Med* **188**, 419 (2022).

907 67. A. L. Ji, *et al.*, Multimodal Analysis of Composition and Spatial Architecture in Human
908 Squamous Cell Carcinoma. *Cell* **182**, 497-514.e22 (2020).

909 68. W. Chen, H. Zhao, Y. Li, Mitochondrial dynamics in health and disease: mechanisms and
910 potential targets. *Signal Transduction and Targeted Therapy 2023 8:1* **8**, 1–25 (2023).

911 69. D. C. Chan, Mitochondrial Dynamics and Its Involvement in Disease. *Annu Rev Pathol* **15**,
912 235–259 (2020).

913 70. M. P. Viana, *et al.*, Mitochondrial Fission and Fusion Dynamics Generate Efficient, Robust,
914 and Evenly Distributed Network Topologies in Budding Yeast Cells. *Cell Syst* **10**, 287-297.e5
915 (2020).

916 71. B. Glancy, *et al.*, Mitochondrial reticulum for cellular energy distribution in muscle. *Nature* **523**,
917 617–620 (2015).

918 72. J. Nunnari, *et al.*, Mitochondrial transmission during mating in Saccharomyces cerevisiae is
919 determined by mitochondrial fusion and fission and the intramitochondrial segregation of
920 mitochondrial DNA. *Mol Biol Cell* **8**, 1233–1242 (1997).

921 73. A. Kowald, T. B. L. Kirkwood, Evolution of the mitochondrial fusion - Fission cycle and its role
922 in aging. *Proc Natl Acad Sci U S A* **108**, 10237–10242 (2011).

923 74. R. Sênos Demarco, B. S. Uyemura, C. D'Alterio, D. L. Jones, Mitochondrial fusion regulates
924 lipid homeostasis and stem cell maintenance in the Drosophila testis. *Nat Cell Biol* **21**, 710–
925 720 (2019).

926 75. M. Khacho, *et al.*, Mitochondrial Dynamics Impacts Stem Cell Identity and Fate Decisions by
927 Regulating a Nuclear Transcriptional Program. *Cell Stem Cell* **19**, 232–247 (2016).

928 76. R. Iwata, P. Casimir, P. Vanderhaeghen, Mitochondrial dynamics in postmitotic cells regulate
929 neurogenesis. *Science* **369**, 858–862 (2020).

930 77. H. Liu, *et al.*, Prohibitin 1 regulates mtDNA release and downstream inflammatory responses.
931 *EMBO J* **41** (2022).

932 78. G. Della-Flora Nunes, *et al.*, Prohibitin 1 is essential to preserve mitochondria and myelin
933 integrity in Schwann cells. *Nature Communications 2021 12:1* **12**, 1–16 (2021).

934 79. M. J. Birket, *et al.*, A reduction in ATP demand and mitochondrial activity with neural
935 differentiation of human embryonic stem cells. *J Cell Sci* **124**, 348–358 (2011).

936 80. J. M. Facucho-Oliveira, J. C. John St., The relationship between pluripotency and
937 mitochondrial DNA proliferation during early embryo development and embryonic Stem Cell
938 differentiation. *Stem Cell Rev Rep* **5**, 140–158 (2009).

939 81. K. M. Holmström, T. Finkel, Cellular mechanisms and physiological consequences of redox-
940 dependent signalling. *Nature Reviews Molecular Cell Biology 2014 15:6* **15**, 411–421 (2014).

941 82. P. H. G. M. Willems, R. Rossignol, C. E. J. Dieteren, M. P. Murphy, W. J. H. Koopman, Redox
942 Homeostasis and Mitochondrial Dynamics. *Cell Metab* **22**, 207–218 (2015).

943 83. W. Wang, *et al.*, Superoxide flashes in single mitochondria. *Cell* **134**, 279–290 (2008).

944 84. Z. Ying, *et al.*, Transient Activation of Mitoflashes Modulates Nanog at the Early Phase of
945 Somatic Cell Reprogramming. *Cell Metab* **23**, 220–226 (2016).

946 85. C. E. Bauer, S. Elsen, T. H. Bird, Mechanisms for redox control of gene expression. *Annu*
947 *Rev Microbiol* **53**, 495–523 (1999).

948 86. M. Fratelli, *et al.*, Gene expression profiling reveals a signaling role of glutathione in redox
949 regulation. *Proc Natl Acad Sci U S A* **102**, 13998–14003 (2005).

950 87. H. Y. Hsu, M. H. Wen, Lipopolysaccharide-mediated reactive oxygen species and signal
951 transduction in the regulation of interleukin-1 gene expression. *Journal of Biological Chemistry*
952 **277**, 22131–22139 (2002).

953 88. J. Chiu, I. W. Dawes, Redox control of cell proliferation. *Trends Cell Biol* **22**, 592–601 (2012).

954 89. J. C. Patterson, *et al.*, ROS and Oxidative Stress Are Elevated in Mitosis during
955 Asynchronous Cell Cycle Progression and Are Exacerbated by Mitotic Arrest. *Cell Syst* **8**, 163-
956 167.e2 (2019).

957 90. D. G. Kirova, *et al.*, A ROS-dependent mechanism promotes CDK2 phosphorylation to drive
958 progression through S phase. *Dev Cell* **57**, 1712 (2022).

959 91. D. P. Byrne, *et al.*, Aurora A regulation by reversible cysteine oxidation reveals evolutionarily
960 conserved redox control of Ser/Thr protein kinase activity. *Sci Signal* **13** (2020).

961 92. S. G. Menon, *et al.*, “Redox Regulation of the G 1 to S Phase Transition in the Mouse Embryo
962 Fibroblast Cell Cycle 1” (2003).

963 93. C. T. J. van Velthoven, T. A. Rando, Stem Cell Quiescence: Dynamism, Restraint, and
964 Cellular Idling. *Cell Stem Cell* **24**, 213–225 (2019).

965 94. S. Horvath, J. Dong, Geometric interpretation of gene coexpression network analysis. *PLoS*
966 *Comput Biol* **4** (2008).

95. S. Morabito, F. Reese, N. Rahimzadeh, E. Miyoshi, V. Swarup, hdWGCNA identifies co-expression networks in high-dimensional transcriptomics data. *Cell Reports Methods* **3** (2023).

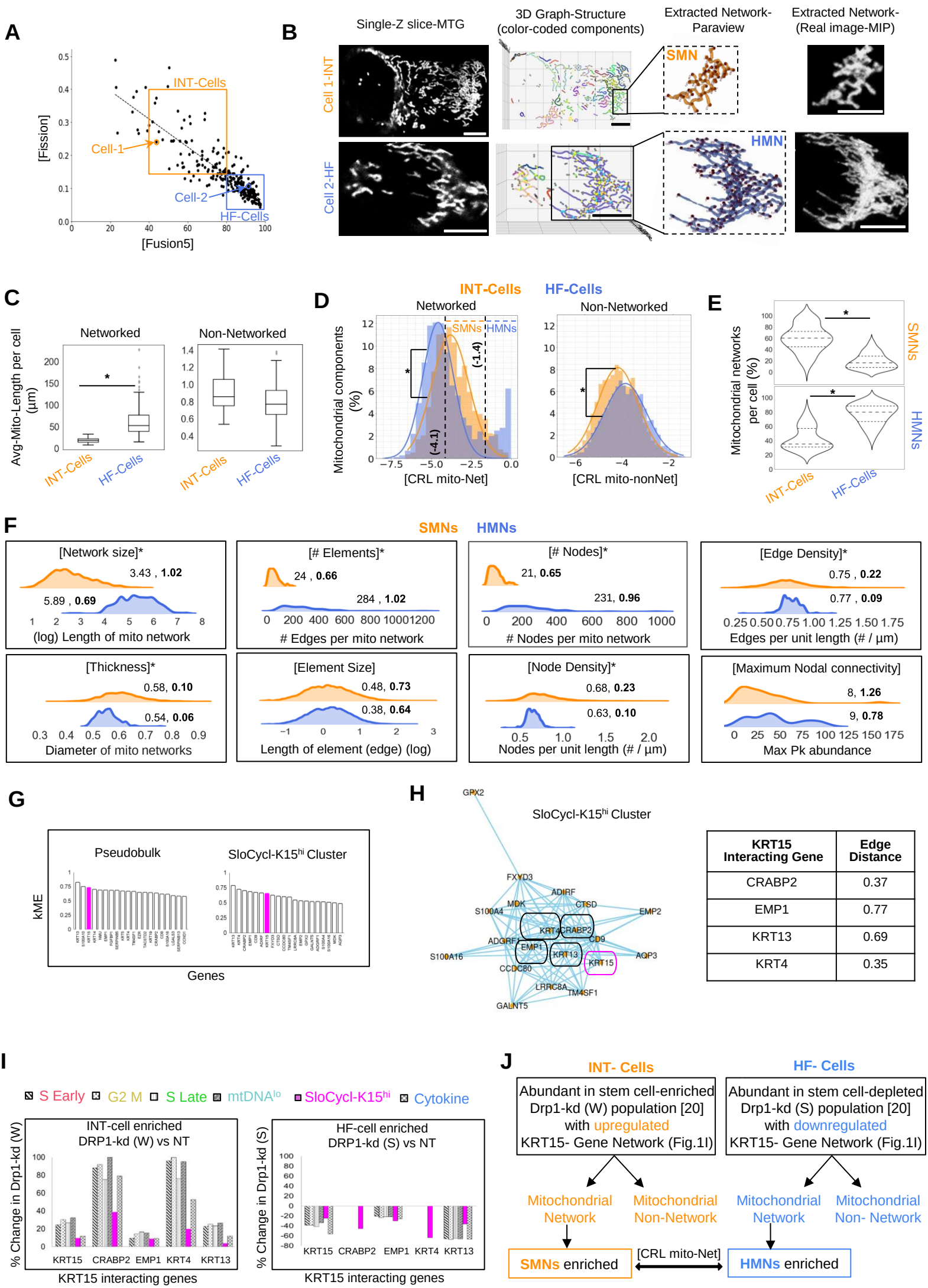
A
INT-Cells
Cell-1
Cell-2
HF-Cells
[Fission]
[Fusion5]
B
Single-Z slice-MTG
3D Graph-Structure (color-coded components)
Extracted Network-Paraview
Extracted Network-(Real image-MIP)
Cell 1-INT
Cell 2-HF
SMN
HMN
C
Avg-Mito-Length per cell (µm)
Networked
Non-Networked
INT-Cells
HF-Cells
D
INT-Cells
HF-Cells
Networked
Non-Networked
SMNs
HMNs
(-1.4)
(-4.1)
Mitochondrial components (%)
[CRL mito-Net]
[CRL mito-nonNet]
E
Mitochondrial networks per cell (%)
SMNs
HMNs
INT-Cells
HF-Cells
F
SMNs
HMNs
[Network size]*
3.43 , 1.02
5.89 , 0.69
(log) Length of mito network
[# Elements]*
24 , 0.66
284 , 1.02
Edges per mito network
[# Nodes]*
21, 0.65
231, 0.96
Nodes per mito network
[Edge Density]*
0.75 , 0.22
0.77 , 0.09
Edges per unit length (# / µm)
[Thickness]*
0.58, 0.10
0.54, 0.06
Diameter of mito networks
[Element Size]
0.48, 0.73
0.38, 0.64
Length of element (edge) (log)
[Node Density]*
0.68, 0.23
0.63, 0.10
Nodes per unit length (# / µm)
[Maximum Nodal connectivity]
8, 1.26
9, 0.78
Max Pk abundance
G
Pseudobulk
SloCycl-K15hi Cluster
kME
Genes
H
SloCycl-K15hi Cluster
GPX2
FXYD3
ADIRF
MDK
CTSD
S100A4
EMP2
KRT4
CRABP2
ADGRF1
CD9
EMP1
KRT13
S100A16
AQP3
KRT15
CCDC80
LRRC8A
TM4SF1
GALNT5
KRT15 Interacting Gene | Edge Distance
CRABP2 | 0.37
EMP1 | 0.77
KRT13 | 0.69
KRT4 | 0.35
I
S Early
G2 M
S Late
mtDNAlo
SloCycl-K15hi
Cytokine
INT-cell enriched DRP1-kd (W) vs NT
HF-cell enriched DRP1-kd (S) vs NT
% Change in Drp1-kd (W)
% Change in Drp1-kd (S)
KRT15
CRABP2
EMP1
KRT4
KRT13
KRT15 interacting genes
J
INT- Cells
HF- Cells
Abundant in stem cell-enriched Drp1-kd (W) population [20] with upregulated KRT15- Gene Network (Fig.1I)
Abundant in stem cell-depleted Drp1-kd (S) population [20] with downregulated KRT15- Gene Network (Fig.1I)
Mitochondrial Network
Mitochondrial Non-Network
Mitochondrial Network
Mitochondrial Non- Network
SMNs enriched
[CRL mito-Net]
HMNs enriched
Fig.1

Figure. 1: Single mitochondrial analyses identify and characterize the physical Small-Mitochondrial-Networks that are linked to stemness transcriptomic networks. A. Scatter plot of [Fission] versus [Fusion5] metrics from mito-SinCe analysis of individual cells stained with Mitotracker Green in a combined population with varying levels of Drp-1 knockdown {re-analysed from (20)}; range for INT-cells and HF-cells are demarcated by coloured boxes. **B.** Representative images of single cells from INT-Cells and HF-Cells populations marked in **A**; Single optical slices and 3D graph from mito-SinComp analysis with networks are shown. The sample SMN and HMN were magnified and visualized using ParaView software from Cell 1-INT and Cell 2-HF, respectively, with corresponding network cut out from the raw image. Scale bar: 5 µm. **C.** Box plot of Avg-Mito-Length per cell of networked and non-networked mitochondria in INT and HF groups. **D.** Histogram distribution of [CRL mito-Net] or [CRL mito-nonNet], with demarcation of thresholds (dashed line) for SMNs (−4.1 to −1.4) and HMNs (≥−1.4) in the network plot (see Methods for details) **E.** Violin plot of mitochondrial networks per cell in the SMN and HMN categories in INT and HF groups, with median (dashed line) and the quartile ranges (dotted lines) shown. **F.** Ridgeline plot comparing the distribution of structural parameters between SMNs and HMNs (see Supplementary methods for the description of the parameters); Median and Coefficient of Variation are indicated for each parameter, latter in bold. **G.** kME plot of KRT15 transcriptomic interaction modules, identified using hdWGCNA, of the Drp1-kd (W) and Drp1-kd (S) datasets compared to NT control {original data published in (20)}. **H.** Hub-Gene Network Plot of the SloCycl-K15^{hi} module identified in **G**, with direct KRT15 transcriptomic connections are outlined (left). The table shows edge distance of KRT15 with its direct connections. **I.** Bar plots showing percentage change in median values for INT group enriched DRP1-kd (W) and HF-cell enriched DRP1-kd (S) with respect to control, NT across colour-coded cell clusters. **J.** Schematic of the summary of mito-SinComp structural analyses **(B-F)** and scRNA-seq analyses **(G-I)** of the combined population with varying levels of Drp-1 knockdown. (* signifies Holmes-Bonferroni corrected p-value < 0.05).

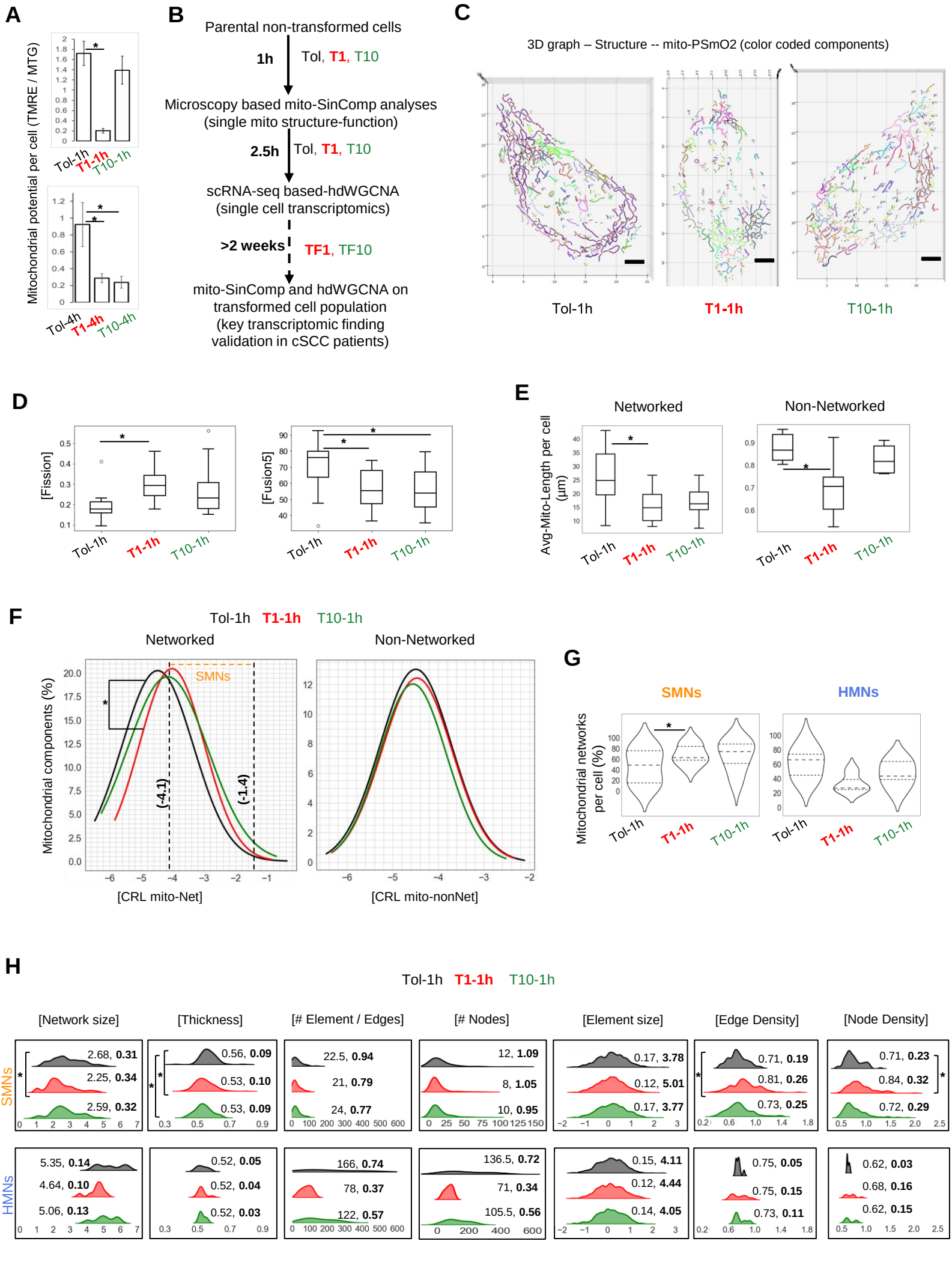
A
Mitochondrial potential per cell (TMRE / MTG)
Tol-1h
T1-1h
T10-1h
Tol-4h
T1-4h
T10-4h
B
Parental non-transformed cells
1h
Tol, T1, T10
Microscopy based mito-SinComp analyses
(single mito structure-function)
2.5h
Tol, T1, T10
scRNA-seq based-hdWGCNA
(single cell transcriptomics)
>2 weeks
TF1, TF10
mito-SinComp and hdWGCNA on
transformed cell population
(key transcriptomic finding
validation in cSCC patients)
C
3D graph – Structure -- mito-PSmO2 (color coded components)
Tol-1h
T1-1h
T10-1h
D
[Fission]
[Fusion5]
Tol-1h
T1-1h
T10-1h
E
Networked
Non-Networked
Avg-Mito-Length per cell (µm)
Tol-1h
T1-1h
T10-1h
F
Tol-1h T1-1h T10-1h
Networked
Non-Networked
SMNs
Mitochondrial components (%)
(-4.1)
(-1.4)
[CRL mito-Net]
[CRL mito-nonNet]
G
SMNs
HMNs
Mitochondrial networks per cell (%)
Tol-1h
T1-1h
T10-1h
H
Tol-1h T1-1h T10-1h
[Network size]
[Thickness]
[# Element / Edges]
[# Nodes]
[Element size]
[Edge Density]
[Node Density]
SMNs
HMNs
2.68, 0.31
2.25, 0.34
2.59, 0.32
0.56, 0.09
0.53, 0.10
0.53, 0.09
22.5, 0.94
21, 0.79
24, 0.77
12, 1.09
8, 1.05
10, 0.95
0.17, 3.78
0.12, 5.01
0.17, 3.77
0.71, 0.19
0.81, 0.26
0.73, 0.25
0.71, 0.23
0.84, 0.32
0.72, 0.29
5.35, 0.14
4.64, 0.10
5.06, 0.13
0.52, 0.05
0.52, 0.04
0.52, 0.03
166, 0.74
78, 0.37
122, 0.57
136.5, 0.72
71, 0.34
105.5, 0.56
0.15, 4.11
0.12, 4.44
0.14, 4.05
0.75, 0.05
0.75, 0.15
0.73, 0.11
0.62, 0.03
0.68, 0.16
0.62, 0.15

Fig. 2

Figure. 2: Acute-1h exposure to stem cell enriching carcinogen depolarizes mitochondria and converts hyperfused mitochondrial networks (HMNs) to more complex small mitochondrial networks (SMNs). A. Mitochondrial potential per cell measured as the ratio of TMRE to MTG signal from individual HaCaT cells from confocal micrographs of Tol, T1-1h, T10-1h (top) and Tol, T1-4h, T10-4h (bottom) groups. **B.** Schematic of the experimental regime using mito-SinComp and scRNA-seq analyses for studying acute impact of TCDD exposure that leads to eventual neoplastic transformation. **C.** Representative 3D graph of single cells from mito-SinComp analysis from Tol-1h, T1-1h and T10-1h groups. Scale bar: 5 µm **D.** Box plot of [Fission] and [Fusion5] metrics of individual cells from mito-SinCe analyses of Tol-1h, T1-1h and T10-1h groups. **E.** Box plot of Avg-Mito-Length per cell of networked and non-networked mitochondria from Tol-1h, T1-1hand T10-1h groups. **F.** Histogram distribution of [CRL mito-Net] or [CRL mito-nonNet] metrics, with demarcation of thresholds (dashed line) for SMNs and HMNs in the network plot (as in **Fig. 1D**). **G.** Violin plot of mitochondrial networks per cell in the SMN and HMN categories in Tol-1h, T1-1h and T10-1h groups, with median (dashed line) and the quartile ranges (dotted lines) shown. **H.** Ridgeline plots comparing the distribution of named structural parameters between SMNs and HMNs from Tol-1h, T1-1h and T10-1h groups; Median and Coefficient of Variation are indicated for each parameter, latter in bold. (* signifies Holmes-Bonferroni corrected p-value < 0.05).

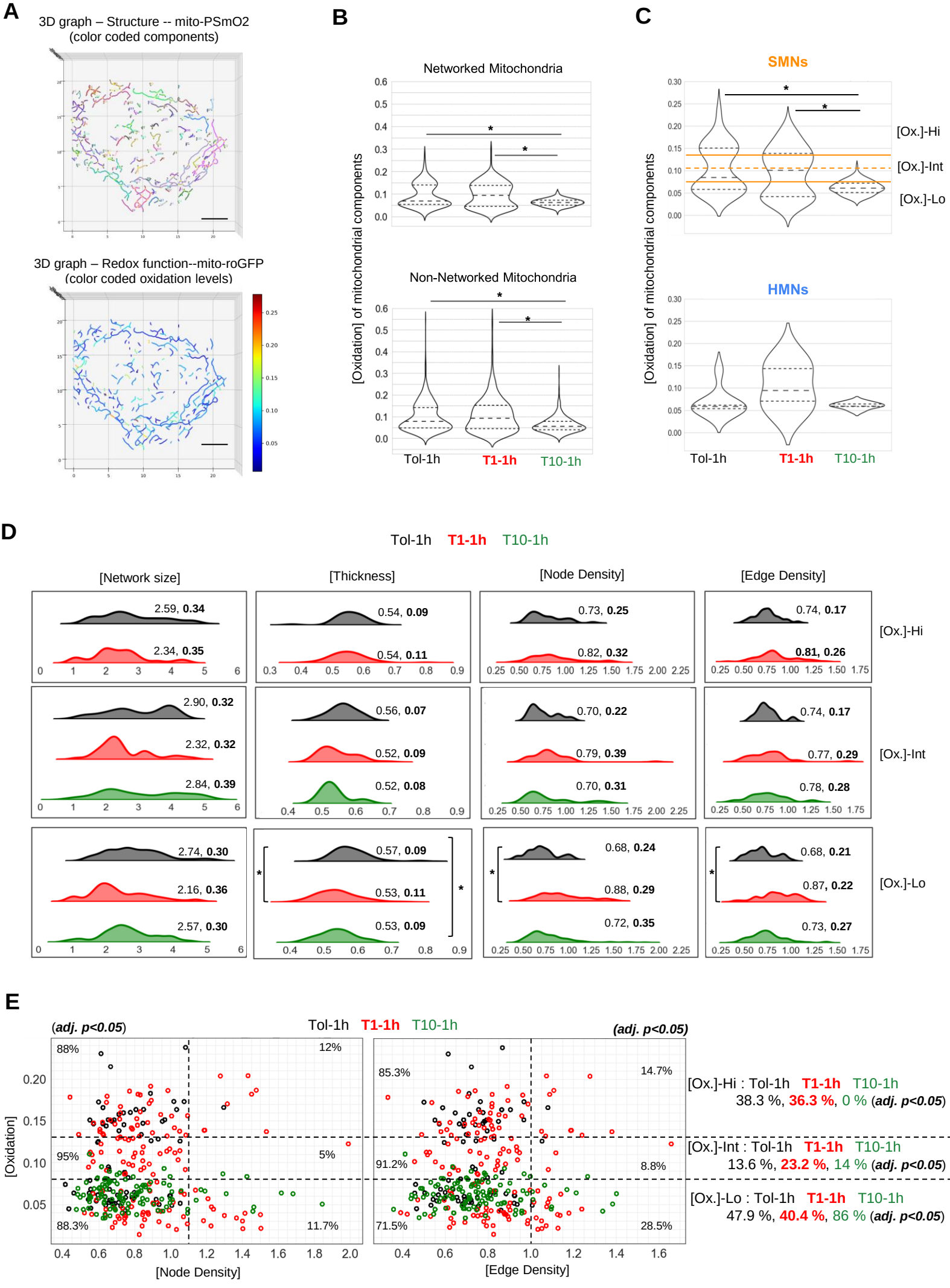
A
3D graph – Structure -- mito-PSmO2
(color coded components)
3D graph – Redox function--mito-roGFP
(color coded oxidation levels)
B
Networked Mitochondria
Non-Networked Mitochondria
[Oxidation] of mitochondrial components
Tol-1h
T1-1h
T10-1h
C
SMNs
HMNs
[Ox.]-Hi
[Ox.]-Int
[Ox.]-Lo
D
Tol-1h T1-1h T10-1h
[Network size]
[Thickness]
[Node Density]
[Edge Density]
2.59, 0.34
2.34, 0.35
0.54, 0.09
0.54, 0.11
0.73, 0.25
0.82, 0.32
0.74, 0.17
0.81, 0.26
2.90, 0.32
2.32, 0.32
2.84, 0.39
0.56, 0.07
0.52, 0.09
0.52, 0.08
0.70, 0.22
0.79, 0.39
0.70, 0.31
0.74, 0.17
0.77, 0.29
0.78, 0.28
2.74, 0.30
2.16, 0.36
2.57, 0.30
0.57, 0.09
0.53, 0.11
0.53, 0.09
0.68, 0.24
0.88, 0.29
0.72, 0.35
0.68, 0.21
0.87, 0.22
0.73, 0.27
E
(adj. p<0.05)
Tol-1h T1-1h T10-1h
(adj. p<0.05)
88%
12%
95%
5%
88.3%
11.7%
85.3%
14.7%
91.2%
8.8%
71.5%
28.5%
[Oxidation]
[Node Density]
[Edge Density]
[Ox.]-Hi : Tol-1h T1-1h T10-1h
38.3 %, 36.3 %, 0 % (adj. p<0.05)
[Ox.]-Int : Tol-1h T1-1h T10-1h
13.6 %, 23.2 %, 14 % (adj. p<0.05)
[Ox.]-Lo : Tol-1h T1-1h T10-1h
47.9 %, 40.4 %, 86 % (adj. p<0.05)

Fig. 3

Figure 3. Acute-1h exposure to stem cell enriching carcinogen sustains an intermediate oxidative status in the SMNs of restricted nodal complexity. A. Representative 3D graphs of single cells from mito-SinComp analyses showing distribution of mitochondrial components (networks and non-networks) colour-coded by structure (top), oxidation levels (bottom) with scale shown. **B.** Violin plot of [Oxidation] of individual mitochondrial components in the networked and non-networked category in Tol-1h, T1-1h and T10-1h groups, with median (dashed line) and the quartile ranges (dotted lines) shown. **C.** Violin plot of [Oxidation] of individual mitochondrial components in SMNs and HMNs category in Tol-1h, T1-1h and T10-1h groups, with median (dashed line) and the quartile ranges (dotted lines) shown; SMNs are divided into three zones based on high, intermediate and low oxidation levels ([Ox.]-Hi, [Ox.]-Int and Ox-Lo) with the criteria described in the appropriate Results section. **D.** Ridgeline plots comparing the distribution of the named structural parameters of SMNs from Tol-1h, T1-1h and T10-1h groups within each of the above three oxidation zones; Median and Coefficient of Variation are indicated for each parameter, latter in bold. **E.** Scatter plot of [Oxidation] vs [Edge/Node density] for individual SMNs in Tol-1h, T1-1h and T10-1h groups. The horizontal and the vertical dashed lines indicate the demarcation of the [Oxidation] and the [Edge/Node Density] zones, respectively. The percentage abundance of SMNs in each zone is mentioned with $p<0.05$, showing Chi-square goodness of fit analysis. (* signifies Holmes-Bonferroni corrected p-value < 0.05).

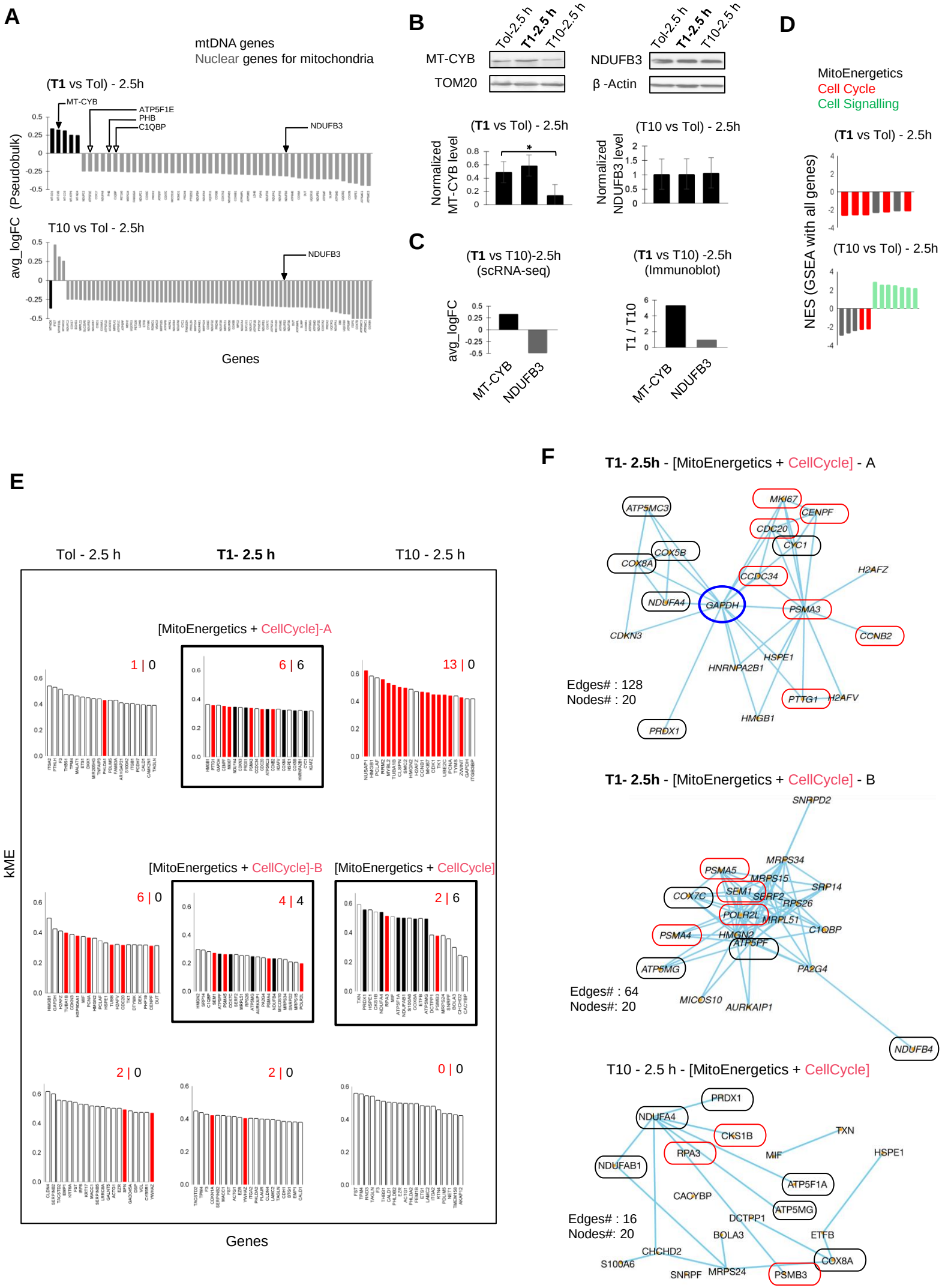
A
mtDNA genes
Nuclear genes for mitochondria
(T1 vs Tol) - 2.5h
MT-CYB
ATP5F1E
PHB
C1QBP
NDUFB3
avg_logFC (Pseudobulk)
T10 vs Tol - 2.5h
NDUFB3
Genes
B
Tol-2.5 h
T1-2.5 h
T10-2.5 h
MT-CYB
TOM20
NDUFB3
β -Actin
(T1 vs Tol) - 2.5h
Normalized MT-CYB level
(T10 vs Tol) - 2.5h
Normalized NDUFB3 level
C
(T1 vs T10)-2.5h (scRNA-seq)
avg_logFC
MT-CYB
NDUFB3
(T1 vs T10) -2.5h (Immunoblot)
T1 / T10
MT-CYB
NDUFB3
D
MitoEnergetics
Cell Cycle
Cell Signalling
(T1 vs Tol) - 2.5h
NES (GSEA with all genes)
(T10 vs Tol) - 2.5h
E
Tol - 2.5 h
T1- 2.5 h
T10 - 2.5 h
[MitoEnergetics + CellCycle]-A
1 | 0
6 | 6
13 | 0
kME
[MitoEnergetics + CellCycle]-B
[MitoEnergetics + CellCycle]
6 | 0
4 | 4
2 | 6
2 | 0
2 | 0
0 | 0
Genes
F
T1- 2.5h - [MitoEnergetics + CellCycle] - A
ATP5MC3
MKI67
CENPF
CDC20
CYC1
COX5B
COX8A
CCDC34
H2AFZ
NDUFA4
GAPDH
PSMA3
CDKN3
CCNB2
HSPE1
HNRNPA2B1
Edges# : 128
Nodes# : 20
PTTG1
H2AFV
HMGB1
PRDX1
T1- 2.5h - [MitoEnergetics + CellCycle] - B
SNRPD2
MRPS34
PSMA5
MRPS15
SRP14
COX7C
SEM1
SRRF2
RPS26
POLR2L
MRPL51
C1QBP
PSMA4
HMGN2
ATP5PF
ATP5MG
PA2G4
Edges# : 64
Nodes#: 20
MICOS10
AURKAIP1
NDUFB4
T10 - 2.5 h - [MitoEnergetics + CellCycle]
PRDX1
NDUFA4
CKS1B
TXN
RPA3
MIF
HSPE1
NDUFAB1
ATP5F1A
CACYBP
ATP5MG
Edges# : 16
Nodes#: 20
DCTPP1
BOLA3
ETFB
CHCHD2
S100A6
COX8A
SNRPF
MRPS24
PSMB3

Fig. 4

Figure 4. Acute-2.5h exposure to stem cell enriching carcinogen upregulates mtDNA genes, while establishing transcriptomic interaction between mitochondrial energetics and cell cycle exit. A. T1-2.5h vs Tol-2.5h and T10-2.5h vs Tol-2.5h pairwise pseudobulk analyses on scRNA-seq data; only expression of genes encoding mitochondrial proteins (MitoCarta) are shown here, with solid triangles indicating MT-CYB and NDUFB3 genes chosen for validation in **B**, while open triangles denote genes uniquely modulated in T1-2.5h **B.** Immunoblot analysis of MT-CYB (left) and NDUFB3 (right), with TOM20 and β-actin as loading controls in Tol-2.5h, T1-2.5h and T10-2.5h groups. Levels of MT-CYB and NDUFB3 were normalized to their respective loading controls (bottom); * signifies p value < 0.05 from Student's t-test. **C.** Pseudobulk analyses from **A** for MT-CYB and NDUFB3 (left) and ratio of relative expression for these molecules in T1 vs T10 from **B** (right). **D.** Normalized Enrichment Scores (NES) from Gene Set Enrichment Analysis (GSEA) of all genes from pseudobulk analyses described in **A**. **E.** kME Plots of all modules identified with hdWGCNA, using all genes from T1-2.5h vs Tol- 2.5h pairwise pseudobulk analysis; [MitoEnergetics + CellCycle] modules are boxed. **F.** Hub-Gene Network plots for the top 20 hub genes of the boxed modules in **E,** with number of edges and nodes indicated, mitochondrial and cell genes are outlined, and GAPDH circled.

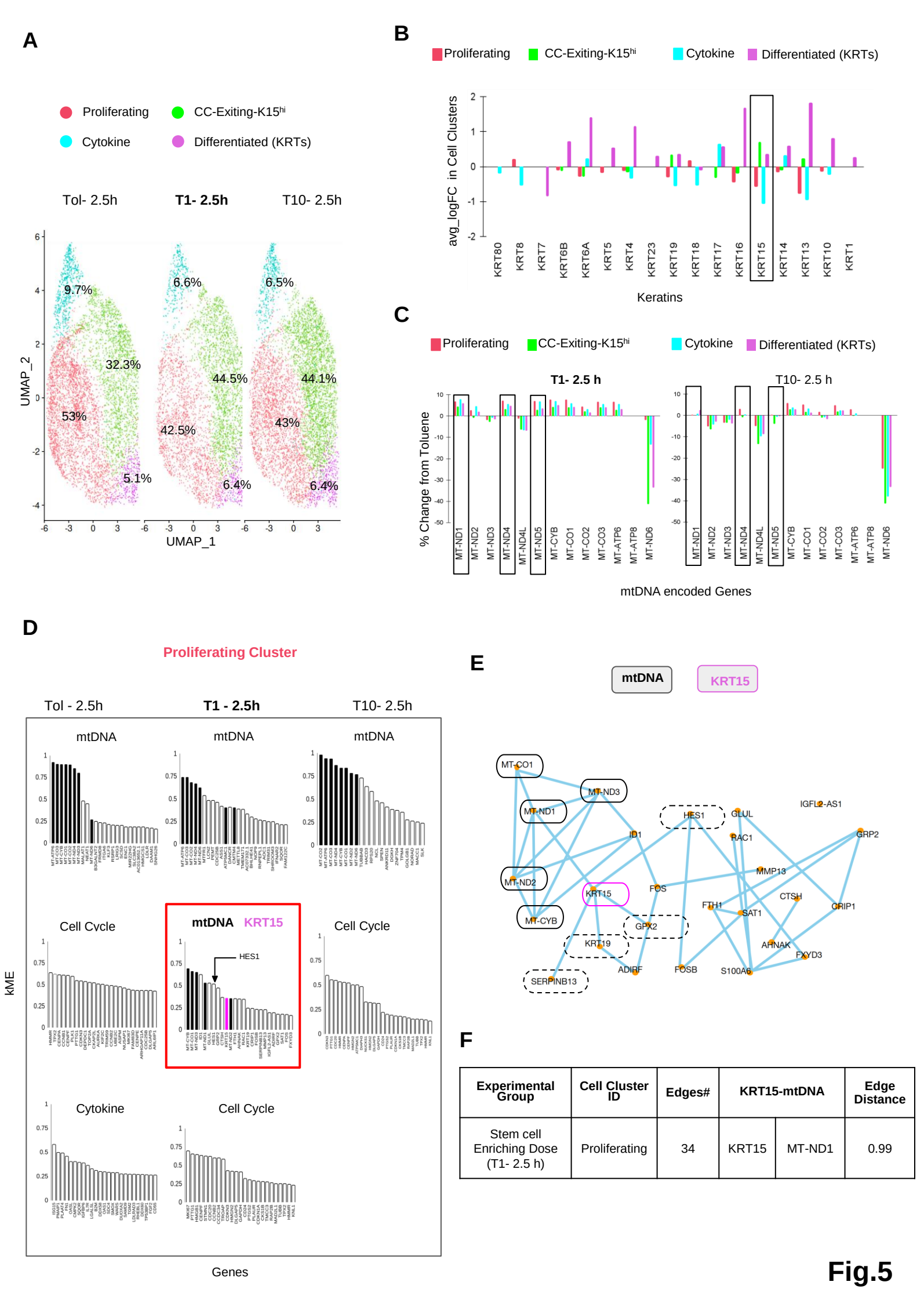

Experimental Group	Cell Cluster ID	Edges#	KRT15-mtDNA		Edge Distance
Stem cell Enriching Dose (T1- 2.5 h)	Proliferating	34	KRT15	MT-ND1	0.99

Fig.5

Figure 5. Acute-2.5h exposure to stem cell enriching carcinogen establishes transcriptomic interaction between mtDNA genes and stemness gene KRT15 in non-transformed proliferating cells prior to their cell cycle exit. A. UMAP plot displaying scRNA-seq derived clusters within cell populations of the Tol-2.5h, T1-2.5h and T10-2.5h groups; the numbers indicate % abundance of cells in each cluster based on **Fig. S6A** and the identity of the clusters are based on top10 marker genes across clusters and GSEA. **B.** Bar plots showing cluster-specific average logFC of all Keratin genes in the named cell clusters, with stem cell-specific KRT15 boxed. (also see **Fig. S6D** for raw data on KRT15). **C.** Bar plots showing percentage change in median expression of mtDNA-encoded genes for T1-2.5h or T10-2.5h groups from Tol-2.5h group across clusters (also see **Fig. S6C** for raw data); MT-ND1 is boxed. **D.** kME plots showing transcriptomic interaction modules obtained using hdWGCNA, which were functionally annotated using GSEA; the modules of Proliferating cluster are shown where interaction between mtDNA genes and KRT15 is detected (boxed). **E.** Hub-Gene Network plot displaying the top 25 genes from the boxed module identified in **D**; Nodes of mtDNA-encoded genes, KRT15 and its directly interacting genes are outlined. **F.** Table displaying edge number and distance for the direct transcriptomic connection between KRT15 and MT-ND1 from **E**.

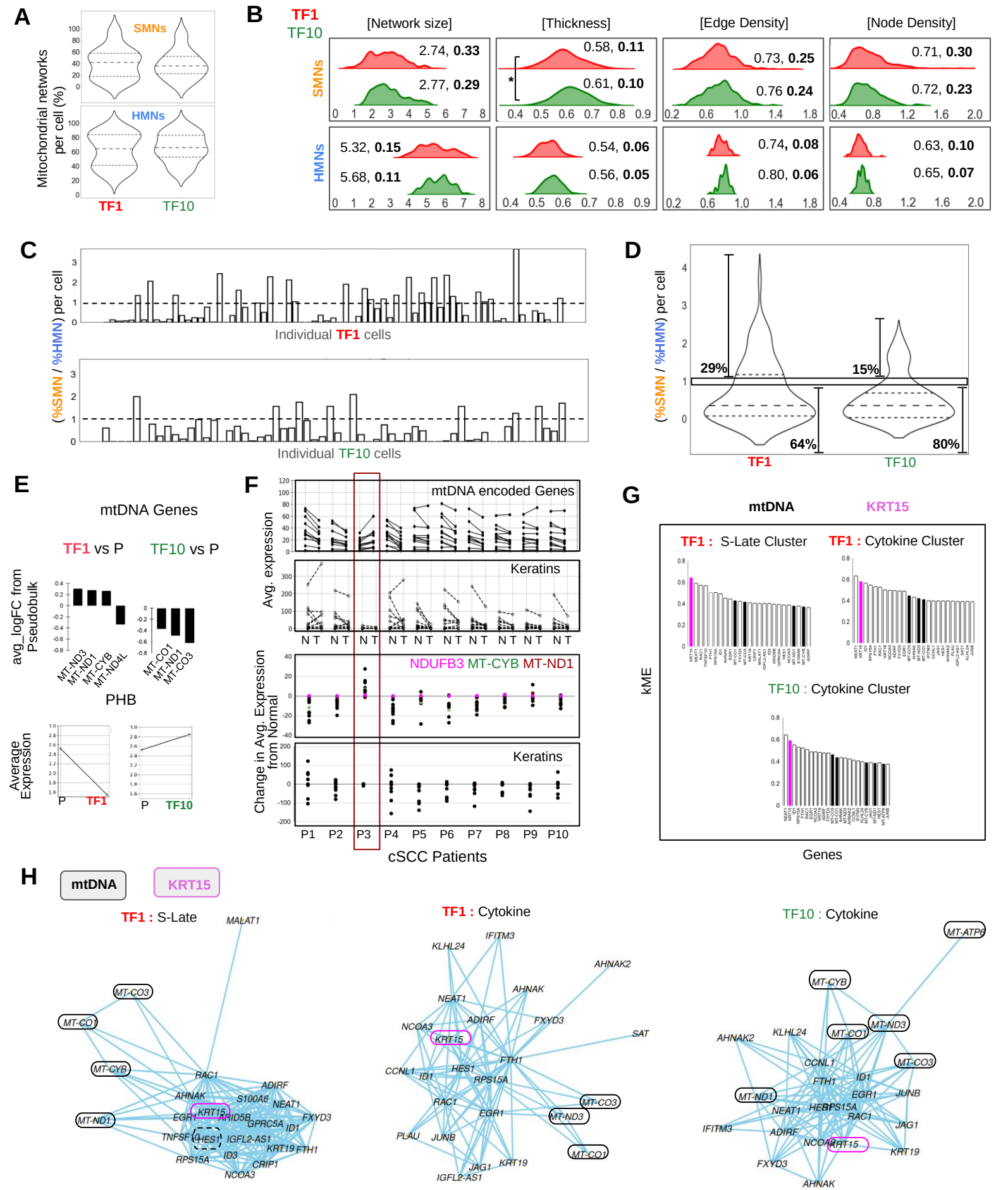

I

Experimental Group	Cell Cluster ID	Edges #	KRT15-direct connections (only relevant ones mentioned)		Edge Distance
TF1 (enriched with SMN and stem cells)	S Late	310	KRT15	MT-CYB	0.99
				MT-ND1	0.99
				HES1	0.44
	Cytokine	159	No mtDNA or HES1 connection		
TF10	Cytokine	210	Only HES1 connection		

Fig. 6

Figure 6. Transformation with stem cell enriching carcinogen sustains SMN enrichment and maintains the mtDNA-KRT15 transcriptomic interaction particularly in late S phase. A. Violin plot of mitochondrial networks per cell in SMN and HMN categories in TF1 and TF10 transformed populations, with median (dashed line) and the quartile ranges (dotted lines) shown. **B.** Ridgeline plots comparing the distribution of the named structural parameters between SMNs and HMNs from TF1 and TF10 groups; Median and Coefficient of Variation are indicated for each parameter, latter in bold. (* signifies Holmes-Bonferroni corrected p-value < 0.05). **C.** Bar chart showing (%SMN / %HMN) per cell among TF1 and TF10 groups. **D.** Violin plot showing (%SMN / %HMN) per cell in TF1 and TF10 groups, with median (dashed line) and the quartile ranges (dotted lines) shown; the percentages of population above 1.1 and below 0.9 are mentioned. **E.** Overall differential gene expression for mtDNA genes using pseudo-bulk RNA-seq analysis (top) and average expression for Prohibitin (PHB) (bottom) for TF1 and TF10 compared to Parental (P) control. **F.** Absolute average expression (top two) and its change in tumor (T) from normal (N) (bottom two) for mtDNA encoded genes and major Keratins for scRNA-seq data of cSCC Patient (P) data (n=10) from Ji. et al., 2020 (67) (N- Normal and T-Tumor). **G.** kME plots of KRT15 transcriptomic interaction modules using hdWGCNA of the TF1 and TF10 datasets compared to P control {original data published in (20)}. **H.** Hub-Gene Network Plot of the TF1: S Late module identified and TF1 / TF10: Cytokine modules identified in **G. I.** Direct transcriptomic connections of KRT15 with mtDNA and HES1 in the cell clusters shown, as outlined in **H**; the table shows edge distance of these direct connections.

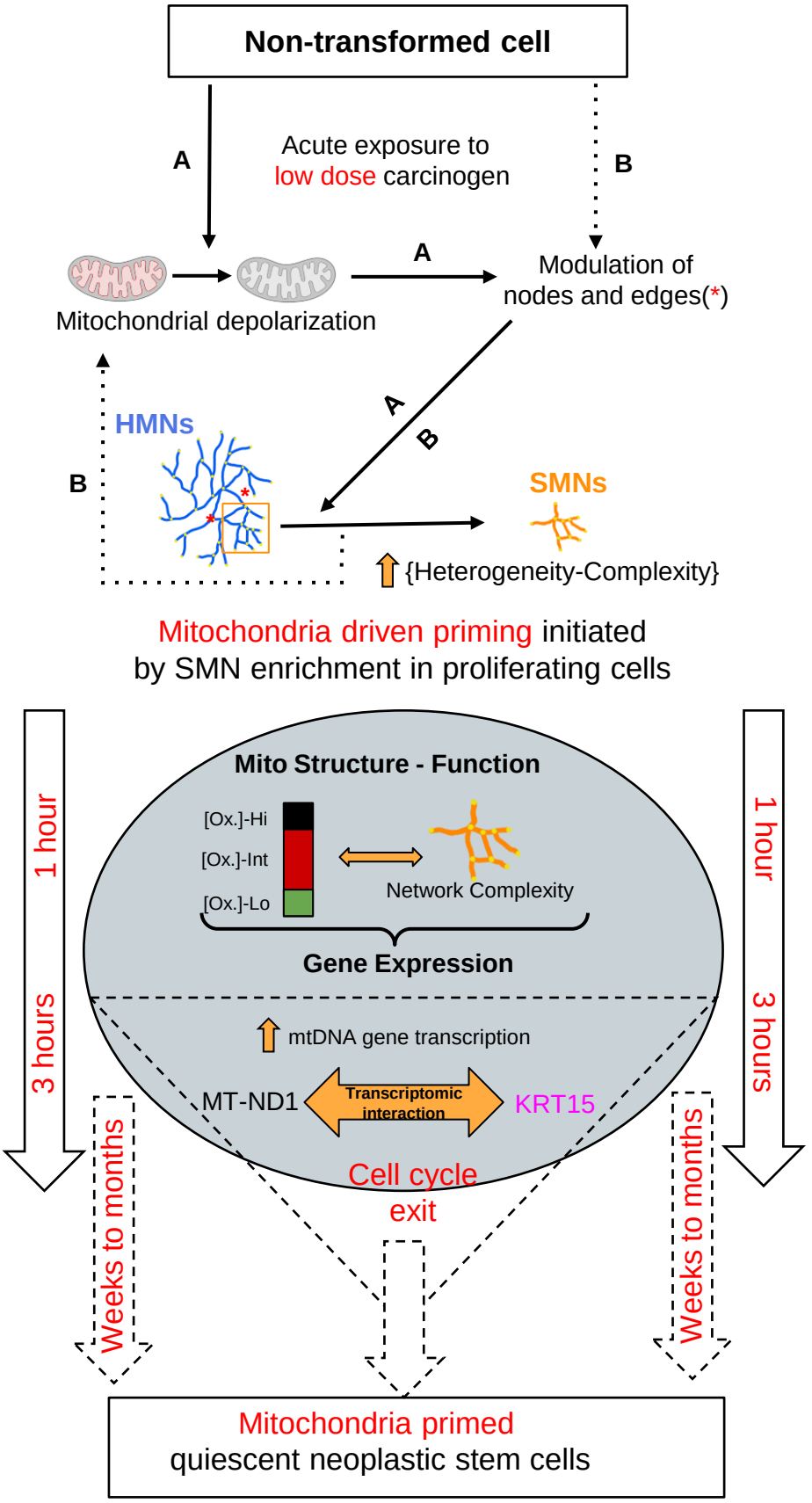
Non-transformed cell
A
Acute exposure to
low dose carcinogen
B
A
Modulation of
nodes and edges(*)
Mitochondrial depolarization
A
B
HMNs
B
SMNs
{Heterogeneity-Complexity}
Mitochondria driven priming initiated
by SMN enrichment in proliferating cells
1 hour
3 hours
Mito Structure - Function
[Ox.]-Hi
[Ox.]-Int
[Ox.]-Lo
Network Complexity
Gene Expression
mtDNA gene transcription
MT-ND1
Transcriptomic interaction
KRT15
Cell cycle
exit
1 hour
3 hours
Weeks to months
Weeks to months
Mitochondria primed
quiescent neoplastic stem cells

Fig. 7

Supporting Information for

Quantitative analyses of structure-function heterogeneity of individual mitochondrial components reveal an early role of small-mitochondrial-networks in priming neoplastic transformation

Mayank Saini[1#], Swati Agarwala[1#], Biratal Wagle[1], Brian Spurlock[2], Bharti Golchha[1], Danitra Parker[2] and Kasturi Mitra[1,2*]

Email: kasturi.mitra@ashoka.edu.in

This PDF file includes:

Supporting text
Figures S1 - S15 with their legends
SI References

Other supporting materials for this manuscript include the following:

Data S1 - S3

Supplementary Methods

Development of mito-SinComp analysis:

The mito-SinComp analysis uses 3D confocal micrographs with appropriate combinations of compatible probes reporting mitochondrial structure and function separately. The images are required to be amenable for MitoGraph analyses as described before (1, 2). Mito-SinComp analysis requires a Linux or MacOS system to run natively. It can be run on Windows through the Windows Subsystem for Linux (WSL) or another Virtual Machine application like VirtualBox. We developed mito-SinComp analysis using Ubuntu 24.04 LTS with VTK 9.0 modifying the open source code for MitoGraph (https://github.com/vianamp/MitoGraph) and after installing all essential libraries and packages (build-essential, cmake, git, r-base, wget, os, sys, libvtk9-dev, libgl1-mesa-dev, freeglut3-dev, qtbase5-dev, qtdeclarative5-dev, libqt5opengl5-dev, pandas, networkx, igraph, PIL, numpy, tifffile, matplotlib.pyplot). Our customized modular script for mito-SinComp structure-function analyses includes the following steps (**Fig. S9**):

1. Identifying the 'structure' and 'function' channels: Our 3D confocal micrographs for mitochondrial structure (shape) -- function (redox) analyses have 3 channels, excited by 405 nm (function-1), 488 nm (function-2) and 555 nm lasers (structure). MitoGraph exclusively uses only designated structure channel to obtain the binary image through an adaptive thresholding process (3). Therefore, we aimed to obtain the intensity values of the 'function' channels in the pixels of the MitoGraph binary image. Here, we used "splitter.py" function to separate the channels using the AICSImageIO and tifffile libraries. Each channel is then saved as an individual Z-stack in TIFF format as 'structure' and 'function' channels.

2. Running MitoGraph: The open source MitoGraph (v3.0) script is included to obtain the MitoGraph output files as described before (1, 2).

3. Identifying individual mitochondrial components: Mitograph produces the following three outputs containing distinct types of information: a) connected Components ("cc") on interconnected elements; b) mitochondrial elements ("line id") on individual mitochondrial segments; c) points on the mitochondrial skeleton ("point id") on individual data points. Each "point id" belongs to a "line id", and each "line id" belongs to a cc. This information is distributed across the following output files: a) *mitograph.txt* contains information about "point id", "line id", and the length of each "line id"; b) *mitograph.cc* file links "node id" to the "cc" they belong to, c) *mitograph.coo* file provides geometric positions (x, y, z coordinates) for each "node id". To streamline our analysis, we consolidated this data into a single, tidy data frame. To incorporate "cc" information into the *mitograph.txt* file for network-level analysis, we identified which "point id" entries are also "node id" entries, where nodes are the terminating points of a "line id". Towards this, we first computed the Euclidean distance between each pair of "point id" (from *mitograph.txt*) and "node id" (from *mitograph.coo*). Thereafter, we identified the "point id" - "node id" pair with the smallest distance to identify the "point id" that corresponds to each "node id". Once the "nodes" were identified, we used the *mitograph.cc* file to link the cc information to each "node id". This enables us to append "cc" information to the *mitograph.txt* file. Thus, the resulting final data frame integrates "cc", "line id", "point id", x, y, z coordinates and "nodes" in a single *.csv file where the structural and functional properties will be included after having calculated as described below. Thus, a comprehensive data file is created for further downstream analyses.

4. Calculating structural properties for networks and non-networks: We first identified the individual networks and non-networks from the connected components ("cc"), which include both networked and non-networked components. Here, we employed a filtering approach based on the number of edges and nodes. Specifically, any connected component with one edge and two nodes, along with their corresponding data, was classified as a non-networked component. All remaining connected components, along with their corresponding data, were categorized as networked components. This classification enabled the separate analysis of networked and non-networked components, facilitating a more focused examination of their distinct properties. The following table includes the definition and formulae of all the structural parameters studied.

Name of metric	**Definition**	**Formulae**
Length of an individual element in μm -Networks	Length of an individual mitochondrial element within a network	$L\text{-}E_{Net}$
Length of an individual element/edge in μm - Networks (log) [Element Size]	Natural log transformed values of length of an individual mitochondrial element within a network	$\ln(L\text{-}E_{Net})$
Length of an individual mitochondrial component in μm - Network	The total length of individual mitochondrial elements that constitute a networked mitochondrial component.	$L_{Net} = \Sigma L\text{-}E_{Net}$
Length of an individual mitochondrial component in μm - Non-Network	Length of individual mitochondrial elements that constitute a non-networked mitochondrial component.	$L_{nNet} = L\text{-}E_{nNet}$
Length of individual mitochondrial component in μm - Network (log) [Network Size]	The total length of individual mitochondrial elements that constitute a networked mitochondrial component.	$\ln(L_{Net})$
Length of individual mitochondrial component in μm - Non-Network (log) [Non-Network Size]	Length of individual mitochondrial elements that constitute a non-networked mitochondrial component.	$\ln(L_{nNet})$
Number of elements per networked mitochondrial component [# Element / Edges]	Total number of mitochondrial elements/edges that constitute a networked mitochondrial component	$\#E_{Net}$

Name of metric	Definition	Formulae
Total number of mitochondrial components per cell [# Components]	Total number of mitochondrial components that are present in a cell which includes networked and non-networked components	#Comp=#Net+#nNet
Total number of mitochondrial components per cell-Networks [# Networks]	Total number of networked mitochondrial components that are present in a cell.	#Net
Total number of mitochondrial components per cell-Non Networks [# Non-Networks]	Total number of non-networked mitochondrial components that are present in a cell.	#nNet
Total length of mitochondrial components per cell in µm [Sum L_{comp}]	Total length of mitochondrial components that are present in a cell which includes networked and non-networked components	Sum $L_{comp}=\Sigma(L_{Net}+L_{nNet})$
Total length of mitochondrial components per cell in µm -Networks [Sum L_{Net}]	Total length of networked mitochondrial components that are present in a cell.	Sum $L_{Net}=\Sigma L_{Net}$
Total length of mitochondrial components per cell in µm -Non Networks [Sum L_{nNet}]	Total length of non-networked mitochondrial components that are present in a cell.	Sum $L_{nNet}=\Sigma L_{nNet}$
Abundance of mitochondrial components per cell (%)-Networks	It is the percentage of networked mitochondrial components that are present in a cell	(#Net/#Comp) *100
Abundance of mitochondrial components per cell (%)-Non Networks	It is the percentage of non-networked mitochondrial components that are present in a cell	(#nNet/#Comp) *100
Average length of	Total length of all networked mitochondrial	(Sum L_{Net}) / (#Net)

Name of metric	Definition	Formulae
mitochondrial component per cell in μm - Networks	components divided by the number of networked components within a cell	
Average length of mitochondrial component per cell in μm - Non-Networks	Total length of all non-networked mitochondrial components divided by number of non-networked components within a cell	(Sum L_{nNet}) / (#nNet)
Relative length of an individual mitochondrial component within a cell-Networks [CRL mito-Net]	Natural log of the length of a networked mitochondrial component divided by the total length of all the networked components of the cell that the former component is a part of	ln{(L_{Net}) / (Sum L_{Net})}
Relative length of an individual mitochondrial components within a cell-Non networks [CRL mito-nonNet]	Natural log of the length of a non-networked mitochondrial component divided by the total length of all the non-networked components of the cell that the former component is a part of	ln{(L_{nNet}) / (Sum L_{nNet})}
Diameter in μm per networked mitochondrial component [Thickness];	As previously published (1)	-
[Fission]; [Fusion5]	As previously published (1)	-
Pk of nodes	No. of edges / element arising from a single node. (4, 5)	-
Number of nodes per networked mitochondrial component [# Nodes]	Number of nodes that are present in a networked mitochondrial component excluding free ends.	# Nodes
Number of nodes per length of a networked component [Node Density]	Number of nodes (excluding free ends) divided by the length of the networked component that they belong to	#Nodes/L_{Net}
Number of edges / elements per length of a networked component [Edge Density]	Number of edges / elements divided by the length of the networked component that they belong to	#Elements (#Edges)/L_{Net}
Max Pk of a node times their count per network	It is product of maximum Pk of a node with their count within a networked mitochondrial component	Max Pk * Count

Name of metric	Definition	Formulae
[Maximum Nodal Connectivity]		
Abundance of SMNs per cell (%)	Number of SMNs divided by total number of networked mitochondrial component within a cell	(#SMNs/#Net) *100
Abundance of HMNs per cell (%)	Number of HMNs divided by total number of networked mitochondrial component within a cell	(#HMNs/#Net) *100
Abundance of mitochondrial components-Networks (%) for [CRL mito-Net]	Percentage of networked components in a certain bin range of their length distribution	(#Net in a bin/ #Net in that population) *100
Abundance of mitochondrial components- Non-Networks (%) for [CRL mito-nonNet]	Percentage of non-networked components in a certain bin range of their length distribution	(#nNet in a bin/ #nNnet in that population) *100

5. Calculating function for networks and non-networks: The redox function was calculated by obtaining the average pixel intensity ratio of individual cc by mapping the 'function' information to the 'structure' information obtained as above. This was achieved following the steps below:

a. Converting MitoGraph output to pixel coordinates: MitoGraph was run using Z-stack for the structure channel using *runMitograph.py* function in a batch processing mode for all cells within a single directory. Mitograph outputs the geometric coordinates (x, y, z) of the mitochondrial skeleton as per the provided scale when running Mitograph. The pixel coordinates (x_pixel, y_pixel, z_pixel) can be retrieved from the geometric coordinates through using the scale using the formula, Where *D* represents either x, y or z. This is then rounded to the nearest integer, as pixel coordinates are a discrete quantity.

$$D_{pixel} = \frac{D}{D_{scale}}$$

The table below shows an example of the results of this process, where the scale for *x* and *y* is 0.104 and is 0.5 for z.

line_id	point_id	x	y	z	x_pixel	y_pixel	z_pixel
0	0	8.97867	4.85333	2.33333	86	47	5
0	1	8.85002	4.95192	2.41975	85	48	5
0	2	8.73600	4.99200	2.50000	84	48	5
1	0	17.42000	6.05800	2.37500	168	58	5
1	1	17.27913	5.89616	2.43519	166	57	5

The conversion is confirmed by the overall overlap of the calculated pixel coordinates (in red) with the MIP of the structural channel, as exemplified in the image below.

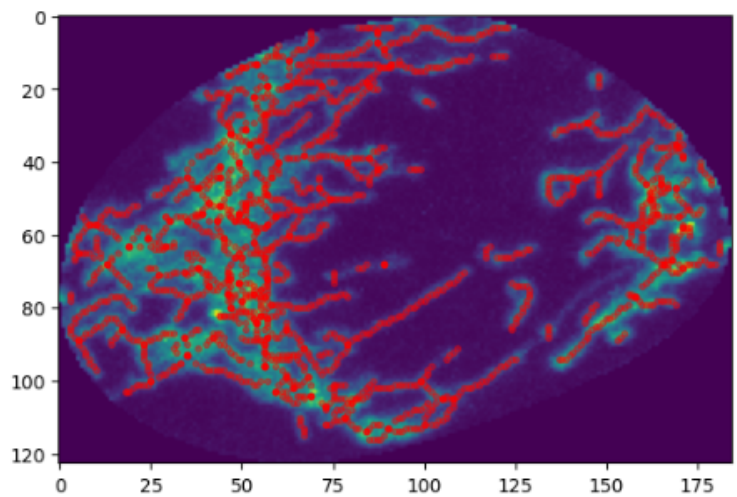

b.<u>Obtaining the intensity values of the pixel coordinates from individual 'function' channels:</u> The Z-stacks Tiff images are converted into a three dimensional array using tifffile library. The intensity value of each pixel coordinate generated in step 5 is calculated from the individual functional channels. The average intensity of the 9 pixels in a 1X3X3 voxel is calculated and assigned to the central pixel. This is repeated for every x, y, z pixel calculated in step 5. In the following example, in the slice of an image at z = 2, , intensity of a_{222} is the average of all the colored pixels.

$$z = 2, \begin{pmatrix} b_{11} & b_{12} & b_{13} & b_{14} & b_{15} \\ b_{21} & a_{211} & a_{212} & a_{213} & b_{25} \\ b_{31} & a_{221} & a_{222} & a_{223} & b_{35} \\ b_{41} & a_{231} & a_{232} & a_{233} & b_{45} \\ b_{51} & b_{52} & b_{53} & b_{54} & b_{55} \end{pmatrix}$$

$$Pixel\ intensity\ of\ a_{222} = \frac{a_{211} + a_{212} + a_{213} + a_{221} + a_{222} + a_{223} + a_{231} + a_{232} + a_{333}}{9}$$

c. <u>Obtaining pixel intensity ratio to reflect redox function</u>**:** Once the pixel_intensity for each pixel is obtained (step 6), this information is put into the "pixel_intensity_channel_*N*" column, where "*N*" reflects which, channel was selected. For calculating the pixel intensity ratio at the individual cc level, the intensities for each channel are grouped according to their "cc_id" and averaged to find the pixel intensity of the "cc". These values are validated as described in the main text. The ratio of these averages gives the "cc_pixel_intensity_ratio", as exemplified below for an individual "cc".

x_pixel	y_pixel	z_pixel	pixel_intensity_channel_1	pixel_intensity_channel_2
105	55	17	256.5	12.75
106	54	17	243.5	35
107	54	18	374	18
108	54	18	483.5	34.25
109	55	18	463.5	17
110	56	18	342.75	0

cc_pixel_intensity_ratio
0.05407279
0.05407279
0.05407279
0.05407279
0.05407279
0.05407279

$$cc\ pixel\ intensity\ channel\ 1 = \frac{256.5 + 243.5 + 374 + 483.5 + 463.5 + 342.75}{6}$$

$$cc\ pixel\ intensity\ channel\ 2 = \frac{12.75 + 35 + 18 + 34.25 + 17 + 0}{6}$$

$$cc\_pixel\_intensity\_ratio = \frac{19.5}{360.625} = 0.05407$$

d. Visualizing single networks and non-networks within single cells in 3D graphs: Visualization of the data from the comprehensive data file is performed using the *3D_generate_graphs.py* script. The data is plotted by looping through each "**cc**" and each "**line id**". The individual points in each "**line id**" are then plotted to ensure that the order of the points is preserved in the visualization. To distinguish between shapes, each "**cc**" is assigned a random and unique color. These shapes are then rendered in a 3D space. The same process is repeated for generating the LUT of the 'function'values, where the color code represents redox function of individual element.

High Dimensional weighted gene correlation network analyses (hdWGCNA) :

hdWGCNA (6), smorabit.github.io/hdWGCNA/) was used to identify gene interaction modules amongst differentially expressed genes (> 0.25 avg_logFC, $<10^{-5}$ p_val_adj, pct ≥ 0.25 in pseudobulk analyses using FindMarkers function) and amongst the characteristic marker genes for the identified cell clusters (> 0.25 avg_logFC, $<10^{-5}$ p_val_adj). QC plots of nCounts_RNA distributions were used to establish lower thresholds for outlier removal (**Figs. S11A-B, S12A, S13A, S14A, S15A**). This processed integrated Seurat object is used as an input for respective hdWGCNA, both at the pseudobulk and cell cluster levels.

The hdWGCNA object was initialized, and metacells were constructed using K-nearest neighbors (KNN) (**Figs. S11C-D, S12B-C, S13B-C, S14B-C, S15B-C**). Gene expression matrices were constructed, and pairwise Pearson's correlations were computed, transformed into adjacency matrices using a soft-thresholding power approach (**Figs. S11E, S12D, S13D, S14D, S15D**), and used to construct networks using Topological Overlap Measures (TOM) values The hdWGCNA algorithm ensured a scale-free topology during signed network construction for each hdWGCNA object for both pseudobulk and cell cluster. Transcriptomic modules were detected using hierarchical clustering and TOM, with module eigengenes (MEs) computed for further analysis. Module connectivity (kME) values were calculated to identify hub genes characterized by high kME values. Selection of specific parameter cut-offs for hdWGCNA are elaborated below:

a. K-nearest neighbors (KNN)-based dimensionality reduction: Metacells for each experimental/control group (pseudobulk) and specific clusters were constructed using KNN, leveraging biological similarity to define cellular subpopulations in each hdWGCNA object. Pearson correlation-based density plots guided the selection of K value of 20 with a maximum of 10 shared neighbors for an average of 5000 cells in each population, optimizing the balance between capturing local structure and minimizing noise in sparse data (**Figs. S11C-D, S12B-C, S13B-C, S14B-C, S15B-C**).

b. Soft Thresholding Power (β): The optimal β value was selected by evaluating the scale-free topology fit index, to enhance strong correlations and reduce weaker ones, aiming for the lowest power where the network closely approximated a scale-free structure. The β values between 6 and 10 were determined as optimal, balancing network sparsity with scale-free topology at both pseudobulk and cell cluster based hdWGCNA objects (solid black circles on plots in (**Figs. S11E, S12D, S13D, S14D, S15D**). This transformation enabled robust, biologically meaningful signed networks across cellular subpopulations

c. Module Connectivity (kME): kME measures the correlation between a gene's expression profile and its module eigengene, indicating the gene's alignment with the module's expression pattern. High kME values suggest that a gene has a central role within the module, while low values indicate a less integral role. Genes in each module were ranked by kME, identifying the top 20 in pseudobulk (**Fig. 1G, 4E**) and top 25 (**Fig. 5D**) in cell cluster-based hdWGCNA for functional significance. This kME analysis highlighted closely interacting clusters, enabling us to identify top ranking hub genes within a network. with high connectivity of KRT15, its interactors, and mtDNA genes within the biological network of connectivity and interaction strength within the biological network (**Fig. 5E**).

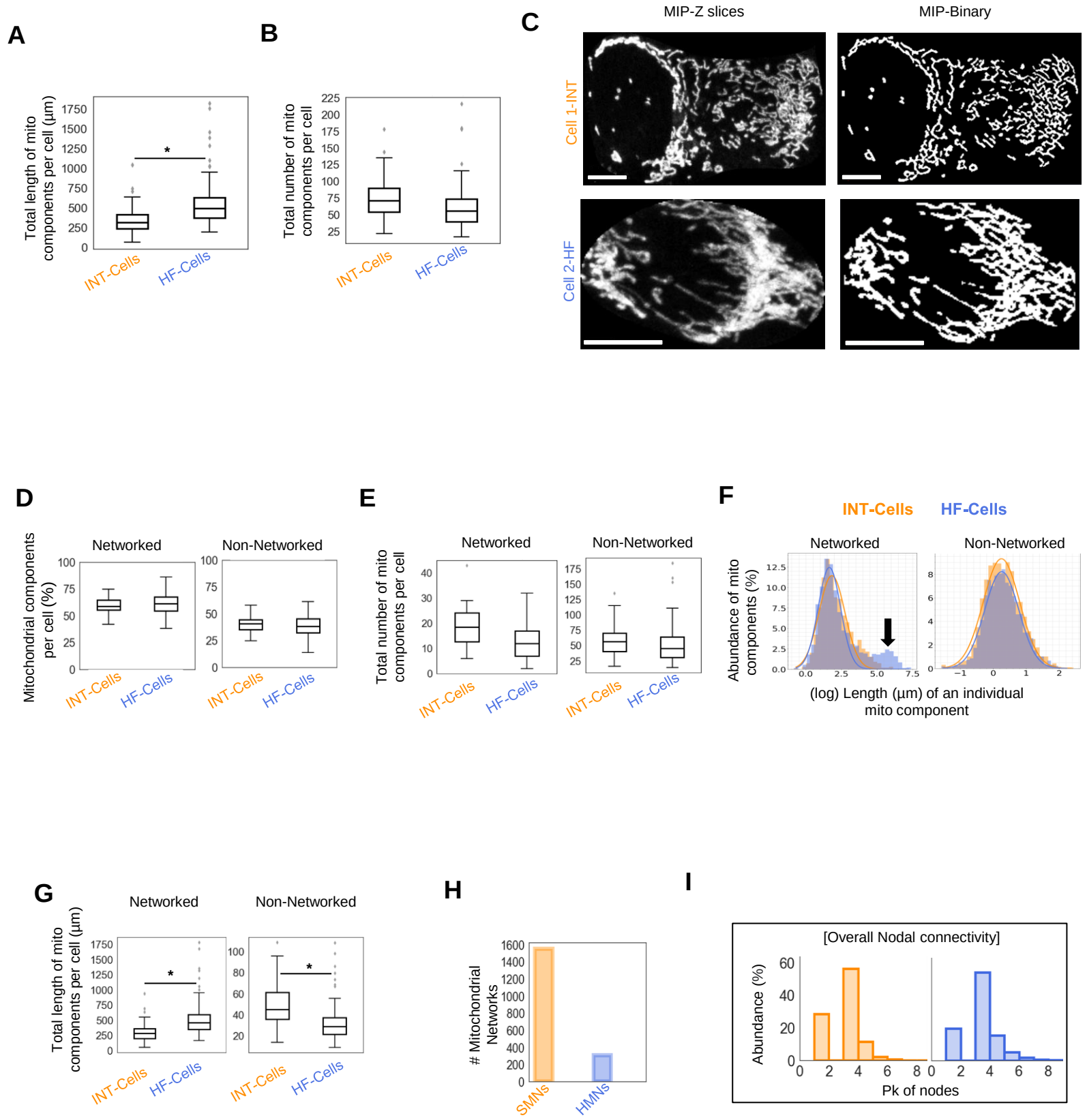
A
Total length of mito components per cell (µm)
1750
1500
1250
1000
750
500
250
0
*
INT-Cells
HF-Cells
B
Total number of mito components per cell
225
200
175
150
125
100
75
50
25
INT-Cells
HF-Cells
C
MIP-Z slices
MIP-Binary
Cell 1-INT
Cell 2-HF
D
Mitochondrial components per cell (%)
Networked
Non-Networked
100
75
50
25
0
INT-Cells
HF-Cells
E
Total number of mito components per cell
Networked
Non-Networked
40
30
20
10
0
175
150
125
100
75
50
25
INT-Cells
HF-Cells
F
INT-Cells
HF-Cells
Networked
Non-Networked
Abundance of mito components (%)
12.5
10.0
7.5
5.0
2.5
0.0
0.0
2.5
5.0
7.5
8
6
4
2
0
−1
0
1
2
(log) Length (µm) of an individual mito component
G
Total length of mito components per cell (µm)
Networked
Non-Networked
1750
1500
1250
1000
750
500
250
0
*
100
80
60
40
20
*
INT-Cells
HF-Cells
H
Mitochondrial Networks
1600
1400
1200
1000
800
600
400
200
0
SMNs
HMNs
I
[Overall Nodal connectivity]
Abundance (%)
60
40
20
0
0
2
4
6
8
0
2
4
6
8
Pk of nodes

Fig. S1

Figure S1. Development of mitoSinComp structural analyses. A. Box plot of the total length of mitochondrial components (including networks and non-networks) per cell in INT and HF groups. **B.** Box plot of the total number of mitochondrial components (including networks and non-networks) per cell in INT and HF groups. **C.** Representative maximum intensity projection (MIP) of original Z slices and Binary from mitoGraph code used in mito-SinComp analysis described in **Fig-1B**; Scale bar: 5 µm. **D.** Box plot of mitochondrial components per cell in networked and non-networked categories in INT-cells and HF-cells groups. **E.** Box plot of the total number of mitochondrial components per cell in networked and non-networked categories in INT-cells and HF-cells groups. **F.** Histogram distribution of log-transformed lengths of individual mitochondrial components in networked and non-networked categories (ignoring their cell identity) in INT-cells and HF-cells groups. **G.** Box plot of the total length of mitochondrial components per cell in networked and non-networked categories in INT-cell and HF-cell groups. **H.** Bar chart showing the number of mitochondrial networks in SMNs and HMNs categories in INT-cell and HF-cell groups. **I.** Histogram plots representing overall nodal connectivity (* signifies Holmes-Bonferroni corrected p-value < 0.05).

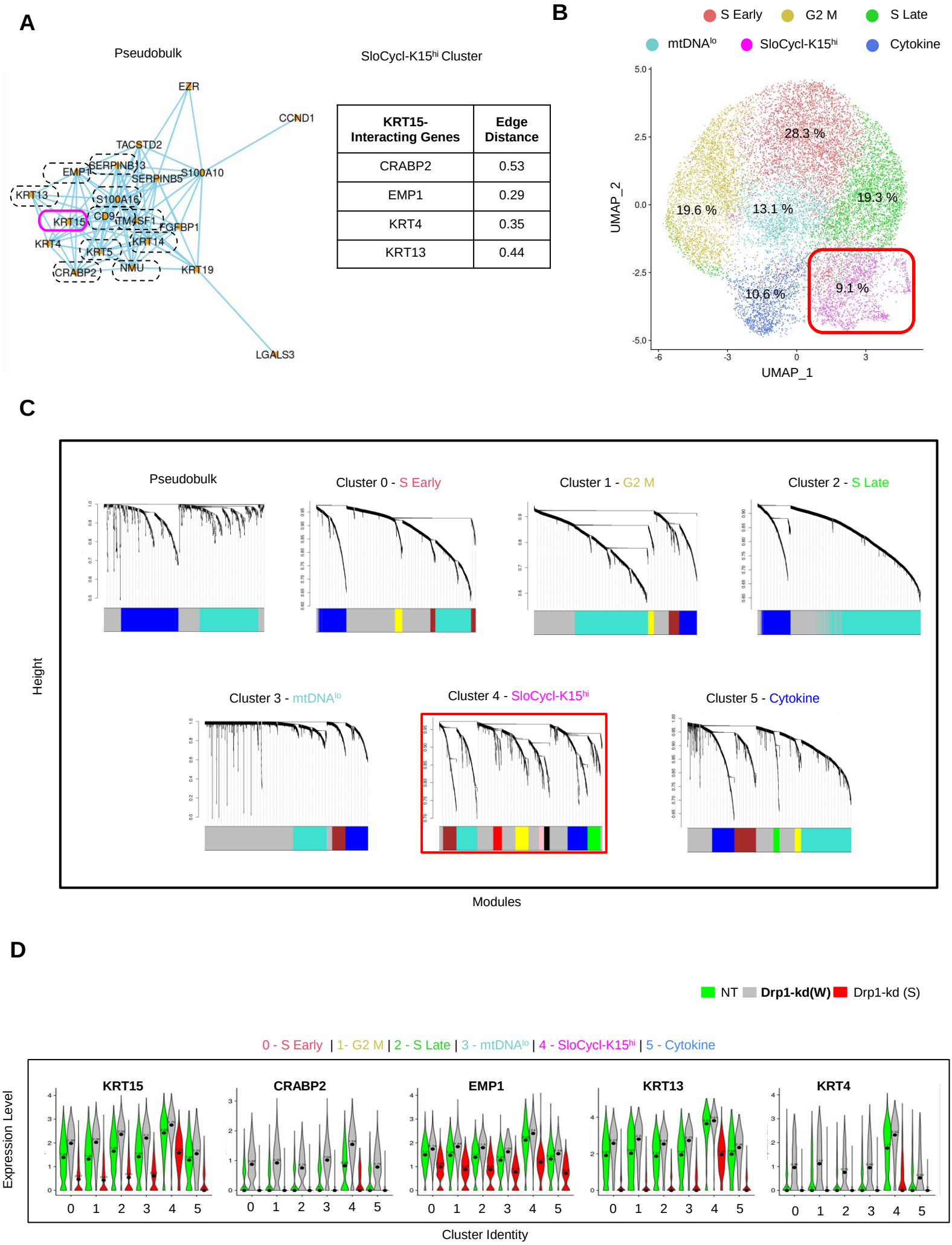

KRT15-Interacting Genes	Edge Distance
CRABP2	0.53
EMP1	0.29
KRT4	0.35
KRT13	0.44

Fig. S2

Figure S2. Employment of hdWGCNA to identify stemness transcriptomic network. A. Hub-Gene Network plot for the module from the pseudobulk analyses identifying the KRT15 module in the left panel of **Fig.1G**. Direct KRT15 transcriptomic connections are outlined with dashed lines, with KRT15 outlined in purple (left). The table depicts the edge distance of the direct transcriptomic connections of KRT15 in the module identified in the SloCycl-K15^{hi} cluster in right panel of **Fig. 1G**. **B.** UMAP plot depicting the color-coded scRNA-seq derived clusters (0-5) with the pooled data of DRP1-kd (W), DRP1-kd (S) and NT (control) populations, with the SloCycl-K15^{hi} cluster outlined; numbers denote percentages of cells within each cluster derived from the pie chart for the clusters (not shown). **C.** Dendrograms depicting hierarchical clustering of adjacency-based dissimilarity to identify color-coded co-expression modules, where grey module represents genes with no significant co-expression; dendrograms from both pseudobulk and cell cluster based analyses shown. **D.** Violin plots depicting gene expression of KRT15 and its direct transcriptomic connections across scRNA-seq derived clusters in the DRP1-kd (W), DRP1-kd (S) and NT (control) populations.

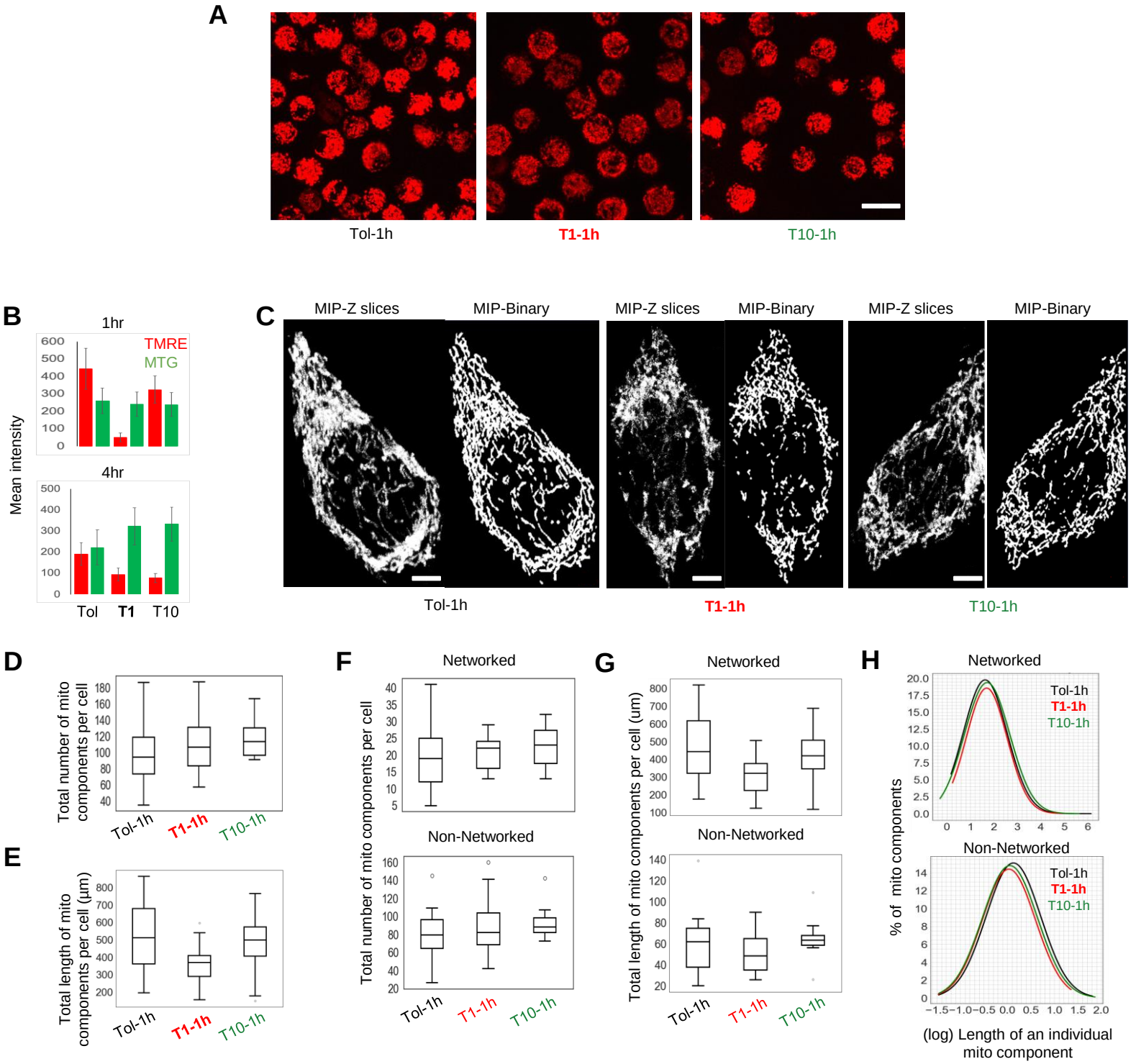
A
Tol-1h
T1-1h
T10-1h
B
1hr
TMRE
MTG
4hr
Mean intensity
Tol
T1
T10
C
MIP-Z slices
MIP-Binary
Tol-1h
T1-1h
T10-1h
D
Total number of mito components per cell
E
Total length of mito components per cell (µm)
F
Networked
Non-Networked
Total number of mito components per cell
G
Total length of mito components per cell (um)
H
% of mito components
(log) Length of an individual mito component

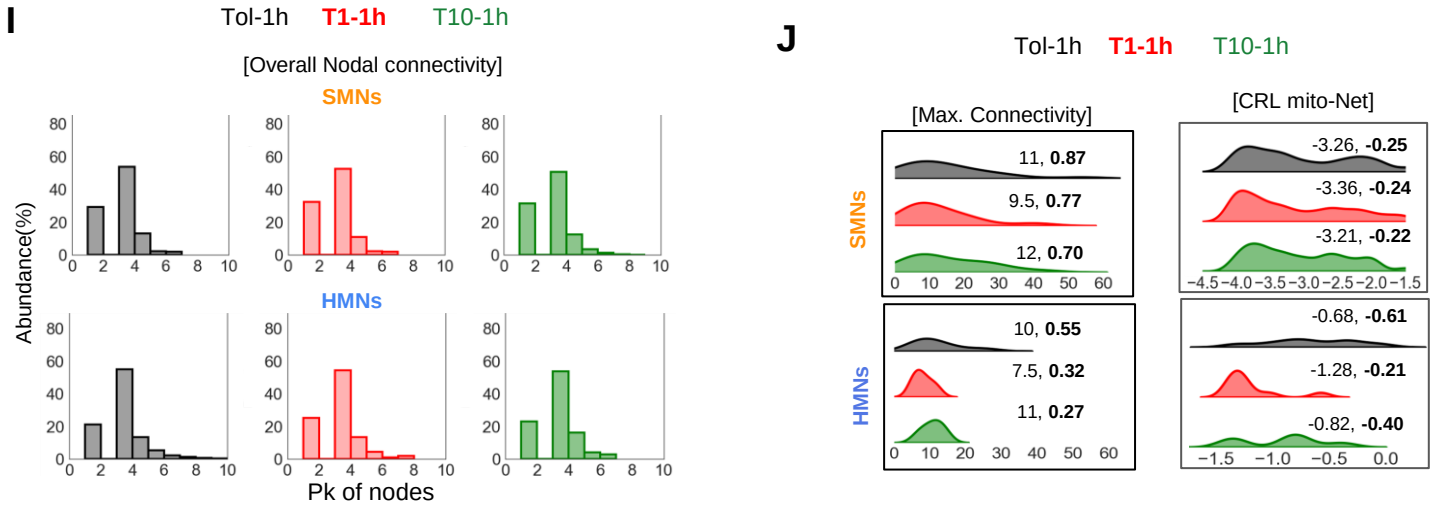
I
Tol-1h
T1-1h
T10-1h
[Overall Nodal connectivity]
SMNs
HMNs
Abundance(%)
Pk of nodes
J
[Max. Connectivity]
[CRL mito-Net]
SMNs
HMNs
11, 0.87
9.5, 0.77
12, 0.70
10, 0.55
7.5, 0.32
11, 0.27
-3.26, -0.25
-3.36, -0.24
-3.21, -0.22
-0.68, -0.61
-1.28, -0.21
-0.82, -0.40

Fig. S3

Figure. S3. Studying the impact of T1-1h and T10-1h exposure on mitochondrial potential and mitochondrial structural properties employing mito-SinComp structural analyses. A. Maximum Intensity Projections of Z-slices of TMRE-stained HaCaT cells after Tol-1h, T1-1h, T10-1h treatment. Scale bar: 20 µm. **B.** Bar chart showing the mean fluorescent intensity of MTG and TMRE from individual HaCaT cells from confocal micrographs of Tol-1h, T1-1h, T10-1h (top) and Tol-4h, T1-4h and T10-4h (bottom) groups. **C.** Representative maximum intensity projection (MIP) of original Z slices and Binary from mitoGraph code used in mtio-SinComp analysis described in **Fig. 2**; Scale bar: 5 µm. **D.** Box plot of the total number of mitochondrial components (including networks and non-networks) per cell in Tol-1h, T1-1h and T10-1h groups. **E.** Box plot of the total length of mitochondrial components (including networks and non-networks) per cell in Tol-1h, T1-1h and T10-1h groups **F.** Box plot of the total number of mitochondrial components per cell in networked and non-networked categories in Tol-1h, T1-1h and T10-1h groups. **G.** Box plot of the total length of mitochondrial components per cell in networked and non-networked categories in Tol-1h, T1-1h and T10-1h groups. **H.** Histogram distribution of log-transformed raw lengths of individual mitochondrial components in networked and non-networked category in Tol-1h, T1-1h and T10-1h groups. **I.** Histogram showing overall nodal connectivity of SMNs and HMNs in Tol-1h, T1-1h and T10-1h groups. **J.** Ridgeline plot comparing the distribution of structural parameters between SMNs and HMNs from Tol-1h, T1-1hand T10-1h groups; Median and Coefficient of Variation are indicated for each parameter, latter in bold. (* signifies Holmes-Bonferroni corrected p-value < 0.05)

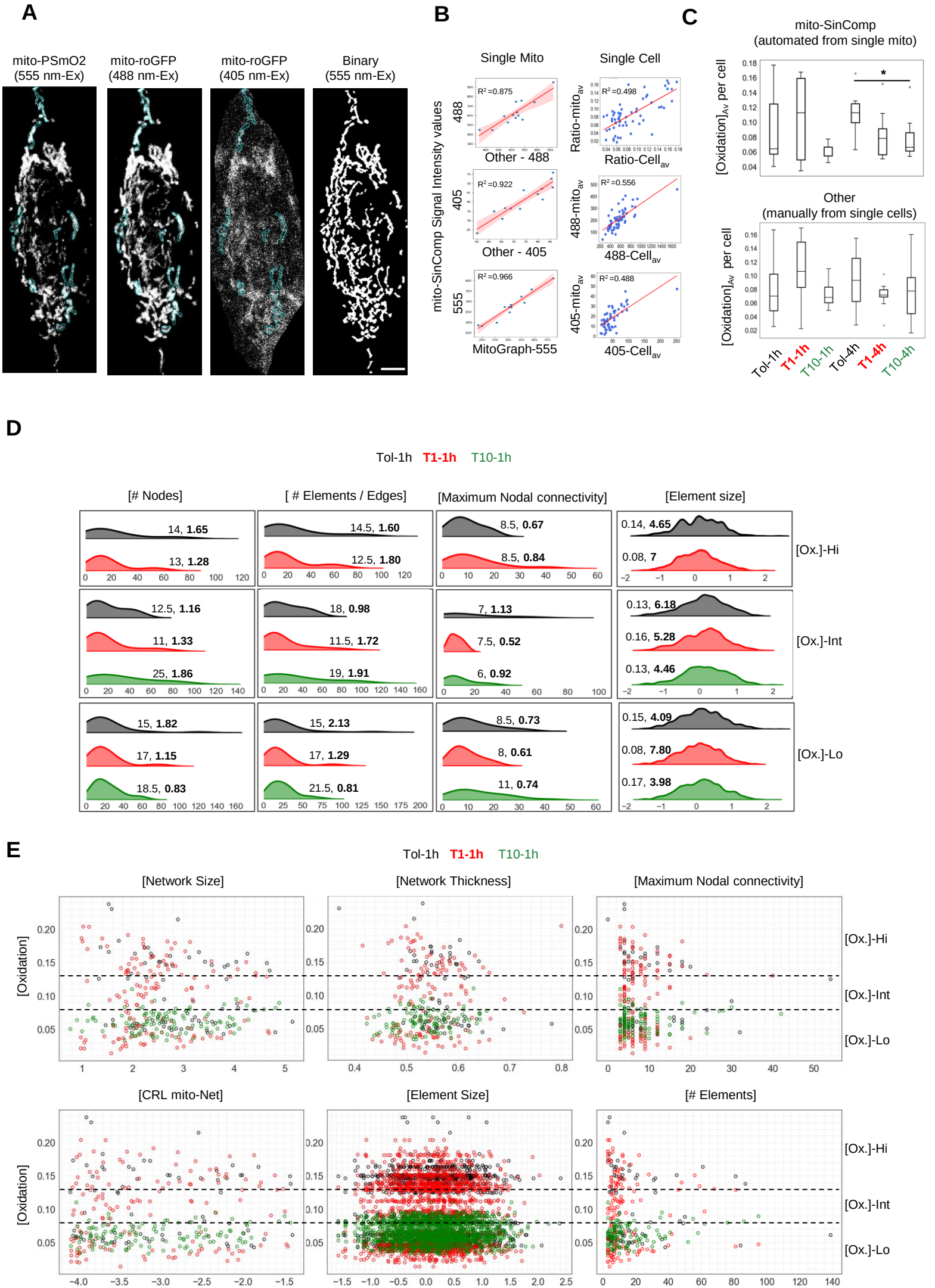
A
mito-PSmO2 (555 nm-Ex)
mito-roGFP (488 nm-Ex)
mito-roGFP (405 nm-Ex)
Binary (555 nm-Ex)
B
Single Mito
Single Cell
mito-SinComp Signal Intensity values
488
Other - 488
405
Other - 405
555
MitoGraph-555
Ratio-mito$_{av}$
Ratio-Cell$_{av}$
488-mito$_{av}$
488-Cell$_{av}$
405-mito$_{av}$
405-Cell$_{av}$
C
mito-SinComp (automated from single mito)
Other (manually from single cells)
[Oxidation]$_{Av}$ per cell
Tol-1h
T1-1h
T10-1h
Tol-4h
T1-4h
T10-4h
D
Tol-1h T1-1h T10-1h
[# Nodes]
[# Elements / Edges]
[Maximum Nodal connectivity]
[Element size]
[Ox.]-Hi
[Ox.]-Int
[Ox.]-Lo
E
Tol-1h T1-1h T10-1h
[Network Size]
[Network Thickness]
[Maximum Nodal connectivity]
[CRL mito-Net]
[Element Size]
[# Elements]
[Oxidation]

Fig. S4

Figure. S4. Studying the impact of T1-1h and T10-1h exposure on mitochondria employing mito-SinComp structure-function analyses. A. Representative Maximum Intensity Projection (MIP) of single cell from the mtio-SinComp structure-function analysis described in **Fig. 3**; shown are the channels corresponding to the mitochondrial structure (mito-PsMO2) or function (mito-roGFP) probes and the MitoGraph binary image. Scale bar: 5 µm. **B.** Bivariate plot of signal intensity values obtained using mito-SinComp structure-function script and that from ImageJ. Values are for 13 individual mitochondrial component (network or non-network) outlined in the representative cell in **A** (Left); Similar comparison shown for averaged values at the single-cell level (Right). **C.** Box plot of the $[\text{Oxidation}]_{Av}$ per cell, as calculated using the automated mito-SinComp script (top) and manually from single cells using image analysis software (bottom). **D.** Ridgeline plot comparing the distribution of structural parameters of SMNs between three zones of oxidation from Tol-1h, T1-1h and T10-1h groups; Median and Coefficient of Variation are indicated for each parameter, the latter in bold. **E.** Scatter plot of [Oxidation] vs various structure parameters for individual SMNs in Tol-1h, T1-1h and T10-1h groups; the dashed line indicates bifurcation into three [Oxidation] zones as described in the appropriate Results section.

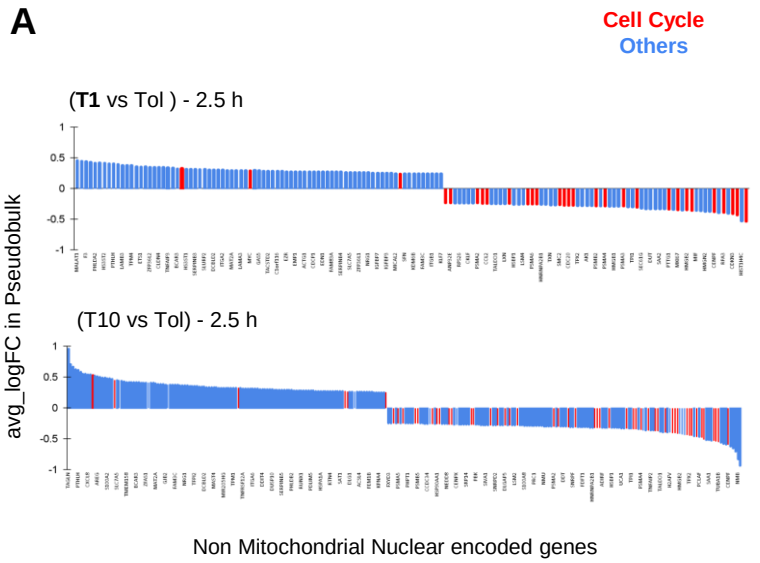

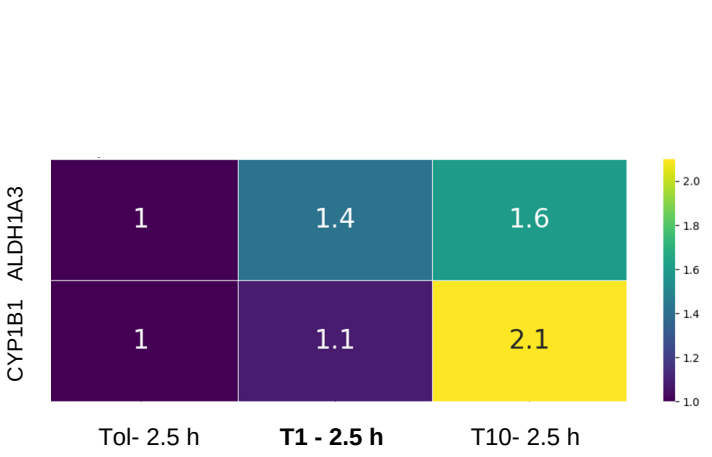

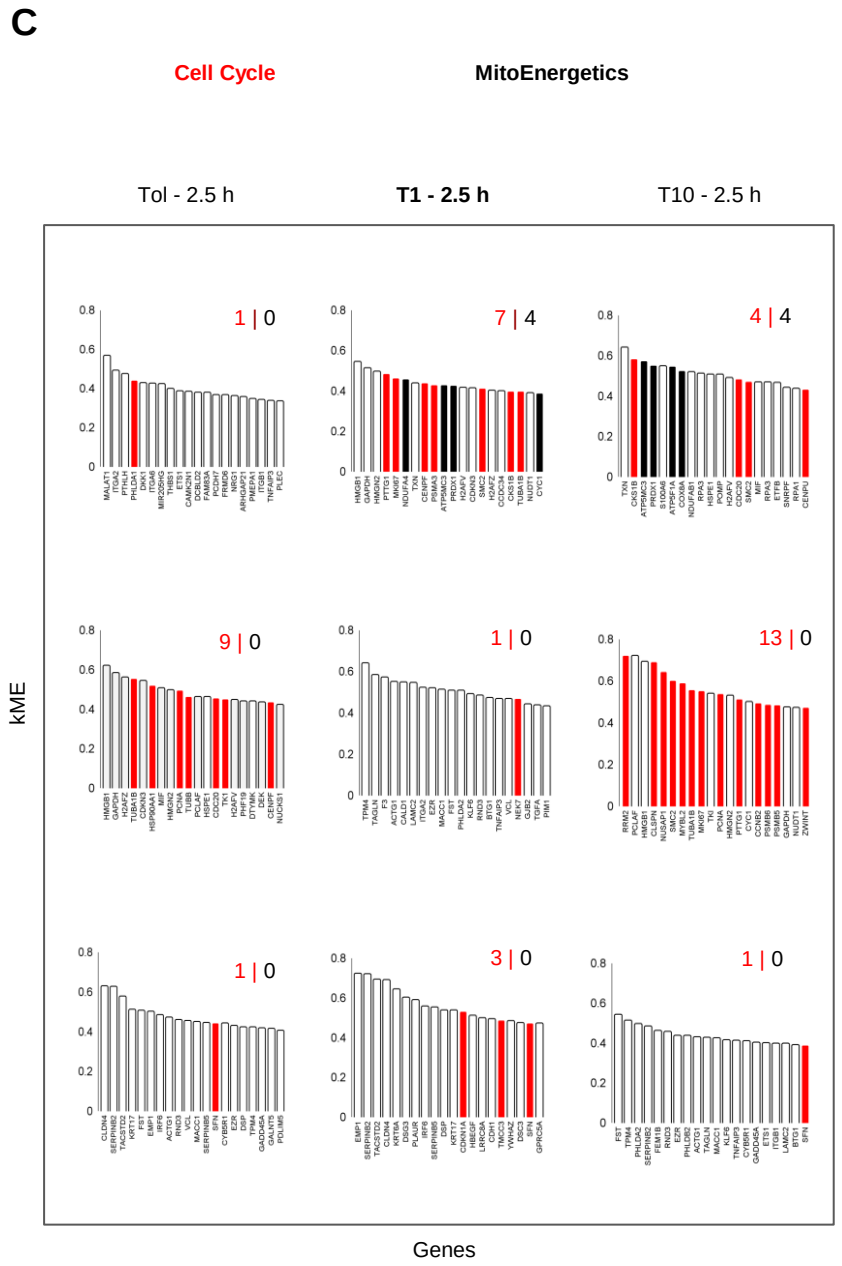

D

Genes	Direct Connections #
GAPDH	16
PSMA3	12
CDC20	7
MKI67	5
CYC1	5
CENPF	4
HMGB1	3
PTTG1	3
NDUFA4	3
CCDC34	3
ATP5MC3	3
H2AFV	3
COX8A	3
COX5B	3
CDKN3	2
HSPE1	2
HNRNPA2B1	2
PRDX1	1
CCNB2	1
H2AFZ	1

Fig. S5

Figure S5. Studying the impact of T1-2.5h and T10-2.5h exposure using hdWGCNA on pseudo-bulk pairwise analyses. A. Bar plots showing the modulation of expression of non-mitochondrial nuclear encoded genes Pairwise pseudo-bulk analyses T1-2.5h vs Tol-2.5h and T10-2.5h vs Tol-2.5h using Seurat's 'FindMarkers' (FM) function on scRNA-seq data; only are shown here. **B.** Heat map showing average gene expression of CYP1B1 and ALDHA3 induced by TCDD. Color intensity represents average expression values, with a scale from 1 (low) to 2 (high). Warmer colors indicate higher expression levels. **C.** Corresponding kME plots of modules using hdWGCNA modules, for pairwise pseudobulk analyses of T10-2.5h with respect to Tol-2.5h. Mitochondrial energetics genes are labelled in black, and cell cycle genes are labelled in red **D.** Tabulation of Degree Connectivity (in terms of direct connections) for the top20 genes identified in the hdWGCNA-derived modules as in **C**. GAPDH shows the maximum connectivity with cell cycle and mitochondrial genes on either side of the network as shown in **Fig. 4F**.

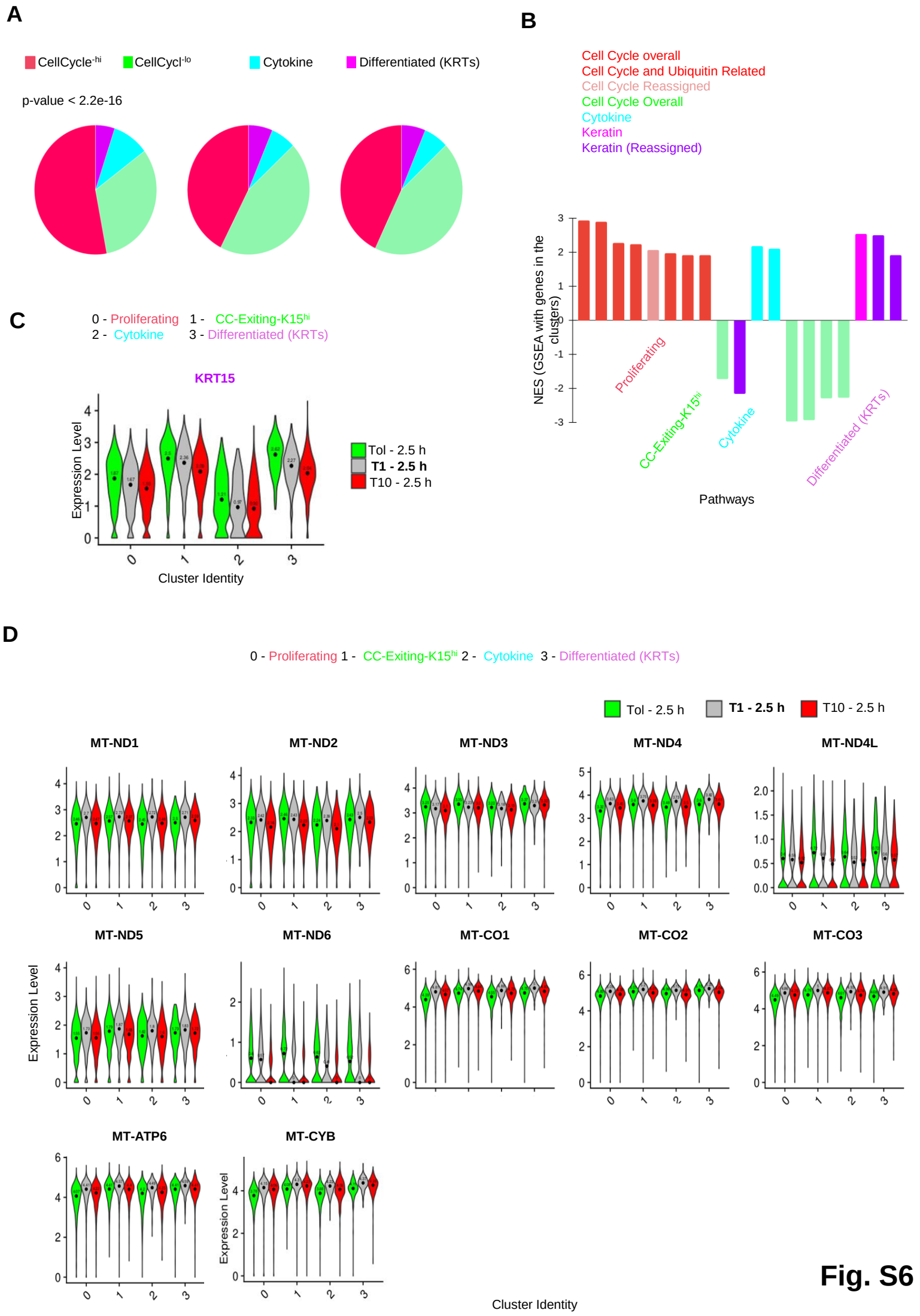
A
CellCycle-hi
CellCycl-lo
Cytokine
Differentiated (KRTs)
p-value < 2.2e-16
B
Cell Cycle overall
Cell Cycle and Ubiquitin Related
Cell Cycle Reassigned
Cell Cycle Overall
Cytokine
Keratin
Keratin (Reassigned)
NES (GSEA with genes in the clusters)
Proliferating
CC-Exiting-K15hi
Cytokine
Differentiated (KRTs)
Pathways
C
0 - Proliferating
1 - CC-Exiting-K15hi
2 - Cytokine
3 - Differentiated (KRTs)
KRT15
Expression Level
Cluster Identity
Tol - 2.5 h
T1 - 2.5 h
T10 - 2.5 h
D
0 - Proliferating 1 - CC-Exiting-K15hi 2 - Cytokine 3 - Differentiated (KRTs)
Tol - 2.5 h
T1 - 2.5 h
T10 - 2.5 h
MT-ND1
MT-ND2
MT-ND3
MT-ND4
MT-ND4L
MT-ND5
MT-ND6
MT-CO1
MT-CO2
MT-CO3
MT-ATP6
MT-CYB
Expression Level
Cluster Identity

Fig. S6

Figure S6. Studying the impact of T1-2.5h and T10-2.5h exposure on scRNA-seq derived clusters. A. Piechart displaying the percentage distribution of scRNA-seq derived cell clusters in Tol-2.5h, T1-2.5h and T10-2.5h cell populations. Chi-square test p-values are indicated. B. Normalized enrichment scores (NES) of functional pathways identified by GSEA for marker genes of Clusters 0-3. Functional annotations based on leading-edge genes are listed on top, with color-coded clusters arranged as in **Fig. 5A. C.** Violin plots showing expression levels of the stem cell gene KRT15 in Tol-2.5h, T1-2.5h and T10-2.5h cell populations across scRNA-seq derived cell clusters (0-3). **D.** Violin plots showing the expression of mtDNA genes in Tol-2.5h, T1-2.5h and T10-2.5h cell populations across scRNA-seq derived cell clusters (0-3).

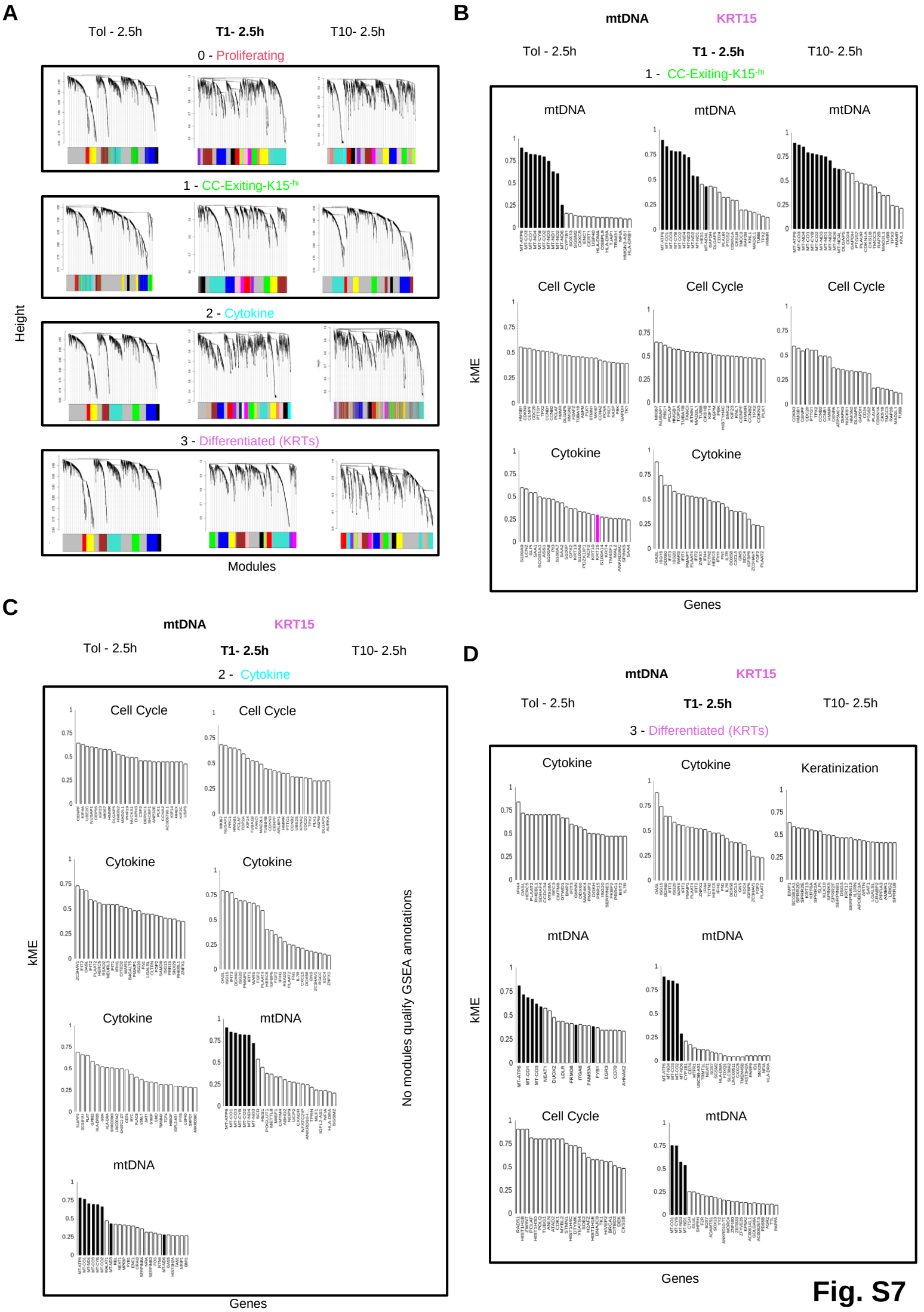
A
Tol - 2.5h
T1- 2.5h
T10- 2.5h
0 - Proliferating
1 - CC-Exiting-K15-hi
2 - Cytokine
3 - Differentiated (KRTs)
Height
Modules
B
mtDNA
KRT15
Tol - 2.5h
T1 - 2.5h
T10- 2.5h
1 - CC-Exiting-K15-hi
mtDNA
Cell Cycle
Cytokine
kME
Genes
C
mtDNA
KRT15
Tol - 2.5h
T1- 2.5h
T10- 2.5h
2 - Cytokine
Cell Cycle
Cytokine
mtDNA
kME
Genes
No modules qualify GSEA annotations
D
mtDNA
KRT15
Tol - 2.5h
T1- 2.5h
T10- 2.5h
3 - Differentiated (KRTs)
Cytokine
Keratinization
mtDNA
Cell Cycle
kME
Genes

Fig. S7

Figure S7. Studying the impact of T1-2.5h and T10-2.5h exposure on gene co-expression modules using hdWGCNA on single cell clusters. A. Dendrograms generated through hierarchical clustering of adjacency-based dissimilarity to identify distinct co-expression color coded modules (grey denotes no significant coexpression) for Tol-2.5h, T1-2.5h and T10-2.5h hdWGCNA objects across scRNA-seq derived cell clusters. **B.** kME Plots from hdWGCNA, for non mtDNA-KRT15 interacting modules of scRNASeq derived CC-Exiting-K15^{hi} cell cluster for Tol-2.5h, T1-2.5h and T10-2.5h cell population. **C.** Plot similar to **Fig. S7B** for Cytokine cluster. **D.** Plot similar to **Fig. S7B** for Differentiated (KRTs) cluster.

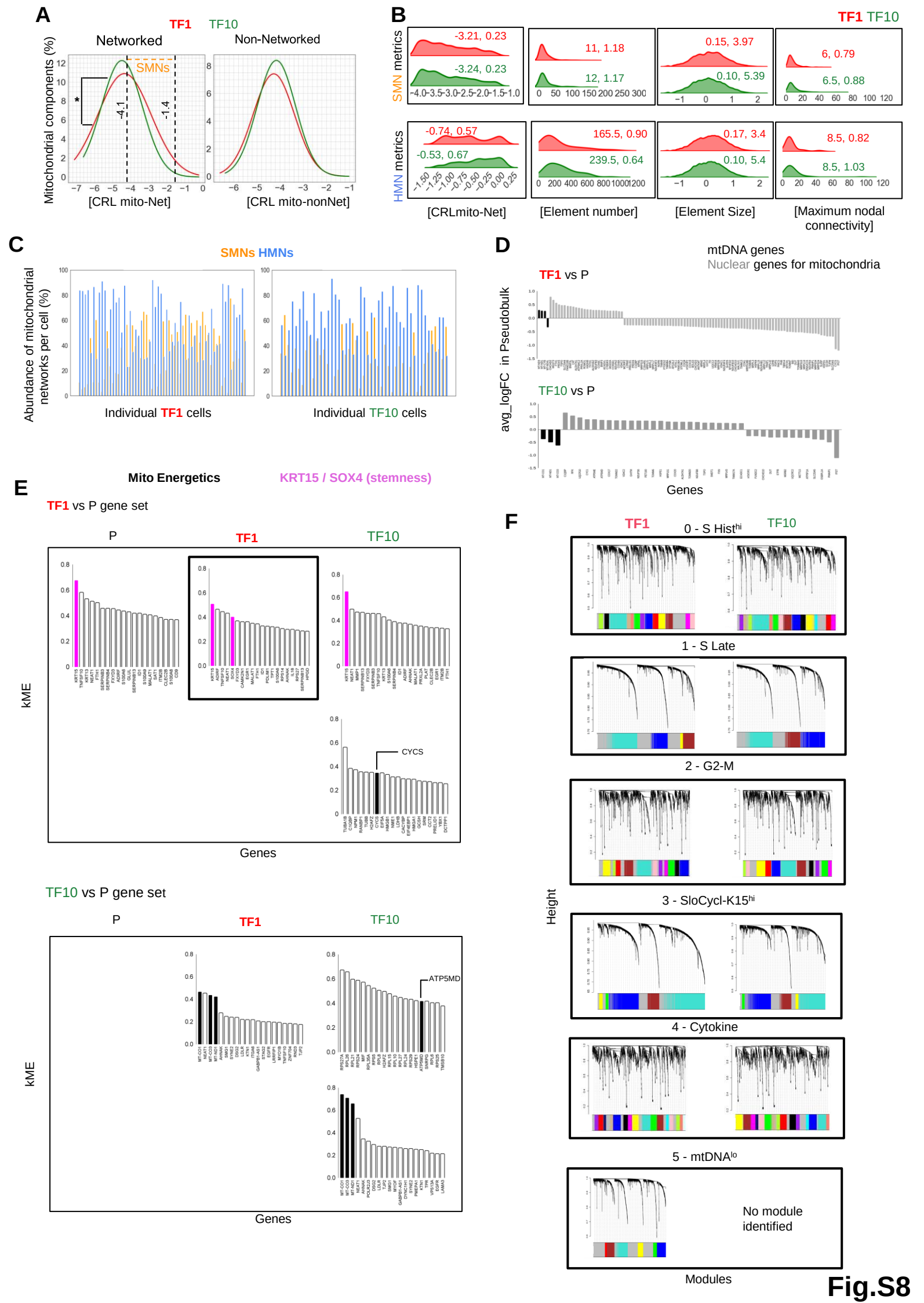
A
TF1
TF10
Networked
Non-Networked
SMNs
Mitochondrial components (%)
-4.1
-1.4
[CRL mito-Net]
[CRL mito-nonNet]
B
TF1 TF10
SMN metrics
HMN metrics
-3.21, 0.23
-3.24, 0.23
11, 1.18
12, 1.17
0.15, 3.97
0.10, 5.39
6, 0.79
6.5, 0.88
-0.74, 0.57
-0.53, 0.67
165.5, 0.90
239.5, 0.64
0.17, 3.4
0.10, 5.4
8.5, 0.82
8.5, 1.03
[CRLmito-Net]
[Element number]
[Element Size]
[Maximum nodal connectivity]
C
SMNs HMNs
Abundance of mitochondrial networks per cell (%)
Individual TF1 cells
Individual TF10 cells
D
mtDNA genes
Nuclear genes for mitochondria
TF1 vs P
TF10 vs P
avg_logFC in Pseudobulk
Genes
E
Mito Energetics
KRT15 / SOX4 (stemness)
TF1 vs P gene set
P
TF1
TF10
kME
CYCS
Genes
TF10 vs P gene set
ATP5MD
F
TF1
TF10
0 - S Hist^hi
1 - S Late
2 - G2-M
3 - SloCycl-K15^hi
4 - Cytokine
5 - mtDNA^lo
Height
No module identified
Modules

Fig.S8

Figure S8. Studying the impact of TF1 and TF10 transformation on mitochondrial structural properties employing mito-SinComp structural analyses and overall gene co-expression profile using hdWGCNA A. Histogram distribution of Cell-Relative Length of a mitochondrial component [CRL mito-Net] or [CRL mito-nonNet] corresponding to networked or non-networked mitochondrial components in TF1 and TF10 transformed cell population; threshold value for identifying SMNs and HMNs (same as **Fig 1**) are marked with dashed lines. **B.** Ridgeline plot comparing the distribution of structural parameters between SMNs and HMNs from TF1 and TF10 groups; Median and Coefficient of Variation are indicated for each parameter, the latter in bold. **C.** Bar plot showing the abundance of mitochondrial networks per cell in SMNs and HMNs categories in TF1 and TF10 groups. **D.** TF1 vs P and TF10 vs P pairwise pseudo-bulk analyses on scRNA-seq data; only mitochondrial nuclear encoded genes are shown here. **E.** kME Plots for hdWGCNA, for non mtDNA-KRT15 interacting modules using genelist from TF1 vs P (top) and TF10 vs.P (bottom) pairwise pseudo bulk analyses. The mtDNA encoded genes are labeled in black, and stem cell genes KRT15 and SOX4 are labeled in purple. **F.** Dendrograms as in **Fig.S7** for TF1 and TF10 hdWGCNA objects across scRNA-seq derived cell clusters.

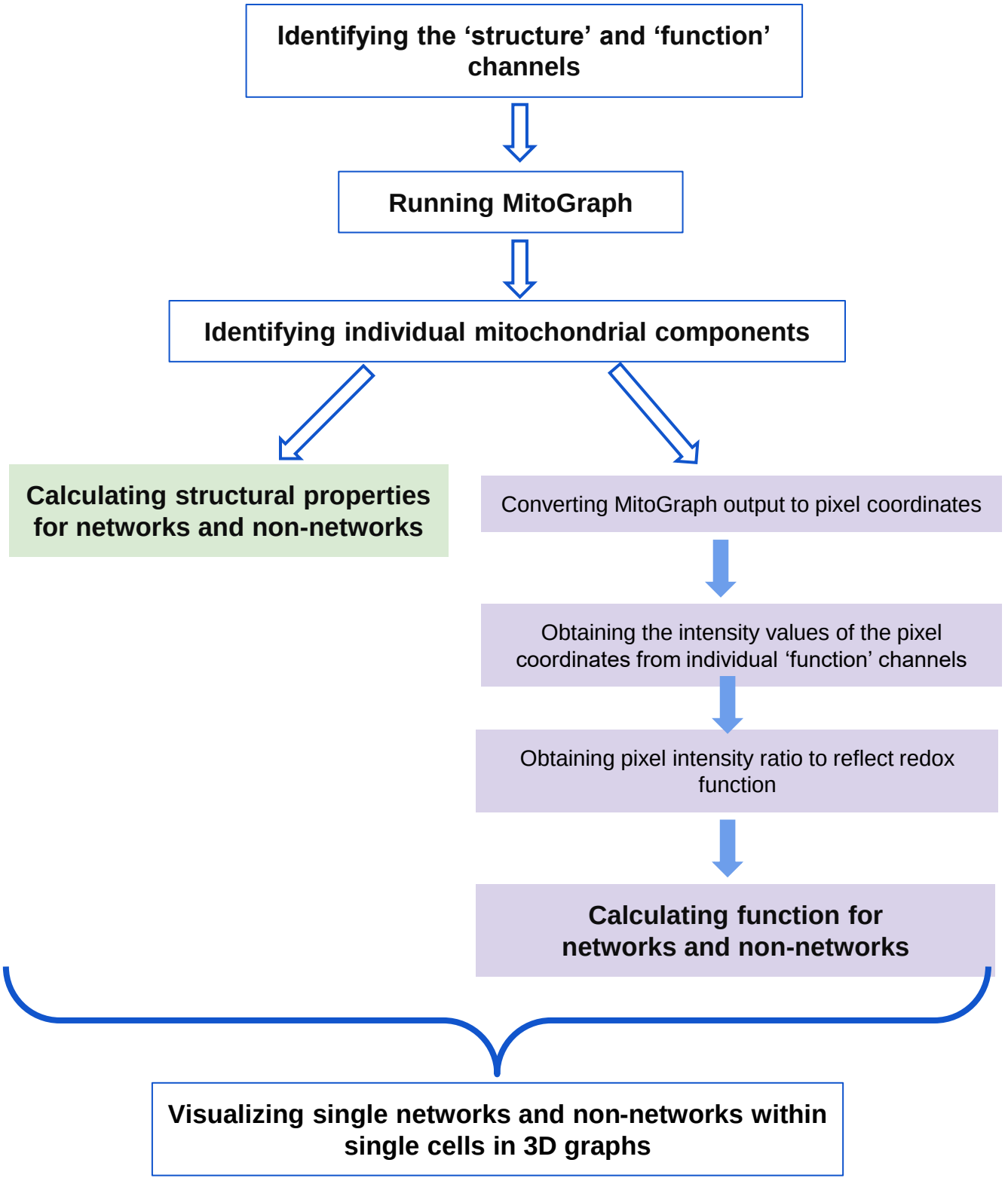
Identifying the 'structure' and 'function' channels
Running MitoGraph
Identifying individual mitochondrial components
Calculating structural properties for networks and non-networks
Converting MitoGraph output to pixel coordinates
Obtaining the intensity values of the pixel coordinates from individual 'function' channels
Obtaining pixel intensity ratio to reflect redox function
Calculating function for networks and non-networks
Visualizing single networks and non-networks within single cells in 3D graphs

Fig. S9

Figure S9. Workflow showing stepwise process for mito-SinComp analyses. The workflow includes identifying 'structure' and 'function' channels, running MitoGraph to delineate individual mitochondrial components, calculating structural and functional properties for networks and non-networks, and visualizing individual mitochondrial networks and non-networks in the form of 3D graphs.

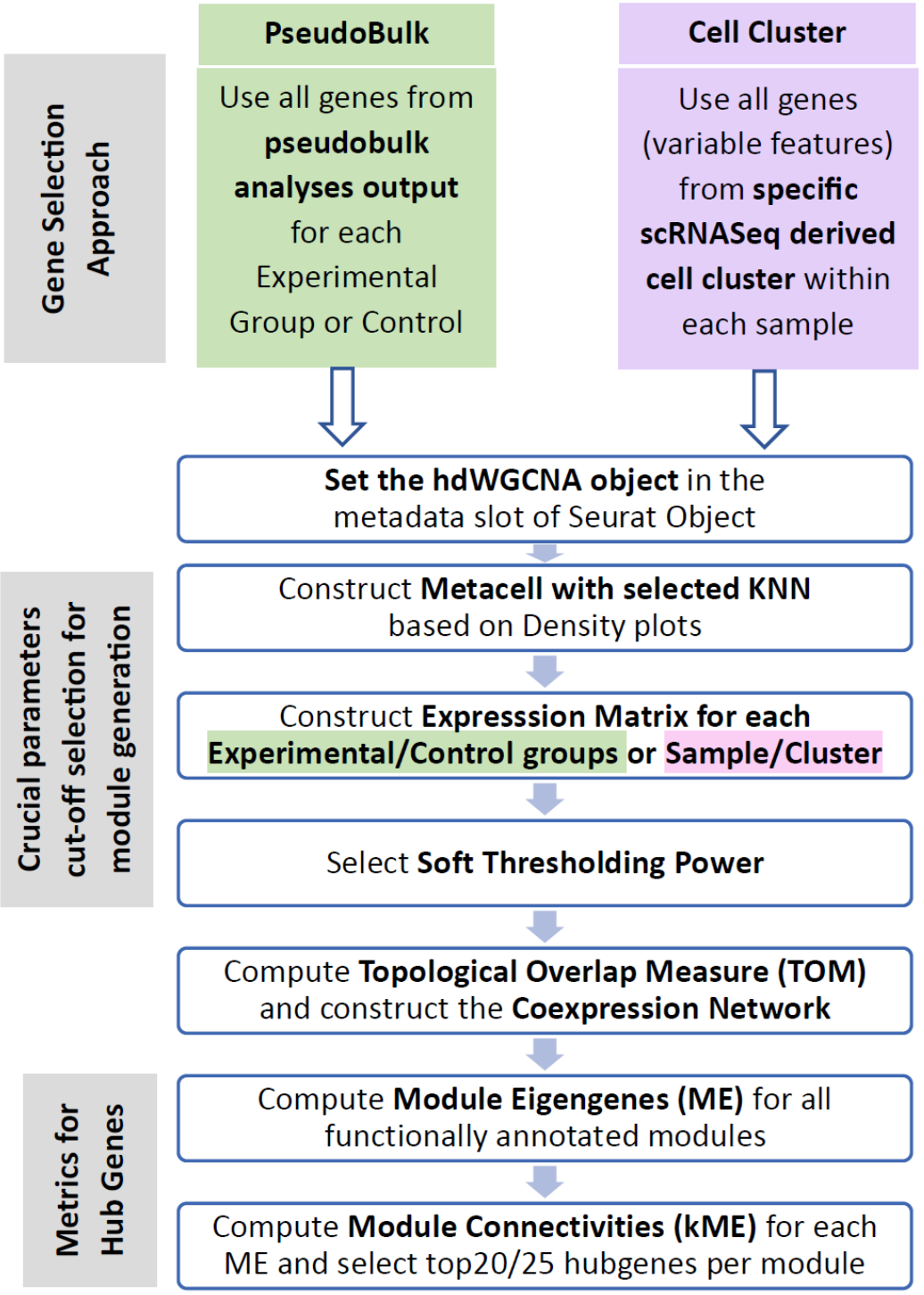
Gene Selection Approach
PseudoBulk
Use all genes from pseudobulk analyses output for each Experimental Group or Control
Cell Cluster
Use all genes (variable features) from specific scRNASeq derived cell cluster within each sample
Set the hdWGCNA object in the metadata slot of Seurat Object
Crucial parameters cut-off selection for module generation
Construct Metacell with selected KNN based on Density plots
Construct Expresssion Matrix for each Experimental/Control groups or Sample/Cluster
Select Soft Thresholding Power
Compute Topological Overlap Measure (TOM) and construct the Coexpression Network
Metrics for Hub Genes
Compute Module Eigengenes (ME) for all functionally annotated modules
Compute Module Connectivities (kME) for each ME and select top20/25 hubgenes per module

Fig. S10

Figure S10. Workflow for detailed stepwise process for hdWGCNA. The hdWGCNA workflow allows network-based transcriptomic analysis in both pseudobulk and single-cell cluster contexts. The stepwise process begins with setting up hdWCGNA object, then constructing metacells using K-nearest neighbors (KNN), followed by computing Pearson's correlations, and transforming them into adjacency matrices with soft-thresholding. Thereafter, networks are built using Topological Overlap Measures (TOM), and transcriptomic modules are identified via hierarchical clustering. Finally, module eigengenes (MEs) and connectivity (kME) values are calculated to identify hub genes.

A

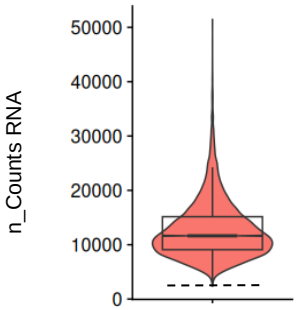

B

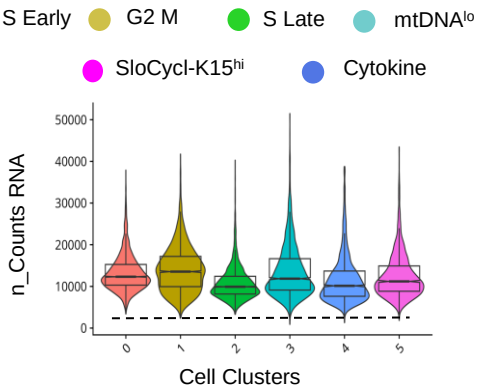

C

DRP1-kd Dataset	nCounts	KNN	Max shared
Pseudobulk	>=2000	20	10
Cell Cluster Based			

D

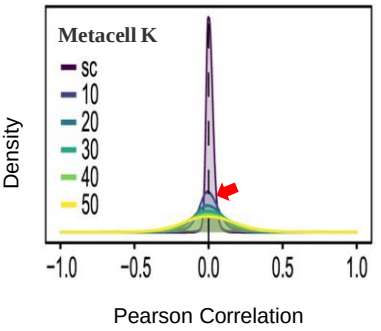

E

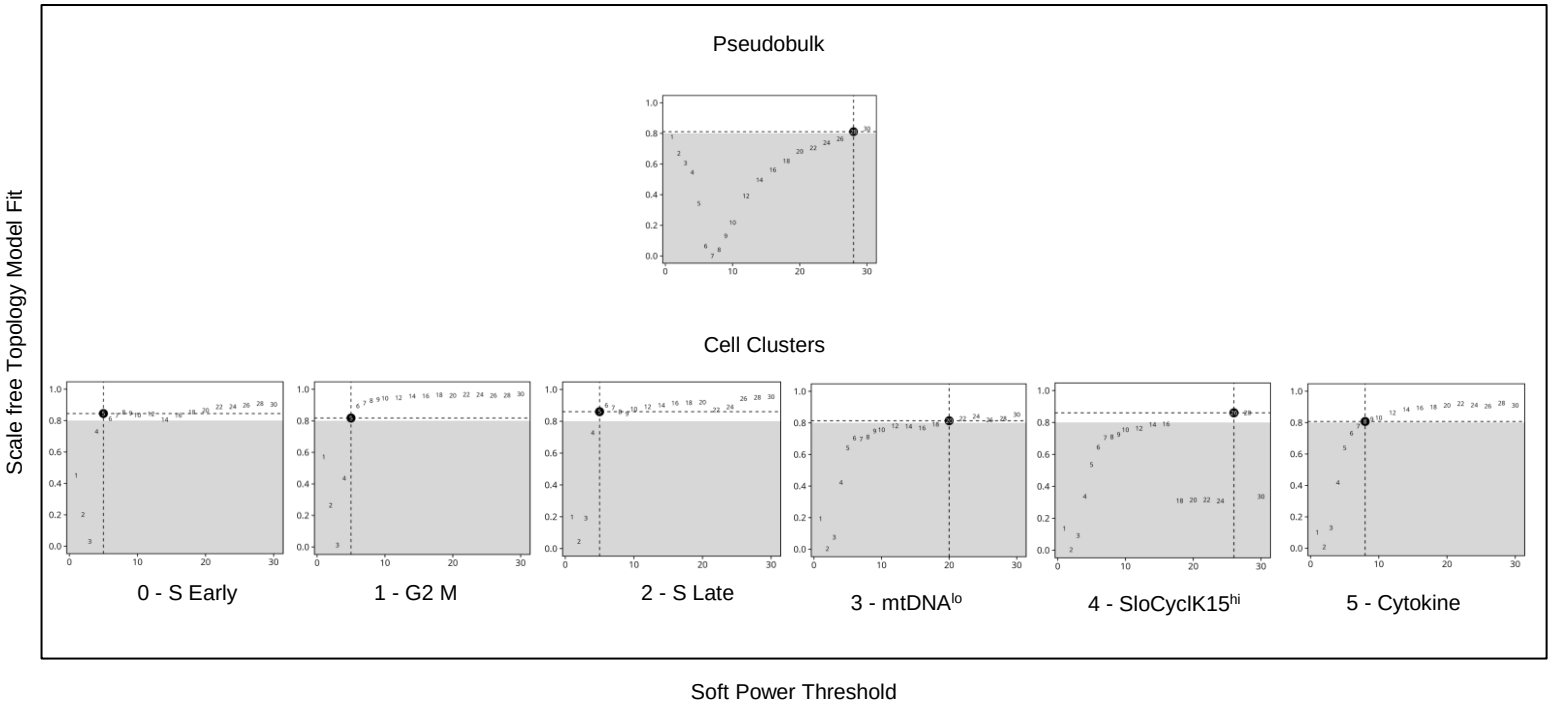

Fig. S11

Figure S11. Optimized parameters for hdWGCNA related to Fig. 1 A. Violin plots display the distribution of high-quality cell counts(n_Counts) for pooled data of DRP1-kd (W) & (S) with NT for pseudobulk analyses; dashed lines represent the selected threshold. **B.** Violin plots obtained as in **Fig.S11A** for clusterwise scRNASeq derived cluster. **C.** Table with parameters for n_Counts, KNN and maximum shared (max_shared) considered for the designated cell populations **D.** Density plot illustrating the distribution of pairwise Pearson correlations between genes from the single-cell expression matrix and metacell expression matrices with varying values of KNN parameter K; red arrow indicates the selected KNN value**. E.** Optimal soft-thresholding power (β) in hdWGCNA for DRP1 pooled data. The panel shows the influence of soft-threshold power on the scale-free fit index for the designated hdWGCNA object.

A

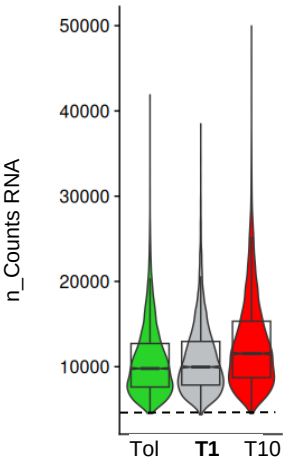

B

Dataset	nCount_RNA	KNN	Maxshared
Acute -2.5h: Pseudobulk	>=2000	20	10

C

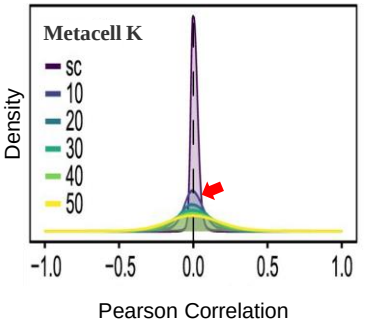

D

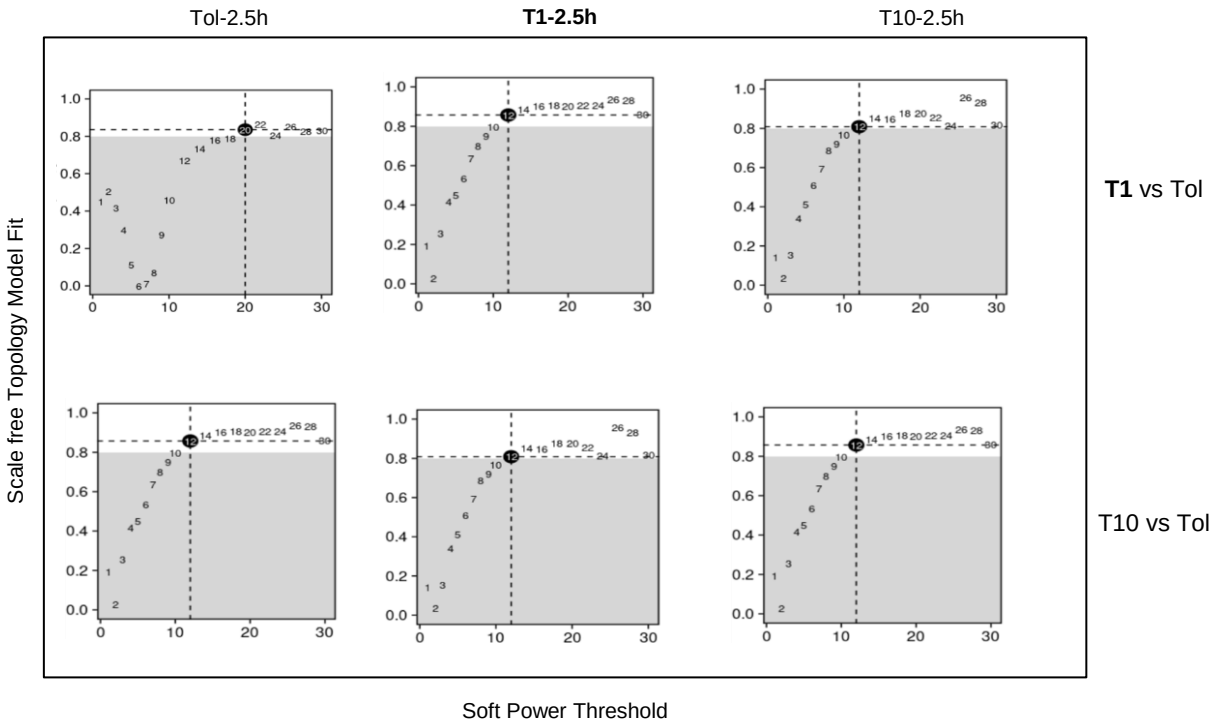

Fig. S12

Figure S12. A. Optimized parameters for hdWGCNA related to Fig. 4. Violin plots obtained as in **Fig.S11A** of T1-2.5hvs. Tol -2.5h and T10-2.5h vs. Tol -2.5h pseudobulk analyses based hdWGCNA objects. **B.** Table similar to **Fig.S11C** using pseudobulk analyses -hdWGCNA objects of Tol-2.5h, T1-2.5hand T10-2.5h **C.** Density plot similar to **Fig. S11D** for T1-2.5h vs. Tol -2.5h and T10-2.5h vs. Tol -2.5h pseudobulk analyses. **D.** Optimal soft-thresholding power (β) for T1-2.5h vs. Tol-2.5h and T10-2.5h vs. Tol-2.5h pseudobulk-hdWGCNA objects.

A

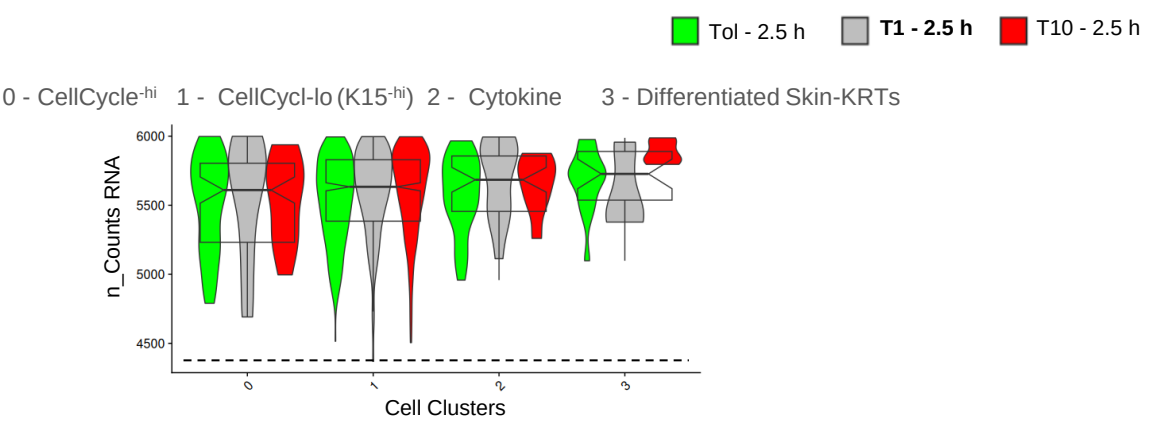

B

Dataset	nCounts	KNN	Max shared
Acute -2.5h: Cell Clusters	>=2000	20	10

C

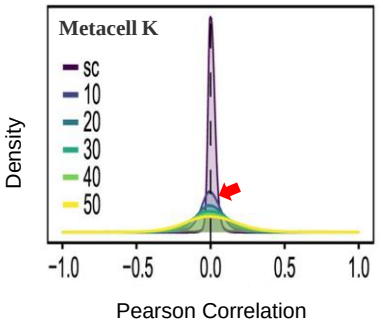

D

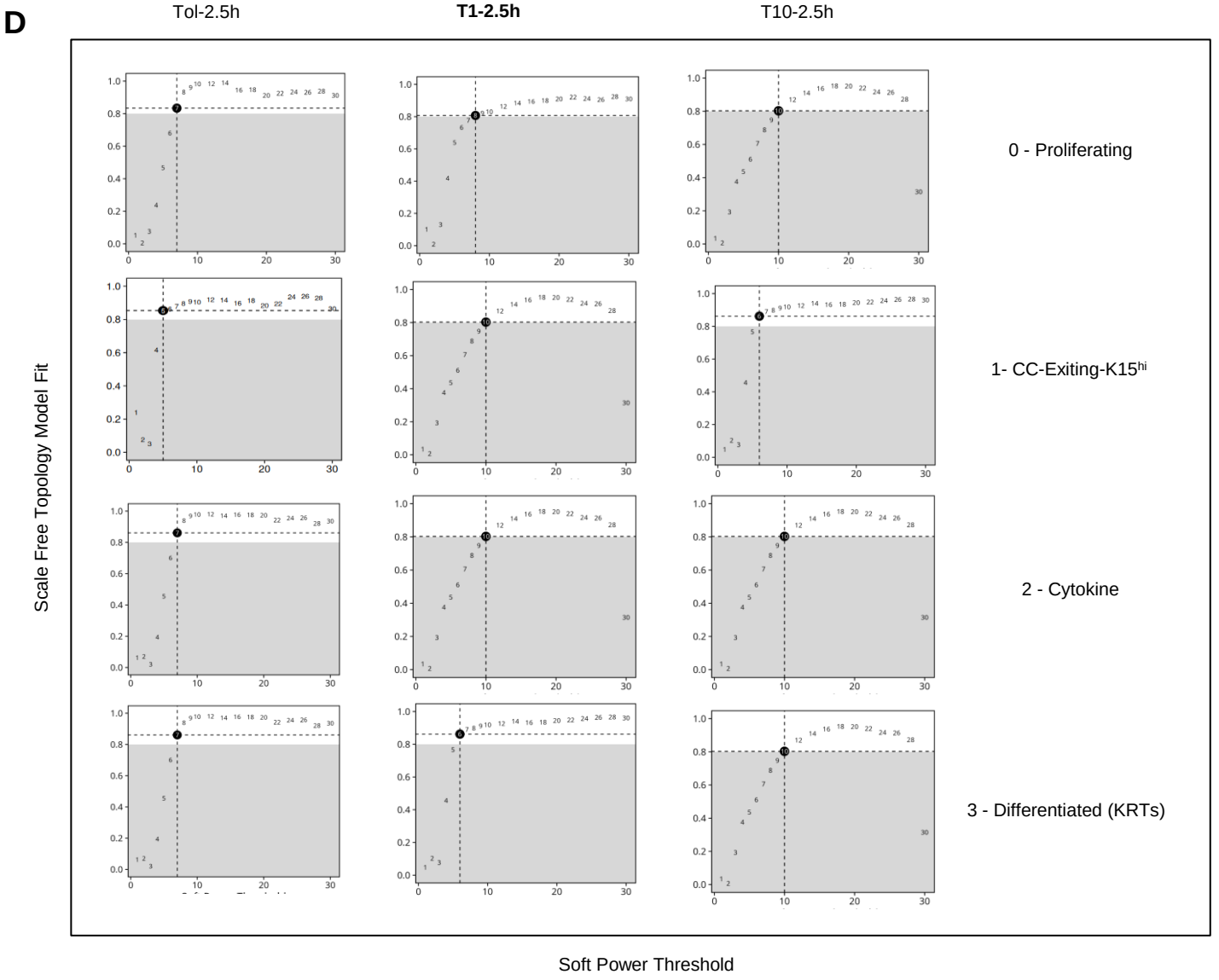

Fig. S13

Figure S13. Optimized parameters for hdWGCNA related to Fig. 5. A. Violin plots obtained as in **Fig.S11A** for Tol-2.5h, T1-2.5h and T10-2.5h across scRNA-seq derived clusters. **B.** Table similar to **Fig.S11C** using Tol-2.5h, T1-2.5hand T10-2.5h data **C.** Density plot similar to **Fig. S11D D.** Optimal soft-thresholding power (β) for Tol-2.5h, T1-2.5h and T10-2.5h cell clusters-hdWGCNA objects.

A

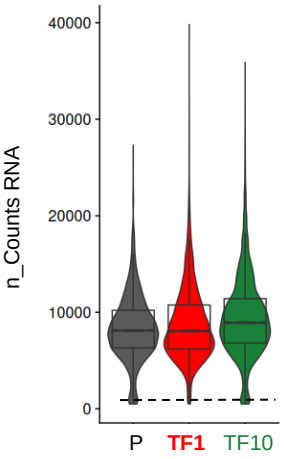

B

Dataset	nCount_RNA	KNN	Maxshared
Transformed: Pseudobulk	>=2000	20	10

C

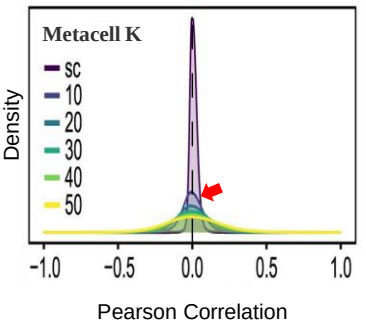

D

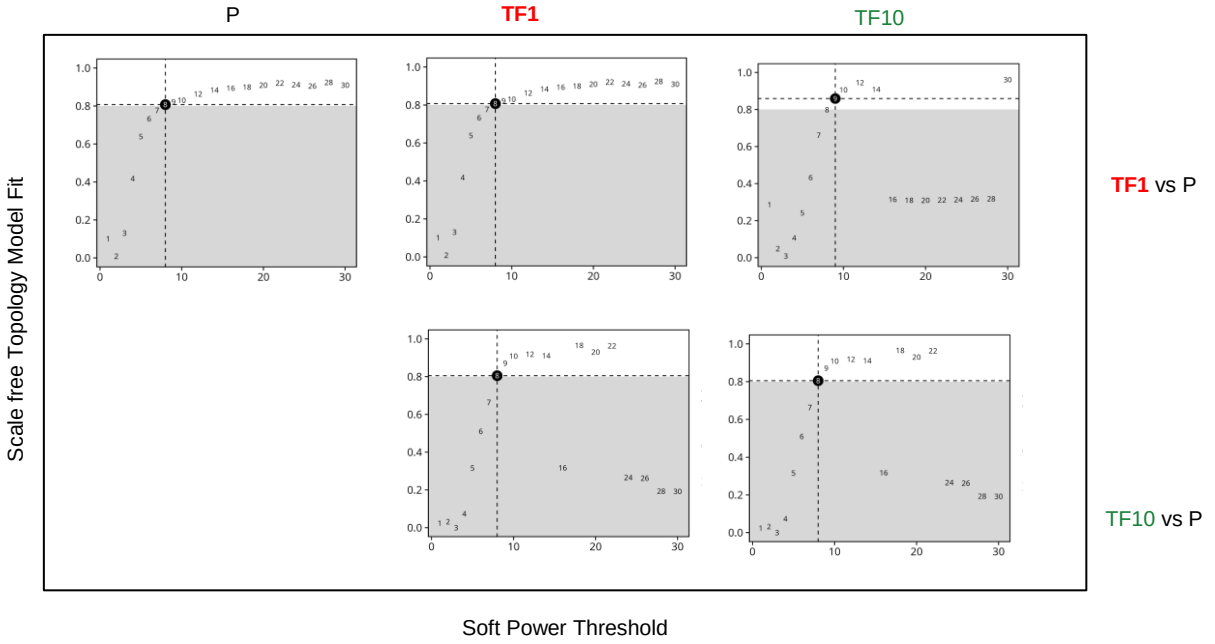

Fig. S14

Figure S14. Optimized parameters for hdWGCNA related to Fig. S8. A. Violin plots obtained as in **Fig.S11A** of TF1 and TF10 for pseudobulk analyses. **B.** Table similar to **Fig.S11C** for the transformed cell populations **C.** Density plot similar to **Fig. S11D** for the transformed cell populations. **D.** Optimal soft-thresholding power (β) for TF1 and TF10 pseudobulk-hdWGCNA objects.

A

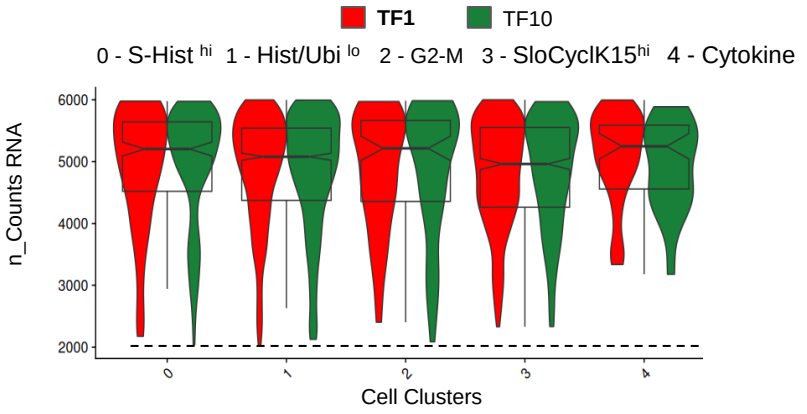

B

Dataset	nCounts	KNN	Max shared
TF1 & TF10	>=2000	20	10

C

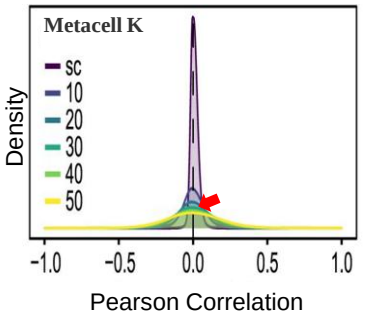

D

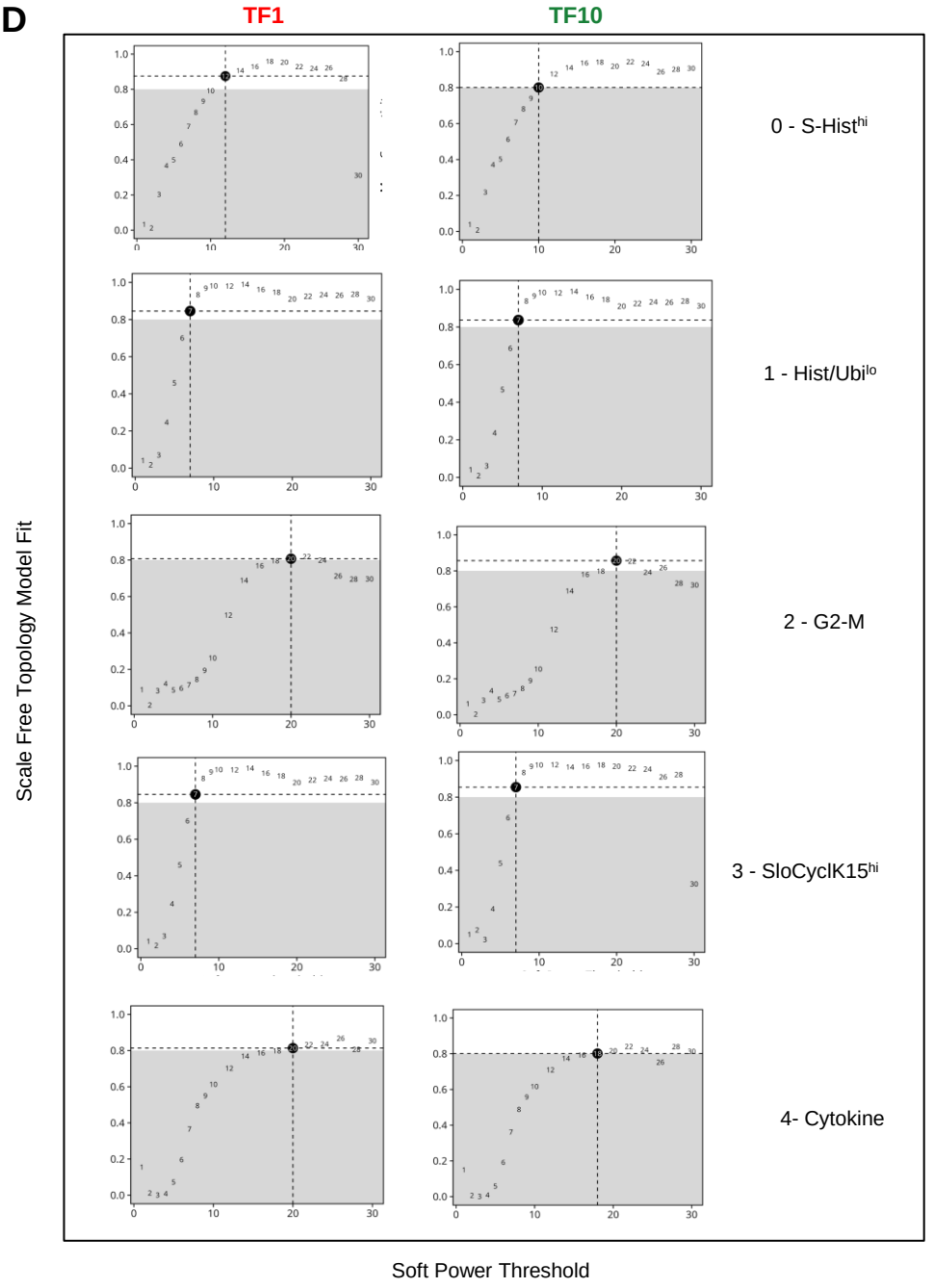

Fig. S15

Figure S15. Optimized parameters for hdWGCNA related to Fig. 6. A. Violin plots obtained as in **Fig.S11A** of TF1 and TF10 for scRNA-seq derived clusters. **B.** Table similar to **Fig.S11C** for the transformed cell populations **C.** Density plot similar to **Fig.S11D** for the transformed cell populations. **D.** Optimal soft-thresholding power (β) for TF1 and TF10 cell clusters-hdWGCNA objects.

References

1. B. Spurlock, K. Mitra, Mito-SinCe2 Approach to Analyze Mitochondrial Structure–Function Relationship in Single Cells. *Methods in Molecular Biology* **2275**, 415–432 (2021).

2. B. Spurlock, *et al.*, New quantitative approach reveals heterogeneity in mitochondrial structure–function relations in tumor-initiating cells. *J Cell Sci* **132** (2019).

3. M. P. Viana, S. Lim, S. M. Rafelski, Quantifying mitochondrial content in living cells. *Methods Cell Biol* **125**, 77–93 (2015).

4. S. Boccaletti, V. Latora, Y. Moreno, M. Chavez, D. U. Hwang, Complex networks: Structure and dynamics. *Phys Rep* **424**, 175–308 (2006).

5. M. P. Viana, *et al.*, Mitochondrial Fission and Fusion Dynamics Generate Efficient, Robust, and Evenly Distributed Network Topologies in Budding Yeast Cells. *Cell Syst* **10**, 287-297.e5 (2020).

6. S. Morabito, F. Reese, N. Rahimzadeh, E. Miyoshi, V. Swarup, hdWGCNA identifies co-expression networks in high-dimensional transcriptomics data. *Cell Reports Methods* **3** (2023).